Feb, 2022

PhD Dissertation

Synthesis, Properties, and Applications of 3D hBN/graphene Reinforced CuNi Composites

Graduate School of Chosun University

Department of Advanced Materials Engineering

Zahid Hussain

Synthesis, Properties, and Applications of 3D hBN/graphene Reinforced CuNi Composites

3차원 그래핀/육방정 질화붕소로 강화된 CuNi 복합체의 합성과 특성 그리고 응용

February 25, 2022

Graduate School of Chosun University

Department of Advanced Materials Engineering

Zahid Hussain

Synthesis, Properties, and Applications of 3D hBN/graphene Reinforced CuNi Composites

Advisor: Choi, Byung-Sang

A dissertation submitted in partial fulfillment of the requirements for a Doctoral Degree

Oct, 2021

Graduate School of Chosun University

Department of Advanced Materials Engineering

Zahid Hussain

후세인 자히드의 박사학위논문을 인준함

위원장	조선대학교 교수	강현철 (인)
위 원	조선대학교 교수	최병상 (인)
위 원	전남대학교 교수	박찬진 (인)
위 원	조선대학교 교수	장태식 (인)
위 원	조선대학교 교수	박현중 (인)

2022년 1월

조선대학교 대학원

Dedicated to my Wife for her patience

ACKNOWLEDGEMENTS

All praise is due to the Lord of the Worlds alone for granting me the strength and serenity to successfully complete my coursework and this dissertation.

I would like to express my utmost gratitude to my supervisor, Prof. Byung-Sang Choi, whose guidance and advice made it possible for me to complete this endeavor. Whenever I needed his support, he gladly provided me with all the facilities. I am indebted to the National Institute for International Education (NIIED) for granting me the scholarship to pursue this degree.

Last but not least, I would like to mention the unconditional support, love and care I received from my family. My mother, whose supplications are always with me, and my brothers, whose constant support has been a source of great hope and encouragement. And a special thank you to my wife and daughters for their patience and sacrifice during my studies. They have indeed contributed greatly to my ability to pursue my research goals.

TABLE OF CONTENTS

LIST OF ABBREVIATIONS AND ACRONYMS

BLG	Bilayer graphene
CVD	Chemical vapor deposition
DSC	Differential scanning calorimetry
EEC	Equivalent electrical circuit
hBN	Hexagonal boron nitride
EDS	Energy dispersive spectroscopy
EIS	Electrochemical impedance spectroscopy
ELD	Electrochemical deposition
FWHM	Full width at half maximum
MA	Mechanical alloying
MLM	Molecular level mixing
MMC	Metal matrix composite
MOCVD	Metal organic chemical vapor deposition
OM	Optical microscopy
ORR	Oxidation reduction reaction
PM	Powder metallurgy
SEM	Scanning electron microscopy
SLG	Single layer graphene
SPM	Semi powder metallurgy
SPS	Spark plasma sintering
SCCM	Standard cubic centimeter per minute
TC	Thermal conductivity
TEM	Transmission electron microscopy
UTS	Ultimate tensile strength
YS	Yield strength
XRD	Xray diffraction

LIST OF FIGURES

LIST OF TABLES

ABSTRACT

Synthesis, Properties, and Applications of 3D hBN/graphene Reinforced CuNi Composites

Zahid Hussain

Advisor: Prof. Choi, Byung-Sang

Department of Advanced Materials Engineering

Graduate School of Chosun University

Three dimensionally interconnected network of graphene or hBN can be a promising structure to improve the mechanical, thermal, and chemical properties of metal matrix composites. In this dissertation, a simple two-step process was used to fabricate $Cu_{0.7}Ni_{0.3}$ composites reinforced by such networks of graphene or hBN. A simple two-step process involves the compaction of micronsized Cu (70wt.%) and Ni (30wt.%) particles followed by chemical vapor deposition (CVD). hBN reinforced CuNi (3Di-hBN CuNi) composite was fabricated using the decaborane and ammonia precursors whereas graphene reinforced CuNi (3DiGr CuNi) composite was fabricated using the methane as precursor. By using various characterization techniques such as optical microscopy, scanning electron microscopy, transmission electron microscopy, and X-ray diffraction analysis, it was shown that graphene or hBN layers surround the CuNi grains and thus impart interesting attributes to the composite.

Uniaxial tensile investigations showed that 3Di-hBN positively influenced the mechanical properties of 3Di-hBN CuNi composite; $\sim$16.3%, $\sim$ 11.67%, and $\sim$ 27.9% higher yield strength, UTS, and fracture toughness, respectively, compared to PM CuNi alloy which was prepared under similar conditions except MOCVD. The overall improved mechanical performance of 3Di-hBN CuNi composite was attributed to the formation of 3Di-hBN layers at the interfaces of Cu-Ni grains, which enable the composite to withstand the applied load through the mechanisms of load transfer,

dislocation strengthening, and grain refinement. The electrochemical performance was examined by potentiodynamic polarization and electrical impedance spectroscopy while thermal performance was investigated by thermal gravimetric analysis and high-temperature oxidation experiment. The results indicated that 3Di-hBN CuNi composite displayed 6 times higher corrosion resistance than PM CuNi alloy (without hBN) during the electrochemical potentiodynamic corrosion experiments. Furthermore, high-temperature oxidation experiment performed at 900 °C revealed that 3DihBN CuNi composite gained ∼36% less weight compared to PM CuNi alloy indicating its better resistance to high-temperature oxidation. In addition, thermal conductivity of 3Di-hBN CuNi composite was found ∼10% higher than that of PM CuNi alloy. The improved chemical and thermal stabilities of 3Di-hBN CuNi and 3DiGr CuNi composites can be attributed to the impermeability and thermal stability of hBN/graphene, i.e. its ability to block the penetration/diffusion of atoms, ions or molecules at high temperatures. Similarly, 3DiGr CuNi also showed 58% higher thermal conductivity, ∼25.9% yeild strength than PM CuNi alloy. The improved properties were associated with the ability of 3D graphene network of providing conducting path channels for electron mobility and blocking the dislocation motion against the externally applied load.

한 글 요 약

3차원 그래핀/육방정 질화붕소로 강화된 CuNi 복합체의 합성과 특성 그리고 응용

후세인 자히드
지도 교수: 최병상
첨단소재공학과
대학원, 조선대학교

그래핀 또는 hBN의 3차원적으로 상호 연결된 네트워크는 금속 메트릭스 복합체의 기계적, 열적 및 화학적 특성을 향상시키는 유망한 구조가 될 수 있다. 본 논문에서는 그래핀과 hBN 네트워크로 강화된 $Cu_{0.7}Ni_{0.3}$ 복합 재료를 제작하기 위해 간단한 2단계 공정을 사용했다. 간단한 2단계 공정에는 마이크로 크기의 Cu 및 Ni 입자 혼합물을 압축 성형과 화학 기상 증착 (CVD)이 포함된다. hBN 강화 CuNi (3Di-hBN CuNi) 복합체는 데카보레인 (Decaborane) 및 암모니아 (NH_3) 전구체를 사용하여 제작된 반면 그래핀 강화 CuNi (3DiGr CuNi) 복합체는 메탄을 전구체로 사용하여 제작하였다. 광학 현미경, 주사 전자 현미경, 투과 전자 현미경 및 X-선 회절 분석과 같은 다양한 특성 평가 기술을 사용하여 그래핀 또는 hBN 층이 CuNi 입자를 둘러싸고 있어 복합체에 흥미로운 속성을 부여하는 것을 확인하였다. 단축 인장 시험은 3Di-hBN이 CVD 공정을 제외하였을 때 동일한 조건에서 제조된 PM CuNi 합금에 비해 3Di-hBN CuNi 복합체가 항복강도 및 최대 인장 강도, 파괴 인성이 각 ~16.3%, ~11.67% 및 ~27.9%이 향상되어 기계적 특성에 긍정적인 영향을 미치는 것으로 나타났다. 3Di-hBN CuNi 복합체의 전체적인 기계적 성능의 향상은 Cu-Ni 입자의 계면에서 3Di-hBN 층이 형성되어 복합체가 하중을 전달하고, 전위 강화, 입자 미세화 메커니즘을 통해 가해진 하중을 견딜 수 있게 된 것이다. 전기화학적 특성은 potentiodynamic polarization과 전기임피던스 분광 법으로 조사하였고, 열적 특성은 열 중량 분석과 고온 산화 실험으로 조사하였다. 그 결과 전기화학적 전위차 부식 실험 중 3Di-hBN CuNi 복합체가 PM CuNi 합금 (hBN 미포함)보다 6배 높은 내식성을 보였다. 또한, 900°C에서 수행된 고온 산화

실험에서 3Di-hBN CuNi 복합체가 PM CuNi 합금에 비해 중량이 ~36% 작게 증가하였으며, 이는 고온 산화에 대한 저항성이 더 우수함을 나타낸다. 그리고 3Di-hBN CuNi 복합체의 열전도율은 PM CuNi 합금보다 ~10% 더 높은 것으로 확인하였다. 3Di-hBN CuNi 및 3DiGr CuNi 복합체의 향상된 화학적 및 열적 안정성은 hBN과 그래핀의 불투과성 및 열 안정성, 즉 고온에서 원자, 이온 또는 분자의 침투/확산을 차단할 수 있는 능력 때문이다. 마찬가지로, 3DiGr CuNi도 PM CuNi 합금보다 58% 더 높은 열전도율, ~25.9% 항복 강도를 보였다. 3DiGr CuNi의 개선된 특성은 3차원의 그래핀 네트워크가 전자 이동성을 위한 전도 경로 채널을 제공하고, 외부에서 가해지는 부하에 대한 전위 이동을 차단하는 기능과 관련이 있는 것으로 보인다.

1 INTRODUCTION

Metal matrix composites (MMCs) are increasingly becoming the focus of research due to their outstanding properties in a wide spectrum of applications. Higher strength to weight ratio, corrosion resistance, wear resistance, damping capacity ,and thermal stability compared to the metals and alloys without reinforcement [1–9]. Moreover, the properties of MMCs can be modified depending on the application by exploiting the properties and morphology of the reinforcing material. MMCs are fabricated using a variety of techniques. However, powder metallurgy (PM) rout is one of the most efficient techniques for fabrication as the composites are produced at a relatively lower temperature than casting, minimising the likelihood of entrapment of unwanted impurities in the structure [10–12]. As a result, the mechanical, thermal, and tribological properties of MMCs prepared by PM route are improved. In addition, a wide variety of materials can be processed at relatively low production costs [13–15].

There are different types of reinforcement materials such as fibers, particles, and flakes to reinforce MMCs [16, 17]. MMCs reinforced by fibers such as SiC [18], boron [19], and Al_2O_3 [20] have been shown to exhibit better mechanical properties under the mechanism of load transfer. Nonetheles, when the matrix is reinforced by 2D materials such as graphene or hBN, it is referred to as reinforcement by flakes. Reinforcement by 2D materials is receiving enormous attention as it offers tremendous potential to improve properties for a wide range of applications [21–23].

This is because 2D materials have the potential to alter the properties of metals at the nanoscale. A single layer of hexagonal boron nitride (hBN) is structurally similar to graphene (carbon system) in which the hexagonal lattices are occupied by boron and nitrogen atoms. hBN has a lattice parameter of 25 nm and possesses extraordinary properties, such as high chemical stability [24], high mechanical strength [24], low density [25], high thermal stability [26], and high thermal shock resistance [27]. These excellent properties can be utilized to improve the performance of various

metal matrix composites (MMCs) through the in-situ construction of three-dimensionally interconnected (3Di) hBN layers in their grain boundaries. Similar approaches have been employed by other researchers, who used 3D-networked graphene to tailor the properties of MMCs [28–30]. For instance, Chen et al. [29] enhanced the yield and tensile strengths of copper by wrapping graphene around copper grains using chemical vapor deposition (CVD). They reported that the graphene acted as a barrier for dislocation movement, and consequently, the elastic modulus and strength were improved. Li et al. [28] reported that Cu-graphene composites had a higher thermal conductivity than pure copper because graphene offered an effective path for heat transfer between the Cu grain boundaries. Other properties, such as corrosion resistance and wear resistance, were improved also [31, 32].

Because of its structural similarity with graphene, the hBN introduced to metal matrices can also impart similar effects. Several researchers have used boron nitride nanoparticles to enhance the strength, hardness, wear, and corrosion resistance of metallic alloys [33–37]. For instance, the microstructure and properties of BN/Ni-Cu composites fabricated by powder technology were reported by Tantaway et al. [12]. They found that the BN content led to a decrease in density and an increase in the hardness, electrical resistivity, and saturation magnetization of the composite. Omayma et al. [25] fabricated Cu/hBN nanocomposites by the PM route, in which powder mixtures of Cu and hBN were compacted and sintered at various temperatures ranging from 950°C to 1000°C. They found that the physical, mechanical and tribological properties of the composite were influenced by the hBN. Still, however, to avail full benefit of hBN as a reinforcement material, much remains to be discussed.

Recently, various techniques have been utilized to fabricate reinforced MMCs through the incorporation of graphene. For instance, Xiong et al. [38] introduced graphene in Cu by the reduction of reduced graphene oxide through sintering. Similarly, ball milling, molecular-level synthesis, spark plasma sintering, and epitaxial growth have

been used to improve the strength of composites using graphene as a reinforcement [29, 39–42]. However, each of these strengthening techniques has some limitations. For instance, ball milling and molecular-level mixing may allow a uniform dispersion of the reinforcement material but may impart structural defects due to the shear stress and the contamination during the fabrication process. A well-ordered/-aligned, uniformly dispersed, and continuous graphene network is essential to attain the best reinforcement results [29]. Kawk et al. [43] introduced a simple, economically efficient two-step process with the potential to deliver better-quality products with uniformly dispersed and continuous graphene networks.

High-temperature oxidation is one of the major causes of component failure in power generation systems such as power plants, heat exchangers, etc. and is referred to as a material deterioration process in which metals and alloys react with oxygen to form oxides at high temperatures [44]. Similarly, metals and alloys deteriorate in a corrosive environment that leads to the loss of capital and sometimes catastrophic failure. Therefore, it is a matter of paramount importance to increase the resistance of metals and alloys against high-temperature oxidation and corrosion, in addition to improving their strength for structural applications. Various approaches such as mechanical alloying, composite coatings etc. were adopted for this purpose [45, 46]. Nonetheless, reinforcing with hBN via a simple two-step process PM route could be more economical and easier to conceive.

1.1 Contributions

In this work, three dimensionally interconnected hexagonal boron nitride networked $Cu_{0.7}Ni_{0.3}$ (3Di-hBN CuNi)and three dimensionally interconnected graphene networked $Cu_{0.7}Ni_{0.3}$ (3DiGr CuNi) composites were fabricated using a similar simple two-step process. We adopted a powder-based strategy to construct in-situ three dimensionally interconnected hexagonal boron nitride (or graphene) (3Di-hBN or 3DiGr) in Cu-Ni matrix through a simple two-step process, such that hBN (or graphene) layers surround

the grains of Cu-Ni matrix. Various characterization techniques were employed to confirm the formation of 3Di-hBN (or 3DiGr) surrounding the grains of the Cu-Ni alloys. CuNi-based alloys have been applied in various industries, such as shipbuilding, construction, and processing, owing to their high mechanical strength and corrosion resistance at elevated temperatures [47].

The reinforced composites are expected to deliver better corrosion, mechanical, and wear characteristics than the CuNi alloy. The properties of hBN and graphene were utilized to improve the mechanical, chemical, and thermal properties of the solid solution of Cu and Ni. For instance, the hBN/graphene is practically impermeable to almost all the ions and molecules and, thus the inclusion of three-dimensionally-interconnected hBN (3Di-hBN) is likely to enhance the resistance against chemical corrosion which is promoted by the transportation of ions at the interface of metal and corrosive electrolyte. Furthermore, hBN is stable at high temperature ($\sim$1000°C) and, therefore reinforcement of hBN into the Cu-Ni matrix is expected to improve the performance of 3Di-hBN CuNi composite at elevated temperatures. Moreover, the 3Di-hBN layer, a foam-like 3D porous structure, separated from 3Di-hBN CuNi composite can be applied in 3DiGr CuNifields of biomedicine, electronics, and energy storage [48–50]. In addition, the surface of three-dimensionally interconnected graphene-reinforced CuNi alloy can be modified to form a large-area network of graphene, which can potentially be used in energy applications such as current collectors for Li-ion batteries or as cathodes in fuel cells [51, 52]. To summarize,

1. 3Di-hBN CuNi and 3DiGr CuNi composites were synthesized using a simple two-step process that involve the compaction of metallic powders followed by chemical vapor deposition (CVD).

2. The composites were characterized with various characterization tools including OM, SEM, TEM, EDS and XRD analyses.

3. The influence of 3Di-hBN and 3DiGr on the mechanical, corrosion, and thermal properties was analyzed. We demonstrated that 3Di-hBN and 3DiGr improved the mechanical strength, corrosion resistance and thermal conductivity of the CuNi matrix.

1.2 Thesis Organization

The rest of this thesis is organized as follows. In chapter II, we review related literature on the synthesizing techniques, properties, and applications of MMCs. In chapter III, we introduce materials and methods used to synthesize and analyse the hBN and graphene reinforced CuNi matrix. Then, experimental outcomes are discussed in chapter IV. Finally, a brief summary and our conclusions on this work, and future scope of this work are given in chapter V.

2 BACKGROUND

2.1 Two-dimensional (2D) Materials

Nanomaterials can be broadly classified into zero-dimensional (Figure 2.1 (a)), one-dimensional (Figure 2.1), two-dimensional (b)), two-dimensional (Figure 2.1(c)), or three-dimensional (Figure 2.1 (d)) [53]. Zero-dimensional materials have all dimensions at the nanoscale, such as atomic clusters, nanoparticles, filaments, etc. When nanomaterials are nanoscale in one dimension, such as a surface film, they can be considered as one-dimensional. Fibers are the example of two-dimensional nanomaterials. Three-diomensional nanomaterials have no dimensions at nanoscale. These materials include bulk powders, multinanolayers, three dimensionally interconnected networks of 2D layers, etc. Each type is shown in Figure 2.1. Nanoscale materials have different physical, chemical, electrical, optical, and magnetic properties (than bulk materials) and are used in the field of nanotechnology.

Graphene is the first known 2D material consisting of a single layer of carbon atoms arranged in a hexagonal lattice. It was first isolated from graphite in 2004 by Novoselov and Geim using the scotch tape method. Since then, research on graphene and other 2D materials such as hexagonal boron nitride, borophene, etc., has advanced at a rapid pace due to their unique and fascinating properties and applications [55].

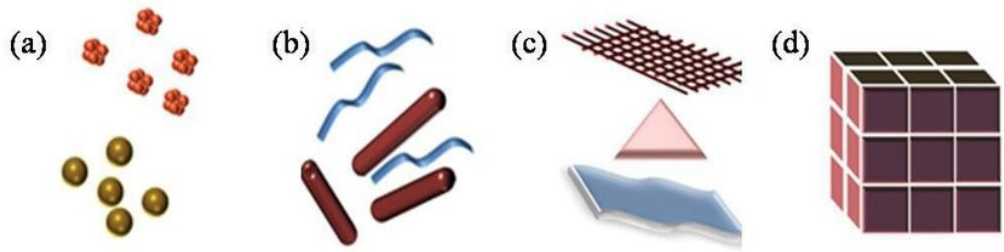

Figure 2.1: (a) Zero-dimensional clay and cluster (b) One-dimensional nanofibers, wires and rods (c) Two-dimensional plate and networks (d) Three-dimensional nanomaterials [54]. (Reused under a Creative Commons Attribution (CC BY) license. See Appendix 'E')

2.1.1 Hexagonal Boron Nitride

In recent years, much attention has been paid to 2D boron nitride (hBN), which is intrinsically an electrical insulator with an ultra-flat surface and an extremely stable structure. Although hBN is an electrical insulator, it can be tuned to have different properties and functionalities through various strategies incuding doping, substitution, functionalization, and hybridization [56]. It can also be used to tune the carrier mobility of other two-dimensional materials such as graphene, MoS_2, and two-dimensional black phosphorus when they properly interact due to the reduced Coulomb scattering and excellent interfacial properties. hBN protects these active materials from contamination, oxidation, and thermally/electrically induced degradation [56]. Due to the expected enormous technical potential, single- and multilayer hBN nanosheets have been successfully developed and investigated, and they have been shown to exhibit many attractive properties for technologically challenging applications, such as deep ultraviolet photonic devices [57], dielectric tunneling [58], power devices [59], electronic packaging [60], fuel cells, [61] and biomedicine [62].

Figure 2.2 (a) schematically shows the structure of hBN, in which boron and nitrogen atoms are alternately linked to form a hexagonal crystalline lattice structure.The unit cell is represented by red dashed lines in Figure 2.2(a). The lattice constants and other structural parameters are given in Table 2.1 [63].

Table 2.1: hBN structural parameters.

Lattice constants	Bond length	Interlayer spacing
a = b = 2.5 Å, c = 6.6 Å $\alpha = \beta = 90^\circ$, $\gamma = 120^\circ$	1.45 Å	3.3 Å

The boron and nitrogen atoms are arranged in a zigzag or armchair fashion, as shown in Figure 2.2 (b). Various geomatric configurations/patterns such as nanotubes, nanoflakes, nanoribbons, and naoscrolls can be derived from monolayers of hBN, as shown in 2.2 (c). Boron nitride nanotubes were first synthesized in 1995 by Chopra et

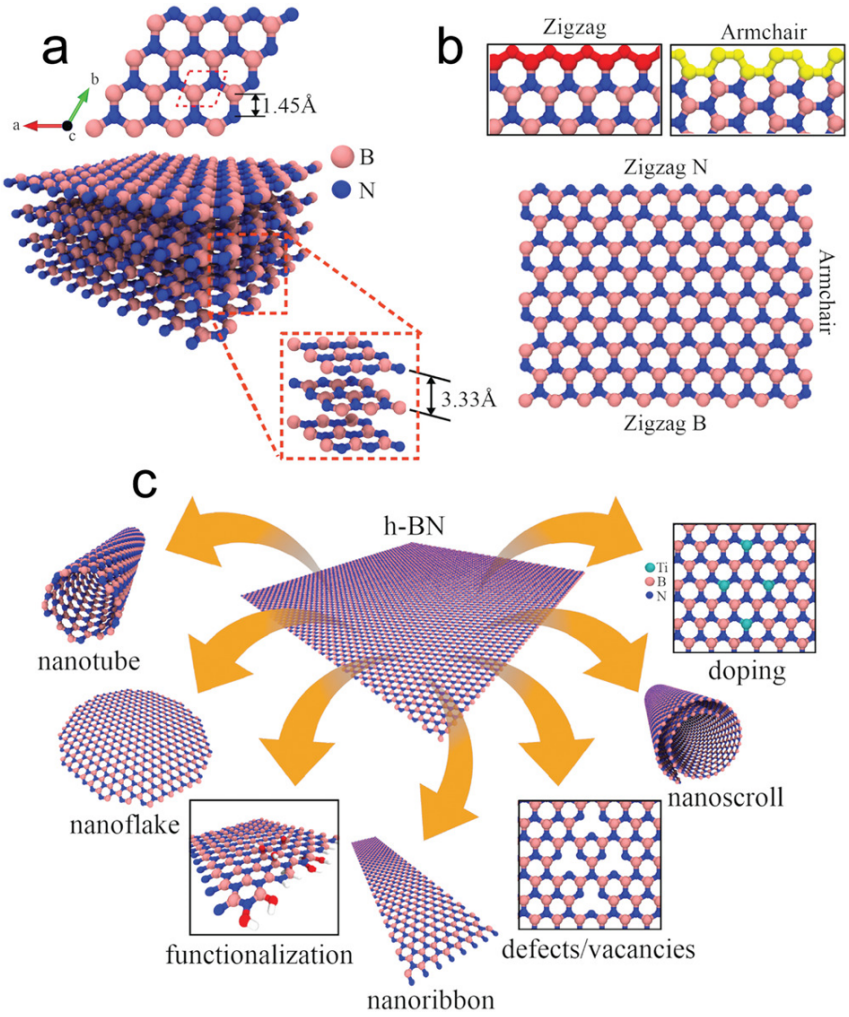

Figure 2.2: (a) Geometrical structure of hBN; the unit cell is represented in red dash lines (b) Displaying the probable atomic distribution of B and N atoms in different orientations [63]. (Reused with permission from John Wiley and Sons under license number 5179680229222. See Appendix 'E')

al. [64]. They reported that boron nitride can be transformed into various nanostructures like graphene. Boron nitride nanotubes can be single or multi-walled and, like carbon nanotubes, can have a variety of diameters and chirality. However, unlike carbon nanotubes, the properties of boron nitride nanotubes do not vary as a function of size

and chirality and tend to exhibit similar electronic properties to hBN with a large band gap around 6 eV.

Due to its excellent corrosion and oxidation resistance, hBN can be used as a dielectric and topcoat to protect the active material element and device from structural decay and chemical degradation [65]. Since hBN is electrically insulating, has a wide band gap of $\sim$6 eV, and is optically transparent, it can be used as a barrier and active layer to implement tunneling devices and tune the carrier dynamics and optical properties. Its high thermal stability (up to 1000°C in air and 1400°C in vacuum) [66], excellent thermal expansion coefficient (1-layer, 2-layer and 9-layer correspond to -3.41×10^{-2}, -3.15×10^{-2}, and -3.78×10^{-2} cm^{-1} K^{-1}, respectively), thermal conductivity (484 W m^{-1} K^{-1}), and excellent mechanical strength (elastic constant of 220-510 Nm^{-1} and elastic modulus of 1.0 TPa) [67, 68] further make it a suitable candidate for other applications such as reinforcing the polymer and metal matrix composites. Of course, the quality of 2D nanosheets mainly affects the performance of hBN-based devices. Therefore, the synthesis process must be tightly controlled to synthesize high-quality hBN with minimal defects. This has led researchers to develop new strategies to control the growth process and understand the mechanisms of formation [68, 69].

Despite the great progress made so far, current research on hBN still faces three major challenges: (a) growth of hBN at large scale with controlled layer quality and appropriate transfer technology, (b) integration of hBN into other nanomaterials, polymer and metal matrices, (c) effective modulation of electronic structures by other strategies (including energy bands and charge carriers) in hBN [70].

2.1.2 Graphene

Graphene is a single layer of carbon atoms that are connected in hexagonal lattice to form honey comb structure. Thanks to its excellent thermal, mechanical, structural and optical properties [71–74], graphene has gained a huge attention of research scientists.

These outstanding properties are shown by graphene because of its unique electronic structure and hexagonal arrangement of carbon atoms in lattice [75]. Graphene could be combined with other materials to synthesize graphene reinforced metal matrix composites (Gr-MMCs). Such composites take the benefit of extraordinary properties of graphene and, therefore, also exhibit excellent properties.

Carbon atom has electronic configuration of $1s^2$ $2s^2$ $2p^2$. When two carbon atoms combine together, sp^2 hybridization occurs because one electron from 2s orbital transfers to 2p-orbital thereby bringing three orbitals 2s, 2px, and 2py to same energy level [76]. This enables single carbon to form strong covalent bond with three carbon atoms thus forming a hexagonal lattice [77]. The C-C planar sigma bond has bond length of 0.142 nm imparts graphene exceptionally high planar strength [78]. Excellent functional properties of graphene are imparted by unhybridized 2pz orbitals which form delocalized electronic clouds over the hexagonal ring [79]. Due to unique atomic structure and electronic interactions, Dirac cones are formed at each edge of hexagonal ring. Graphene has zero bandgap nature because of these Dirac cones [80]. High charge carrier mobility of graphene results in its excellent thermal and electrical conductivities because of the presence of massless Dirac fermions and ballistic charge transport [81].

As mentioned earlier, the properties of graphene depend on the structure of carbon lattice and functional groups associated with each of its derivatives. Graphene derivatives can be classified into several types based on layers number, functional groups and crystallographic structure [82]. On the basis of number of layers, the graphene derivatives are categorized into single-layer graphene, few layered graphene (FLG), multilayered graphene (MLG), and graphene/graphite nanoplatelets (GNPs) [83]. In addition, graphene has excellent mechanical properties; the tensile strength of graphene measured by the experiment is about 130 GPa [71], which is 100 times that of ordinary steel; its fracture strength can reach 42 Nm^{-2}, about 200 times that of steel [71]. At the same time, the elastic elongation of graphene is also higher than that of all other

crystals, and the elongation rate can reach 20%; the elastic constant of graphene is 1∼ 5 Nm^{-1}, and the Young's modulus is as high as 1.02 TPa [71]. These excellent properties of graphene materials generated huge interests in applying it in a myriad of device and in the fields of thermoelectric and optoelectronic devices, ultrastrong paper-like materials, electrocatalysts, novel composite materials, energy conversion materials, and so on. Figure 2.3 shows the overview of applications of graphene in various sectors. In this dissertation, the potential of graphene to reinforce metals and alloys will be focused.

Figure 2.3: Overview of applications of graphene in different sectors [84]. (Reused under a Creative Commons Attribution (CC BY) license. See Appendix 'E')

Graphene and hBN materials hold a prominent position among nanomaterials due to their colossal potential to improve the properties of metals and alloys [16]. In order to benefit from their typical functional and structural properties, scientific community

continues to research on developing MMCs reinforced by graphene or hBN. Despite of all the researches that have been performed on this topic, there are still some gaps which need to be filled and true potential of graphene or other 2D materials is yet to be explored. The fabrication techniques to develop 2D reinforced metal matrix composites (MMCs) are continuously flourishing; efficient and economical methods need to be introduced for the fabrication of 2D materials reinforced MMCs.

2.2 2D Materials Metal Matrix Composites

Metal-matrix composites are metals or alloys that incorporate particles, whiskers, fibers, or hollow micro balloons made of a different material, and offer unique opportunities to tailor materials to specific design needs [85–87]. These materials can be tailored to be lightweight and with various other properties including high specific strength and specific stiffness, high hardness and wear resistance, low coefficients of friction and thermal expansion, high thermal conductivity, and high energy absorption and a damping capacity [87]. In addition to these properties, new MMCs are being developed with self-healing, self-cleaning, and self-lubricating properties, which can be used to enhance energy efficiency and reliability of automotive systems and components [88]. Since the last three decades, metal matrix composites (MMCs) have been intensively studied in order to develop high performance materials exhibiting distinguished properties.

MMCs can be reinforced by fibers, particles, or flakes [16, 17]. Fibers such as SiC [18], boron [19], and Al_2O_3 [20] were used to improve the mechanical properties of the matrix through the mechanism of load transfer. Reinforcement by particles such as BN, SiC, Al_2O_3, etc. has also been used by researchers to improve the hardness and tribological properties of the matrix [16]. However, reinforcement by flakes, including 2D materials such as graphene or 2D hexagonal boron nitride (hBN), is increasingly seeking the attention of researchers because of their colossal potential to improve the

mechanical, thermal, chemical, and electrical properties of the matrix [21–23].

2.3 Current Challenges for Fabricating 2D Materials MMCs

Proper dispersion of graphene/hBN in a metal matrix is essential to achieve MMCs with desired properties. The incorporation of graphene/hBN should be carried out such that there is no agglomeration, uniform distribution, good interfacial attachment, and proper structural integrity. Agglomeration occurs as a result of Van der Waal's forces between graphene sheets [89]. Commonly, graphene reinforced metal matrix composites (Gr-MMCs) are fabricated using graphene nano plates and multi layer graphenes which contain 10∼100 layers of carbon atoms [90]. As a result, there is a big difference in properties between these multilayer graphene derivatives and single layer graphene. With the multilayer graphene derivatives, agglomeration is one of the basic problems because this can unavoidably lead to the large porosity in the structure of MMCs. This may in turn cause premature failure of the composite because of premature crack initiation and propagation [21, 91, 92]. Another serious concern is the inhomogeneous dispersion of graphene in metal matrix [93] which leads to the poor properties of MMCs. Inhomogeneous distribution of graphene results in increase in porosity and decrease in yield strength, thermal, and electrical conductivities of composite [94]. Furthermore, in order to ensure good properties of MMCs, wettability between the reinforcement material and metal matrix is also an important parameter to consider. If the wettability is low, there is weak interface between enforcement material and metal matrix and hence composite is expected to possess low strength [83]. Unfortunately, conventional methods of fabricating MMCs impose harsh processing conditions leading to deteriorating the actual structure of graphene. Various types of deteriorations include thermal decomposition of graphene, high defect density in graphene sheets and lateral size reduction etc. [95, 96]. It must be noted here that the hBN is structurally analogous to graphene having almost all comparable properties to graphene. In this perspective, the

challenges toward the development of hBN reinforced metal matrix composites (hBN-MMCs) are the same as towards the development of Gr-MMCs. In the coming section, we therefore present various processing techniques to fabricate Gr-MMCs with their advantages and limitations.

2.4 Fabrication Methods

Incorporation of graphene in metal matrices has been carried out by utilizing various techniques since last decade [8, 95, 97]. The main focus was to address the aforementioned challenges in the fabrication of Gr-MMCs. The processing techniques can be broadly classified into following classes.

1. Mechanical alloying (MA)
2. Semi powder metallurgy (SPM)
3. Molecular-level mixing (MLM)
4. Electrochemical deposition (ELD)
5. In-situ growth

The forthcoming section illustrates an overview of processing techniques to highlight their scope and applications.

2.4.1 Mechanical Alloying (MA)

MA involves the mixing and blending of graphene and metal powders. This technique is widely being employed for fabrication of Gr-MMCs [98–102]. Mixing and blending are mostly carried out by using ball milling technique which not only blends the graphene and metallic particles but also controls the morphology of metallic powders. During the ball milling process, metallic particles are subjected to severe shear stress and therefore

their fracture occurs. This ensures the good distribution of graphene in metal matrix. Also, interfacial attachment between graphene and metal matrix is controlled by various processes occurring during ball milling such as cold welding, particle fracture and rewilding of metallic powders [21].

Dispersion of graphene in metal matrix depends upon various factors such as milling medium, time, atmosphere, graphene content and ball to powder ratio. It is obvious that longer milling time will ensure better dispersion. However, if milling time is too long, this would adversely affect the morphology of graphene [96, 103]. Post blending process includes compaction and consolidation of composite powders. Compaction and consolidation can be carried out in single step such as press sintering [96]. Nonetheless, compaction and sintering could be performed in separated stages as well. Furthermore, efficient alternatives have also been employed for consolidation of composite powders [100]. For example, spark plasma sintering (SPS), and microwave sintering processes are considered best alternatives of conventional sintering. As the essential outcome of sintering process, however, there is always porosity in the structure which causes in the weakening of properties of the composites. Some researchers have also utilized some further processing on the sintered samples in order to improve properties. These processing techniques include hot extrusion, rolling, annealing etc. [104]. Extrusion and rolling can help in bringing partial alignment of graphene sheets. Several metals and alloys such as Cu, Ni, Ti based alloys etc. have been processed through MA to incorporate graphene.

2.4.2 Semi Powder Metallurgy (SPM)

SPM, also known as solution mixing, is widely used technique to address the challenges of dispersion and interaction of graphene with metal matrix. SPM is different from MA in a sense that it uses solvent (liquid) to disperse the graphene in metallic powders [105, 106]. The advantage of using solution mixing is that it not only provides

good mixing but the structure of graphene is also preserved [106, 107].

The process is carried out in the following steps. Initially, graphene reinforcement is dispersed in the solvent by using sonication. This is followed by the mixing with metallic powders [108]. In order to get uniform distribution of graphene, several blending processes such as ball milling, mechanical mixing and ultrasonication are performed on composite powder [108]. Then solvent is removed by filtering process followed by the drying and heat treatment processes under reducing environment to remove any oxides. Next, consolidation is performed either by conventional sintering, hot pressing or SPS [108]. The schematic of SPM is shown in Figure 2.4.

In SPM process, surfactants are also used to provide better interfacial attachment between graphene and metal particles [108]. These surfactants enhance interaction either by electrostatic interaction or by covalent bonding. This method has tunable processing parameters and can be employed on industrial scale. Various materials such as Al, Ni, Cu, Fe, Ti, Mg etc. have been processed by using this technique [22].

2.4.3 Molecular-level Mixing (MLM)

MA and SPM are good at overcoming the graphene dispersion problem. However, due to low wettability of graphene, interfacial bonding between graphene and metal matrices is not strong enough to deliver the desired properties [108, 110]. Strengthening efficiency can be improved by employing a molecular-level bonding at the interface [111]. In molecular-level mixing technique, graphene sheets are first exfoliated by ultrasonication, then mixed and dispersed with metal salts and lastly, metallic ions are reduced on graphene sheets to give metal-decorated reduced graphene sheets in the form of powder [112]. The most commonly used graphene reinforcement material for MLM is graphene oxide (GO). Presence of functional group on GO surface results in strong interaction between GO and other atoms [113, 114]. Metallic ions find nucleation sites on GO surface because of the existence of oxygen-based functional groups on GO surface. In

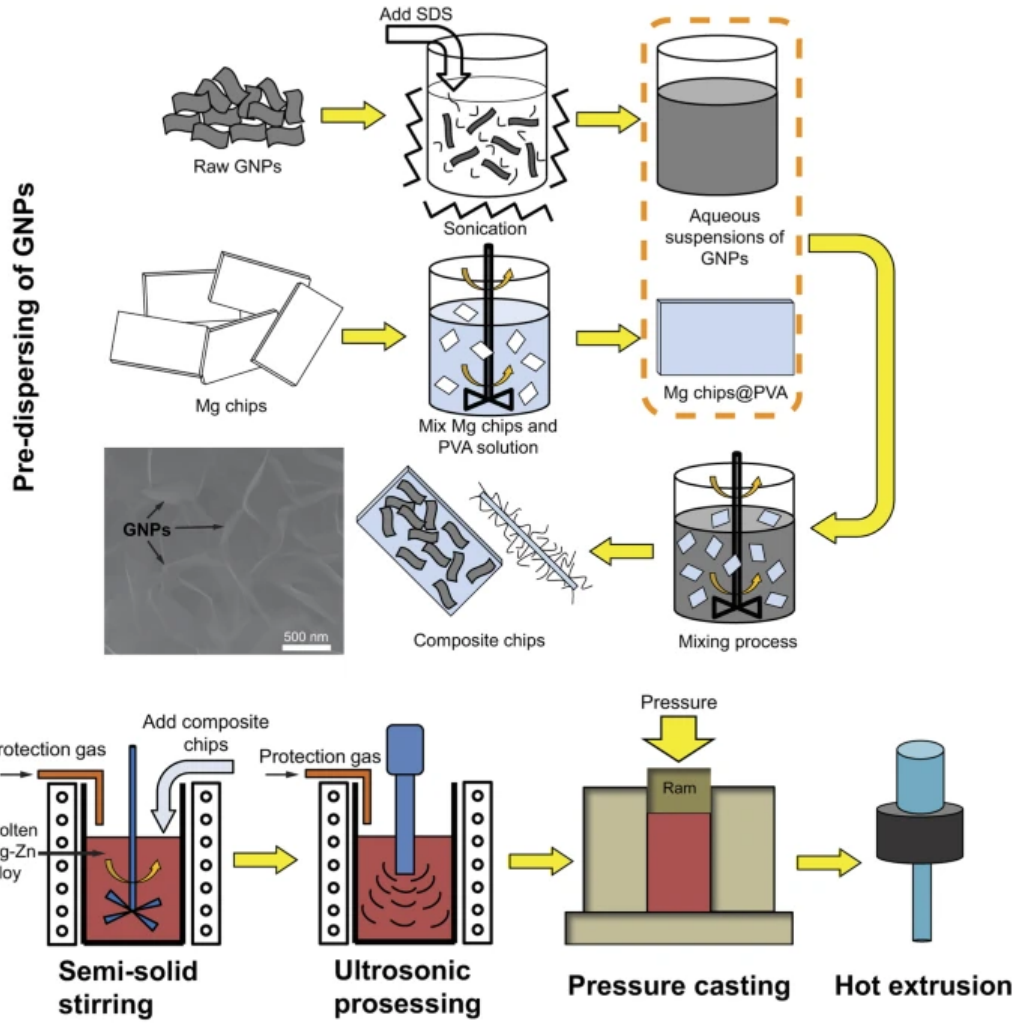

Figure 2.4: Fabrication procedure of the composites by SPM [109]. (Reused under a Creative Commons Attribution (CC BY) license. See Appendix 'E')

this way, strong covalent bonding between metal and carbon atoms is formed due to these functional sites which would not be possible otherwise [115]. The consolidation of the composite powder (metal-decorated reduced graphene) can be carried by conventional sintering processes, hot pressing or SPS [116, 117]. MLM process is schematically shown in Figure 2.5.

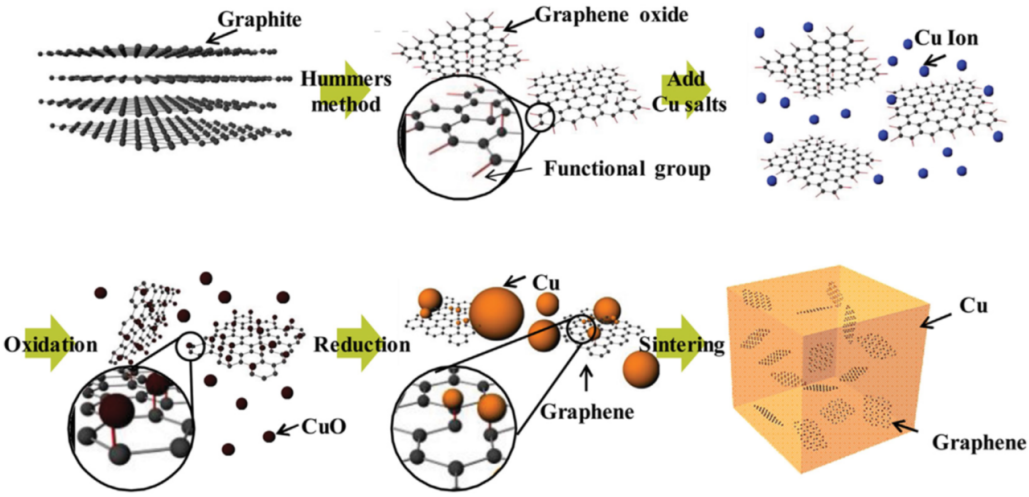

Figure 2.5: Schematic diagram of MLM process for preparing rGO/Cu composite materials [118]. (Reused with permission from John Wiley and Sons under license number 5179690150881. See Appendix 'E')

MLM improves not only wettability between graphene and metal particles but also helps prevent the agglomeration of graphene sheets. Metallic particles attached on the graphene surface during MLM process also act as spacers thereby preventing agglomeration. However, MLM is mostly limited to Cu only because of the ease of the attachment of copper ions on GO surface. Some reports have also included attachment of Ni, Ag, and Mg particles on graphene surface, whilst using metal decorated graphene sheets as reinforcement in Cu, Al, and Ag matrix composites [119].

2.4.4 Electrochemical deposition (ELD)

ELD is considered a reliable technique to fabricate graphene reinforced metal matrix coatings. This technique is known for many attributes such as low cost, high yield, and customizable processing parameters [120, 121]. In this process, electrochemical cell is used that contains plating solution, target electrode, and power source to provide electric current as shown schematically in Figure 2.6.

To fabricate graphene reinforced MMCs coatings, graphene is dispersed in plating

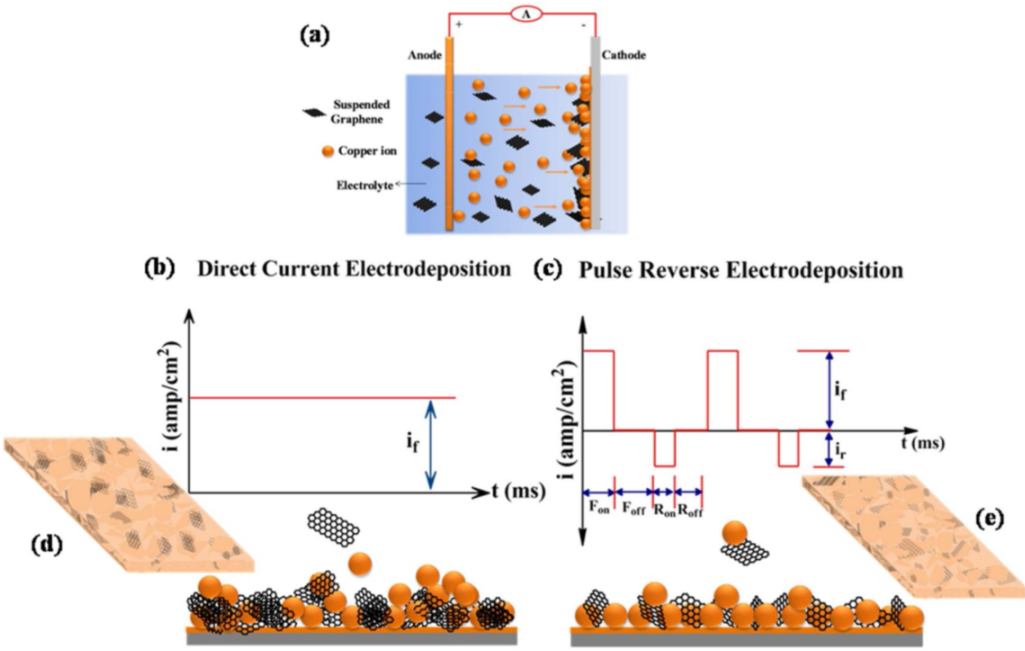

Figure 2.6: (a) Experimental setup of electrodeposition, (b) and (c) Schematic representation of the current waveforms and the co-deposition of Cu and Gr, (d) and (e) Cu-Gr nanocomposite foils prepared by DC and PRED, respectively [122]. (Reused under a Creative Commons Attribution (CC BY) license. See Appendix 'E'.)

solution containing metallic ions, by using ultra sonication. When current is applied, graphene sheets along metallic ions are deposited on the target electrode; thereby generating graphene reinforced MMCs coatings. Constant stirring in the electrochemical bath is required so that graphene sheets do not aggregate and hence graphene is uniformly deposited. Additionally, surfactants are also used to enhance dispersion of graphene sheets in plating solution and hence their distribution in metal matrix [123]. Since ELD process is driven by external power source, the parameters for current have a direct effect on morphology of deposited coating, including grain size, microstructure, and graphene distribution along the metal matrix. The parameters which affect the properties of the deposit to the most are current density, current flow type, deposition time, external voltage, bath composition, and concentration of graphene. ELD has been used to fabricate

graphene-reinforced composite coatings with metal matrices such as Cu, Al, Co, Ni, and Cr.

2.4.5 In-situ Growth

In this process, metallic powder is mixed with carbon or hBN source and is subjected to high temperature in a chemical vapor deposition (CVD) furnace. The source dissociates to constituent atoms which diffuse into metal particles at high temperature [124]. After diffusion, these atoms join together to form graphene (or hBN) surrounding the metal grains. In this way, graphene is dispersed and attached with metal interface without any damage to graphene lattice. Graphene embedded powder can then be consolidated using hot pressing, compaction, and conventional sintering or SPS [125]. The basics of in-situ growth of graphene are simply to grow graphene on metallic particles, which are then subjected to consolidation without the need of any further processing [29]. Schematic diagram is shown in Figure 2.7. A solid or gaseous carbon source supplies carbon atoms, which undergo deposition at high temperature, typically in a CVD furnace. Similar to other techniques, many different routes have been investigated for in-situ growth of graphene in metal matrix. Type of carbon source, carbon quantity, growth temperature, and growth time are the key parameters which effect the crystallinity, number of layers and hence quality of graphene layers [126]. In order to enhance distribution of graphene layers, preprocessing is also carefully carried out to ensure a good mixing and hence maximized interaction of carbon source with metallic particles [127].

The in-situ processing technique is widely being used because of its simplicity and applicability. The fabrication of composites containing well-ordered (aligned) and uniformly dispersed graphene composites via in-situ method could be economically preferred option. Various studies suggest that strength of materials can be increased without any compromise on their other properties such as thermal and electrical

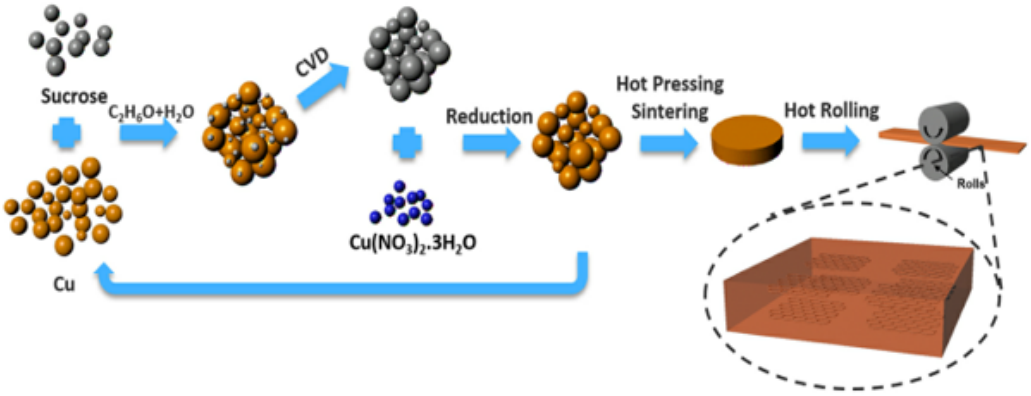

Figure 2.7: Schematic illustration of the in-situ growth for graphene reinforced Cu composite [127]. (Reused with permission from Elsevier under license number 5179690877080. See Appendix 'E')

conductivities, corrosion resistance etc. Some researchers [29, 43, 126, 127] introduced a simple two-step process which comprises simply two steps, i.e. powder compaction and CVD. The spaces in the compacted sample act as catalyst sites (template) for graphene growth during CVD. This method ensures not only uniform dispersion of graphene in matrix but also helps in the formation of three dimensionally interconnected network of graphene surrounding the grains of matrix [43]. Thus, this process has potential to improve mechanical, thermal, chemical and wear properties simultaneously.

Zhang et al. [128] developed a powder metallurgy-based strategy to fabricate 3DiGr-Cu composites, in which a three dimensionally interconnected graphene network (3DiGr) is grown in-situ on Cu powder by rapid thermal annealing. During CVD process, 3DiGr directly adheres to the Cu grains to form a three-dimensionally interconnected graphene network in the composites due to the discrepancy of the thermal expansion coefficient and the associated thermal stress between 3DiGr and Cu. Thus, the highly interconnected nature of 3DiGr is not only leads to the better load transfer capability and higher strengthening efficiency, but also greatly minimizes the scattering of electrons at the interfacial regions, creating pathways for electron transport throughout the matrix.

This leads to an improvement in mechanical properties as well as electrical and thermal conductivities, simultaneously. Furthermore, this viable bottom-up approach to forming graphene into a continuous network architecture during powder consolidation can open new avenues for designing 3D network structures from 2D building blocks in metal matrix composites, without the pervasive limitations of currently used melting-related processing methods.

In our research, we proposed an in-situ growth route starting from CuNi powders and using a simple two-step process. Here, the whole fabrication process of 3DiGr CuNi or 3Di-hBN CuNi composites could be mainly divided into two steps; compaction and CVD (or MOCVD). We have applied this method for the synthesis of graphene or hBN reinforced CuNi composites and accomplished excellent results in terms of properties and applications.

2.4.5.1 Process Chemistry of In Situ Growth via CVD (or MOCVD)

In general, when CVD is performed with transition metal substrates, two types of diffusion mechanisms can cause the crystal to grow. These two mechanisms are referred to as surface-mediated growth and diffusion precipitation growth [129]. Which mechanism dominates mainly depends on the solubility of the growth species in the substrate, in addition to other CVD parameters such as temperature, pressure and cooling rate, etc. [130].

Based on C isotope labelling, it has been reported that graphene grows by surface diffusion when the solubility of C in the substrate (e.g. Cu) is low [130]. C diffuses on the substrate surface and its concentration increases. When a critical supersaturation reaches, nucleation occurs and crystals grow as shown schematically in Figure 2.8. Thus, the growth of graphene is entirely controlled by a vapor-surface reaction, commonly referred to as a self-limiting growth process (surface-mediated growth). In comparison, growth in metal substrates with high C solubility occurs through the segregation of C from the saturated substrate (e.g. Ni) [130]. This process involves diffusion of active C species

into the bulk substrate until the solubility limit is reached, at which point nucleation occurs through precipitation-segregation process (diffusion-precipitation growth) as shown schematically in 2.8. Even though the CVD growth of single-layer graphene on Cu is self-limiting, it is challenging to obtain a large area single crystal and to control the number of graphene layers. Especially, if 3DiGr is to be built up along the Cu grain boundaries of the sintered disk. On the other hand, the use of a Ni substrate leads to inhomogeneous graphitic films with different thicknesses due to the high C-solubility of Ni [131].

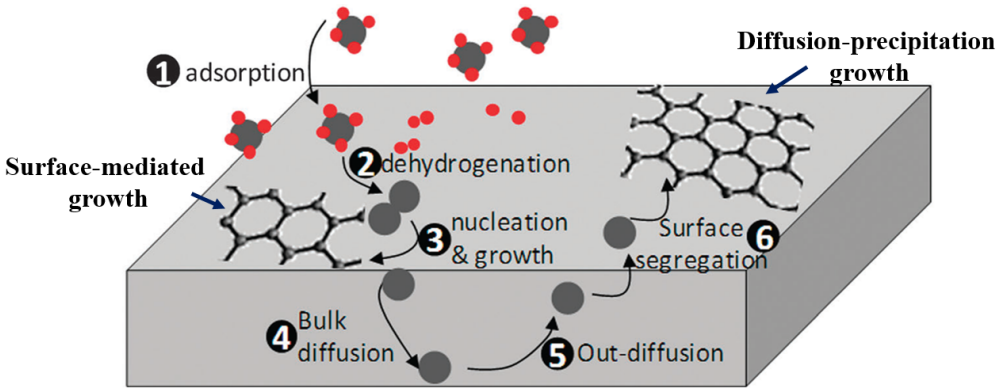

Figure 2.8: Schematic illustrating the surface-mediated and diffusion-precipitation growth mechanisms [131]. (Reproduced with permission from Royal Society of Chemistry. See Appendix 'E')

Both theoretical studies and experimental investigations have shown that alloying Ni with Cu decreases the solubility of C in the Cu-Ni system. The combination of the high catalytic activity of Ni with the low C solubility of Cu is a promising way to control the number of graphene layers during CVD growth [132]. Xie et al. reported the growth of bilayer graphene (BLG) with a domain size of 300 micrometers AB -stacked using Cu vapor on a 25 micrometer thick electrodeposited Cu85-Ni15 alloy (by atomic ratio) [133]. Liu and co-workers achieved 95% coverage of single-layer graphene (SLG) on a 300 nanometer thick Cu94.5-Ni5.5 film substrate; however, increasing the Ni content to 10.4% produced 89% BLG [134]. Ruoff et al. investigated the CVD of graphene on

commercial Cu31-Ni67.8 and Cu90-Ni10 alloys (by atomic ratio); they found that the thickness of the deposited graphene is affected by both the growth temperature and the cooling rate [135, 136]. A thin film of Cu-Ni alloy was previously used to synthesize graphene by Jeon et al. who found that the number of graphene layers can be controlled by controlling the Ni content in the Cu-Ni thin film [137].

The increasing thickness of graphene with increasing Ni content correlates with the increase of C solubility at higher Ni content. Moreover, the introduction of Ni increased not only the C-solubility but also the catalytic activity of the alloy for the decomposition of hydrocarbons. The C-solubility of the growth substrate should also affect the growth time of the graphene. Figure 2.9 shows the time required to grow a graphene film (e.g. SLG, BLG) as a function of Ni content and compares it with the C-solubility values of each alloy. As one can see, the growth time increases as the C solubility of the Cu-Ni alloy increases. This observation is consistent with the fact that CVD graphene growth on Cu-Ni alloy is a bulk diffusion precipitation process. When the hydrocarbon ($-CH$) interacts with the metal surface, C atoms are released by breaking the $C-H$ bond and diffuse into the bulk metal. The C concentration in the metal bulk increases up to the solubility limit for a given substrate. When the precursor supply is stopped and the substrate is cooled, growth of graphene occurs by C precipitation on the surface. The incubation time (the time required to reach the solubility limit) depends on the growth parameters (temperature, pressure, and composition of the starting material) and the C solubility. The two competing mechanisms (surface-mediated and diffusion-precipitation) lead to the growth of 3DiGr in CuNi composites. Due to the increased solubility from 0.001 at. % to 0.03 at. % with the addition of Ni (30 wt.%) in Cu, however, would lead to the dominance of diffusion-segregation mechanism.

When mixed CuNi powders of CuNi are densified, the vacant spaces between the particles serve as a template for graphene growth. During the CVD process, carbon atoms easily enter each part of the disc through the vacant spaces and two processes

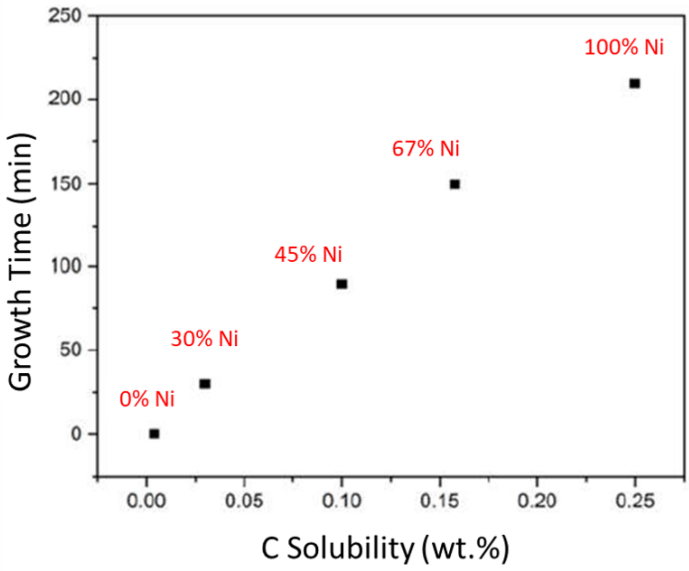

Figure 2.9: Change of C solubility with Ni content and its effect on growth time [132]. (Reused under a Creative Commons Attribution (CC BY) license. See Appendix 'E')

could take place. Some of the C atoms nucleate heterogeneously when the concentration reaches a supersaturation level, and thus the graphene grows along the grain boundaries of the CuNi solid solution. In other words, the grain boundaries serve as a active sites for graphene growth by surface-mediated growth process. However, some of the C atoms dissolve in the CuNi solid solution to form the CuNi-C solid solution, in which the C atoms occupy the interstitial sites of the FCC-CuNi alloy. These carbon atoms precipitate out (segregation) upon cooling and thus graphene grows along the grain boundaries of the CuNi alloy. We believe that the mechanism of diffusion-segregation dominates over the surface-mediated growth for graphene growth in our system due to the increased solubility of C atoms by Ni. Hu et al. have shown that the solubility behavior of B and N in transition metals is similar to that of C [138]. Therefore, we can assume that the growth of hBN in CuNi solid solution is similar to that of graphene in CuNi solid solution.

2.5 Applications of Gr/hBN MMCs

2.5.1 Mechanical Properties

MMCs reinforced by 2D materials have shown excellent mechanical properties including yield strength, tensile strength, toughness and etc. Chu et al. [21] found that Gr-Cu composite showed enhancement in yield strength and Young's modulus upto 114% and 37%, respectively compared to unreinforced Cu. Chen et al. [29] investigated on in-situ grown graphene reinforced Cu matrix composites and found 177% and 27.4% enhancement in yield and tensile strength over pure copper. Similarly, various researchers have observed a substantial increment in mechanical properties of the metal matrix as shown in Table 2.2. Shu et al. [139] reported the improved mechanical properties of Cu/Ti_3SiC_2/C nanocomposites due to synergetic effect of graphene and hBN. The mechanisms explaining the reinforcing effect of graphene (or hBN) are given below:

Table 2.2: Mechanical properties of graphene reinforced MMCs.

Processing method	Ultimate tensile strength (MPa) (Compared to Cu)	Reference
MLM + SPS	319 (increase 25%)	[140]
Sonication + Spark plasa sintering	131 (decrease 24%)	[92]
Ball milling + Equal speed rolling	315.1 (decrease 0.7%)	[98]
A in-situ two-step process	218 (increase 20%)	[141]
Sonication + Hot pressing	271 (increase 18%)	[142]
Ball milling + Sparking plasma sintering	355	[143]
In-situ growth + Hot pressing + Hot rolling	275 (increase 27%)	[127]
Ball milling + in-situ growth + Hot pressing	274 (increase 27.4%)	[29]

2.5.1.1 Load Transfer

3DiGr or 3Di-hBN, having strong interfacial bonding to the metal matrix, can transfer the externally applied load. This network carries the applied load as a whole rather than as isolated graphene or hBN pieces. Therefore, the overall strength of the reinforced composite is enhanced [29]. The mechanism of load transfer is shown in Figure 2.10.

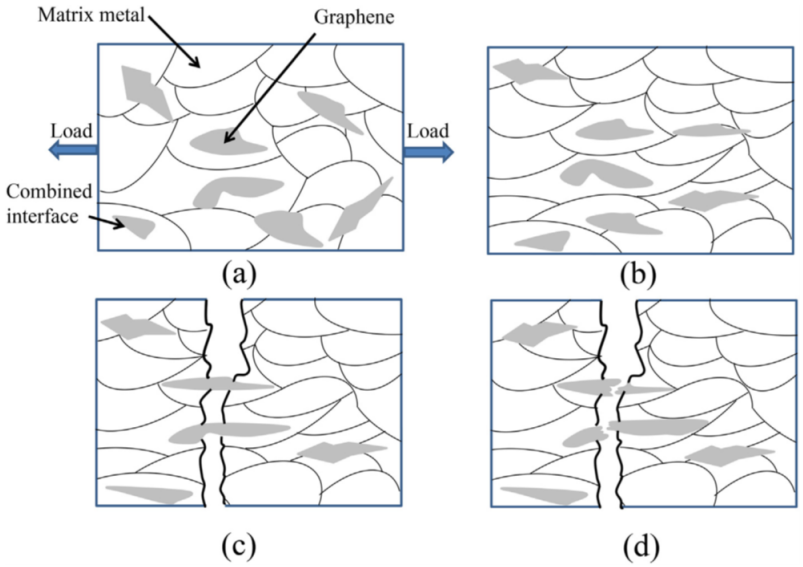

Figure 2.10: Schematic diagram of load transfer: (a) the initial composite material with randomly distributed graphene (b) the matrix deforms and the graphene rotates after being stressed (c) the graphene is deformed and elongated and (d) the graphene finally breaks [144]. (Reused under a Creative Commons Attribution (CC BY) license. See Appendix 'E')

Figure 2.10 (a) shows the perfect interfacial bonding of graphene to the matrix and the strong bonding. This bonding leads to effective transfer of stress to the matrix (Figure 2.10 (b)) when the load is applied along the 2D direction, as shown in Figure 2.10 (a). When a load is applied, the matrix is initially stretched and deformed, which causes the graphene to be elongated and deformed as well (Figure 2.10 (c)). Therefore, the final rupture is further delayed. However, when the load is further increased, the structure of the graphene deforms significantly and finally breaks (Figure 2.10 (d)).

Yan's et al. reported that the mechanism of load transfer increases yield strength of the composite according to the following equation (2.1) [145].

$$\sigma_{YS} = (\sigma_0 + kd^{\frac{-1}{2}})[\frac{V_f(s+4)}{4} + (1 - V_f] \tag{2.1}$$

where σ_0 and k are constants associated with the crystal type, d is the matrix size,

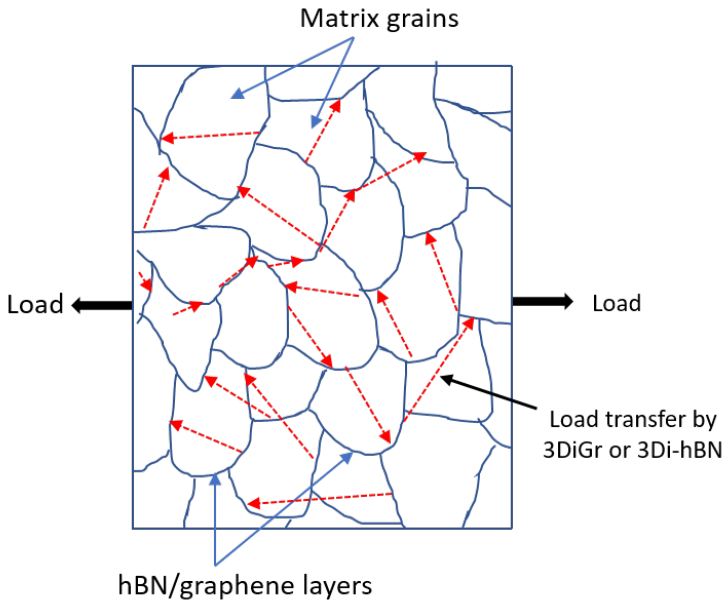

Figure 2.11: Load transfer by 3D interconnected network of 2D layers.

V_f is the graphene's volume fraction, and s is the aspect ratio of the graphene. This equation (2.1) shows that for a given value of V_f, a higher value of aspect ratio leads to a higher yield strength. The theoretically predicted value of yield strength of graphene-Ni/Cu composites based on this model agrees with the experimental results [146]. The load transfer mechanism is considered to be the main reason for increasing the strength of the composite. However, this mechanism ignores other negative effects such as agglomeration, especially when the content of 2D reinforcement is too large. Theoretical studies [104] revealed that the efficiency of load transfer effects within Gr-MMCs is determined by the aspect ratio, dispersion, orientation direction of graphene and interfacial structure. Furthermore, load is also transfered by architecture of 2D layers as shown schematically in Figure 2.11. Load is transfered by one layer to other connected layer and in this manner the entire interconnected network absorbs the load to increase the strength of the composite.

2.5.1.2 Dislocation Strengthening

When external load is applied on the composite, the graphene or hBN can act as a barrier to inhibit the dislocation motion, leading to the dislocation accumulation nearby the interface [147]. Chu et al. [148] explained that improved tensile properties of Gr-Cu composites can be attributed to the accumulation of dislocations at metal-graphene interfaces after tensile deformation.

2.5.1.3 Grain refinement

The inclusion of graphene or hBN in the metal matrix is quite likely to inhibit the grain growth during the synthesis process which leads to refinement in the microstructure [21]. The grain size affects the yield and tensile strength of the sample according to the classic Hall-Petch equations [149, 150]:

$$\sigma_{YS} = \sigma_{YS} + k_{YS} d^{-1/2} \tag{2.2}$$

$$\sigma_{UTS} = \sigma_{UTS} + k_{UTS} d^{-1/2} \tag{2.3}$$

where, σ_{YS} and σ_{UTS} correspond to the yield strength and the ultimate tensile strength, respectively. These equations indicate that the strength of a material increases with the decrease in grain size.

2.5.2 Thermal properties

Graphene has high thermal conductivity, so its inclusion in the metal matrix composite would increase the thermal conductivity. Zhang et al. [128] found that three-dimensional network of graphene in Cu matrix contributed to more than 10% increment in thermal conductivities. They explained their findings by conducting molecular dynamic simulations to prove that three-dimensional network of graphene provides effective conducting path channel for electrons and phonons motion. Li et al. [28] adopted a simple two-step process route to fabricate three dimensionally interconnected network

Table 2.3: Thermal conductivities of graphene reinforced MMCs.

Processing methods	Thermal conductivity (W/m · K)	Reference
Electrodeposition	300.5 (increase 5%)	[151]
MLM + SPS	362 (decrease 3%)	[152]
Stirring + Hot pressing	370 (increase 3%)	[153]
Pasting on Cu foil	445.91 (increase 34%)	[154]
Ball milling + SPS	359 (increase 8%)	[155]
In-situ two-step process	409 (increase 70%)	[28]
Ball milling + Hot pressing	296 (increase 15%)	[156]
MLM + SPS	294 (decrease 18%)	[157]
Ball milling + Hot pressing	253	[158]
Sonication + Vacuum infiltration +SPS	375 (increase 10%)	[159]

of graphene Cu composite and found a substantial increase in thermal conductivity. Table 2.3 summarizes the thermal conductivity of graphene reinforced Cu composites produced via various processing methods.

2.5.3 Corrosion Properties

One of the important applications of 2D materials is their ability to increase the corrosion resistance of MMCs. Graphene and hBN are impermeable to ions, molecules and atoms [160]. Therefore, they can hamper the transfer of ions and molecules across the interface and as a result, increase the corrosion resistance of the composite. Mahveash et al. [160] reported that the CVD grown hBN reduces the Cu corrosion rate by an order of magnitude compared to bare Cu. Li et al. [161] investigated the corrosion resistance of three-dimensionally interconnected networked graphene-Cu composite by potentiodynamic polarization tests and concluded that three-dimensional graphene structure effectively protected the Cu against corrosion. Because of impermeability, graphene or hBN does not let atomic hydrogen entering in the atomic structure and therefore can significantly enhance the resistance of metals and alloys to hydrogen embrittlement. Nam et al. [70] reported that graphene coating could be a protective barrier against the hydrogen embrittlement. Li et al. [161], through the series of

electrochemical experiment, also reported the higher tendency of three dimensionally interconnected graphene reinforced Cu composite to block the penetration of atomic hydrogen.

2.6 Summary

In summary, graphene or hBN has a potential to improve the chemical, mechanical and thermal properties of metal matrix composites due to their outstanding properties. We found that there are several studies which discuss the properties of metal matrix composites reinforced by 3DiGr. However, a very limited amount of research has been done on the metal matrix composites reinforced by 3Di-hBN, despite the fact hBN has excellent mechanical, thermal, and chemical properties. Therefore, in this dissertation, we particularly explored the applications of hBN in CuNi matrix. We reported the mechanical, corrosive, high temperature oxidation, and thermal properties of 3Di-hBN reinforced CuNi composites fabricated by using a simple two-step process. Nevertheless, we also fabricated 3DiGr reinforced CuNi composite, and determined their scope to be used in the energy field.

3 EXPERIMENTAL

3.1 Research Objectives

In this dissertation, we aim to fabricate and characterize the three-dimensionally interconnected network of graphene or hBN reinforced CuNi composites via a simple two-step process. In a simple two-step process, a powder-based strategy is used to construct in-situ three-dimensional network of graphene (3DiGr) or hBN (3Di-hBN) by CVD process. The mechanism of formation of 3DiGr or 3Di-hBN will be discussed by analyzing various characterization techniques such as OM, Raman, TEM, and SEM. Furthermore, mechanical, thermal, and chemical properties will be investigated to analyze the effect of 3Di-hBN and 3DiGr. A flow chart shown in Figure 3.1 describes the overall objectives of the whole research process. The details of main reagents and devices which were used to synthesize 3Di-hBN CuNi and 3DiGr-CuNi composites are mentioned in Appendix "A". The rest of the chapter is devoted to providing the material selection, synthesis condition, and characterization of 3Di-hBN CuNi and 3DiGr CuNi composites.

3.2 Fabrication of 3Di-hBN CuNi Composite

3.2.1 Compaction of CuNi powders

In a simple two step process, the metallic powders are first compacted into a disc then CVD/MOCVD is perforemd. We purchased Cu and Ni particles having sizes of 14-25 μm and ∼1 μm, respectively from Sigma-Aldrich. These particles had spheroidal shape and were used after heat treating at 200°C for 2 h in reducing environment of hydrogen gas in order to eliminate any moisture or oxide contents. The XRD patterns shown in Figure 3.2 confirmed that the powders contained only crystalline Cu and Ni with no other chemical residuals. Cu powder (70 wt.%) and Ni powder (30 wt.%) were mixed in a mortar with care not to change the particle size distribution. Then, the mixture was compacted in a

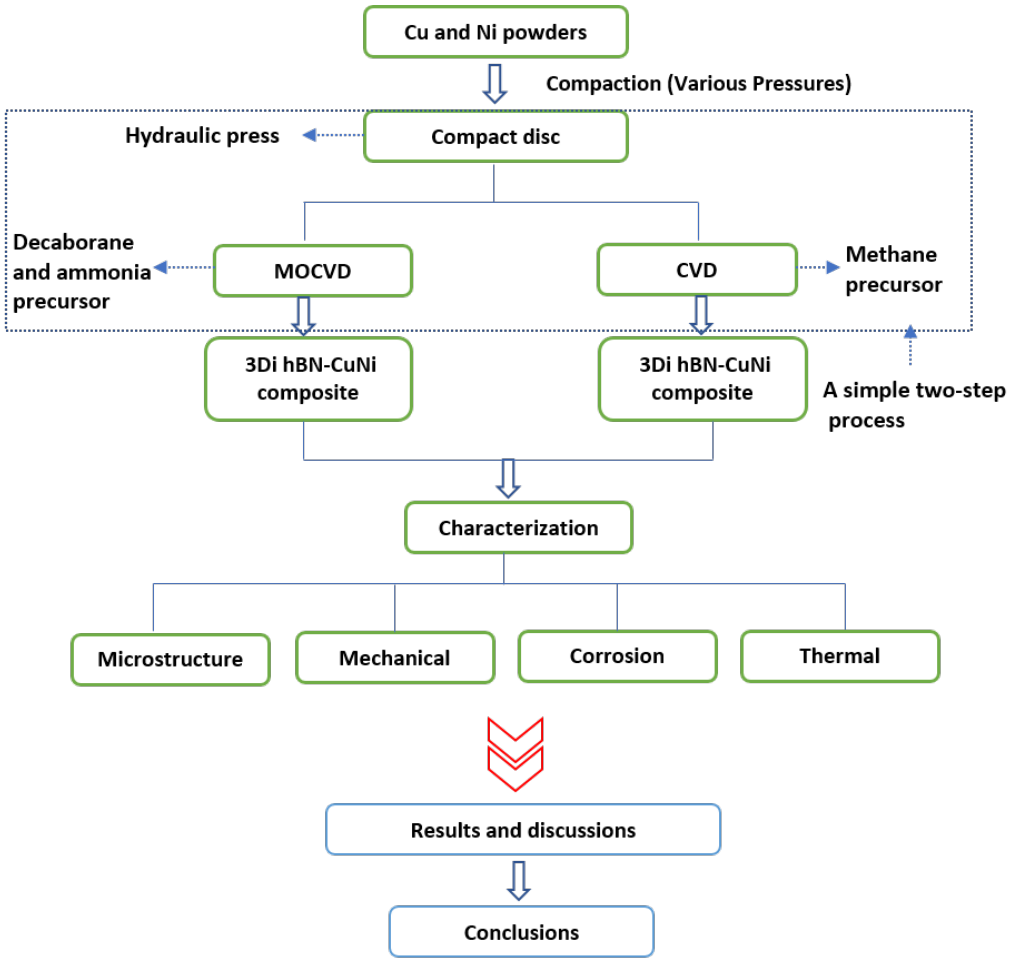

Figure 3.1: Flow chart illustrating the overall objectives.

mold using a double-action oil hydraulic press as shown in Figure 3.3 at the compaction pressures of 60, 110, 220, 280, 335, and 390 MPa. High compaction pressure on the spheroidal particles caused mechanical cold lock among the particles forming the disc shape with diameter of 15 mm or 20 mm (depending upon the mold size) and thichness of about 1.2 mm. Figure 3.4 shows the fractured surface of compacted disc where one can see the large Cu particles being deformed and producing mechanical interlock, while small Ni particles filling the gaps between the Cu particles.

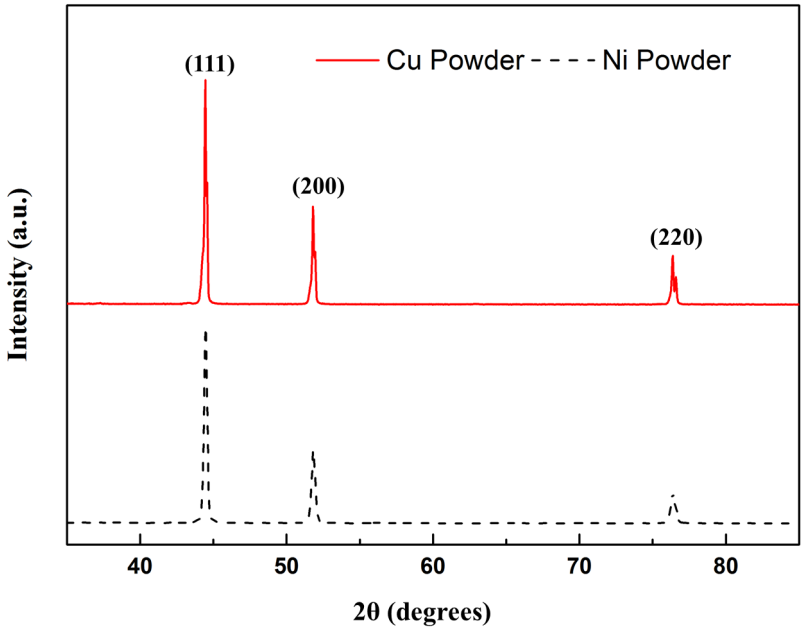

Figure 3.2: XRD patterns of Cu and Ni powders.

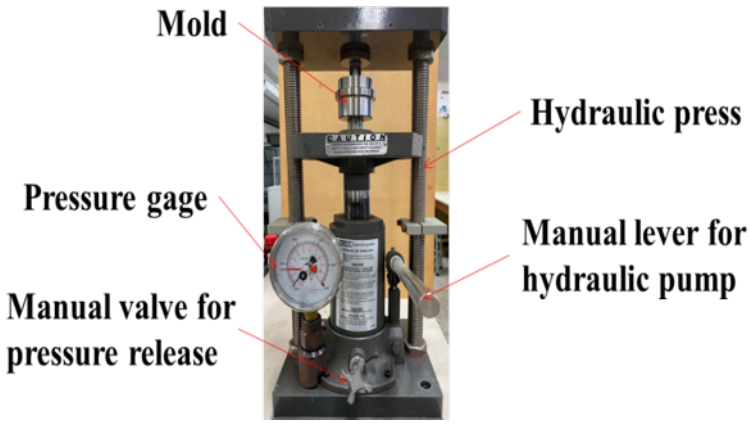

Figure 3.3: Mold and hydraulic press used for powder compaction.

Table 3.1: Chemical compositions of Cu and Ni powders.

Material	Purity	Trace metals in ppm
Cu	>99.5%	Fe 80.0, Na 9.42, Mn 7.6, Mg 4.69, Al 4.4, and B 1.98
Ni	>99.5%	Ag 1.3, Al 17.9, Ba 0.8 Ca 27.9, Cr 3.6, Cu 305.2, Fe 383.7 Mg 2.0, Mn 2.6, Na 11.1, Pd 8.0, Ti 144.5, and V 25.4

3.2.2 Metal Organic Chemical Vapor Deposition (MOCVD)

MOCVD was carried out in a Qartz glass tube furnace having a tube diameter of 23 mm and capable of reaching 1100°C. The system for the preparation of 3Di-hBN CuNi composites is schematically shown in Figure 3.5 (a). The compacted discs were placed in the furnace and MOCVD was performed under the conditions shown in Figure 3.6. At the beginning, air was removed from the system by purging with argon gas at least three times. Then the temperature was raised to 400°C in 24 min and held for 60 min to remove any oxides (deoxidation). The temperature was then increased to 1000°C in 36 minutes (16.67°C min^{-1}) and held constant for 15 or 30 min (sintering). The pressure during the deoxidation and sintering processes was kept at 330 Torr (Figure 3.6). Finally, MOCVD

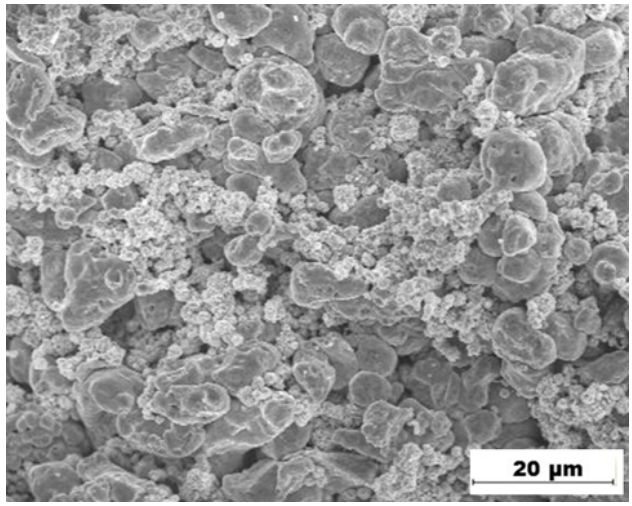

Figure 3.4: Cu and Ni particles shown at the fracture surface of the disc after compaction [162]. (Reused under a Creative Commons Attribution (CC BY) license. See Appendix 'E')

was performed using decaborane ($B_{10}H_{14}$) and ammonia (NH_3) as boron and nitrogen sources, respectively, for 15 min at a pressure of 450 Torr. Preferably, decaborane was used because it is easy to handle, commercially available, and stable. It is well suited to minimize the by-products at elevated temperature and increase the hBN yield [163]. Decaborane has a melting temperature of 98-100°C and its vapors were transported by carrier gas (argon) in the MOCVD growth zone, as shown in Figure 3.5 (a). The flow rate of carrier gas (argon) was kept at 1 sccm, while the flow rate of ammonia was 2 sccm. At elevated temperature (1000°C), decaborane and ammonia decomposed according to the following equations 3.1 and 3.2.

$$NH_{3(g)} \rightarrow [N] + \frac{3}{2}H_{2(g)} \tag{3.1}$$

$$B_{10}H_{14(g)} \rightarrow 10[B] + 7H_{2(g)} \tag{3.2}$$

Deoxidation, sintering and MOCVD were all carried out in reducing enevironment of hydrogen gas having flow rate of 10 sccm. The specifications of MOCVD system used for the fabrication of 3Di-hBN CuNi composites are given in Appendix ”B”. The 3Di-hBN CuNi composite fabricated using a simple two-step process is shown in Figure 3.5 (b).

3.3 Fabrication of 3DiGr-CuNi Composite

3.3.1 Compaction of CuNi Particles

The same procedure was followed as described in Section 3.2.1 for the compaction of Cu and Ni powders to synthesize 3DiGr CuNi composites.

3.3.2 Chemical Vapor Deposition (CVD)

Figure 3.7 shows the conditions for the preparation of 3DiGr CuNi composites. The compacted discs were put into a quartz tube furnace with a tube diameter of 80 mm

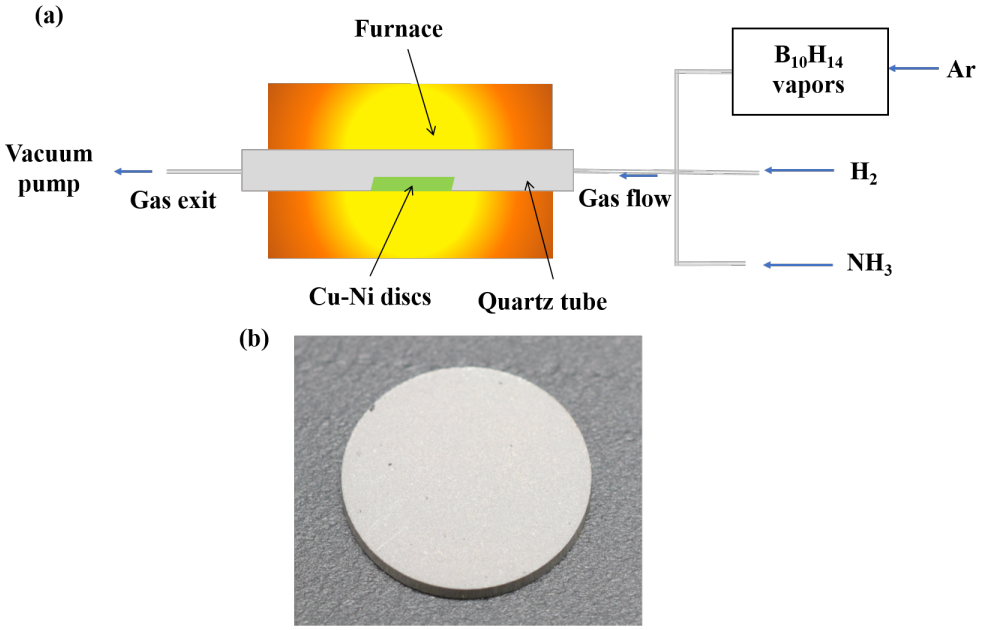

Figure 3.5: (a) Schematic illustration of the fabrication of 3Di-hBN CuNi composite and (b) disc-shaped 3Di-hBN CuNi composite fabricated using a simple two-step process [162]. (Reused under a Creative Commons Attribution (CC BY) license. See Appendix 'E')

capable of reachong 1100°C. The pressure inside the furnace is controlled by a throttle valve in conjunction with a pressure regulator. Before starting the CVD process, the system was purged with Ar gas at least three times to remove any air in the furnace tube. Then, the temperature of the system was increased to 400 °C at the rate of 16.67°C min^{-1} and then kept in a reducing hydrogen environment at 330 Torr for 60 min to remove any oxides (deoxidation). Then, the temperature was increased to 1000°C at the rate of 16.67°C min^{-1} and held for 30 min, before CH_4 was introduced into the system for 30 min with a mass flow rate of 5 sccm at 450 Torr. The system was then cooled to room temperature. Deoxidation, sintering and CVD were all carried out in reducing enevironment of hydrogen gas having flow rate of 10 sccm. The specifications of CVD system used for the fabrication of 3Di-hBN CuNi composites are given in Appendix "B". To compare the electrochemical corrosion resistance, thermal conductivity and

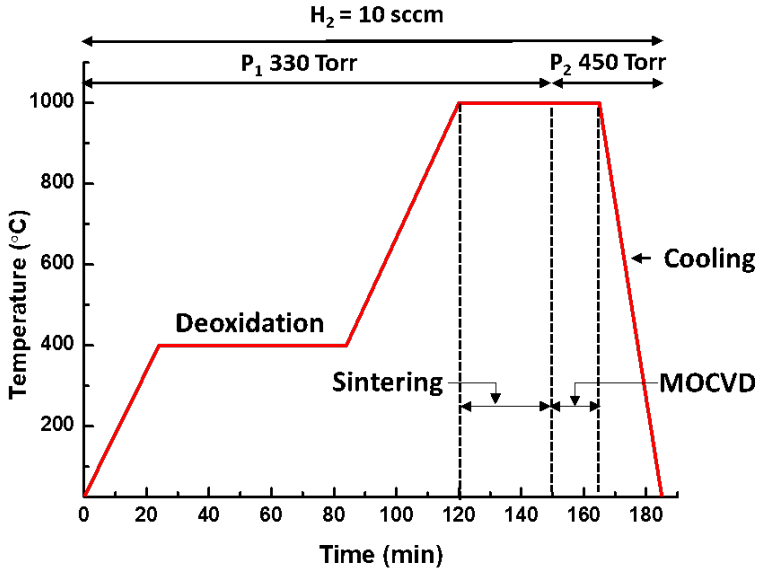

Figure 3.6: MOCVD conditions for fabrication 3Di-hBN CuNi composite [164]. (Reused with permission from Springer Nature under license number 5196180570802. See Appendix 'E')

mechanical properties, a powder metallurgy CuNi (PM CuNi) alloy was also fabricated under similar conditions except CVD, as schematically shown in Figure 3.8.

3.4 Characterization of Synthesized Composites

3.4.1 Density of Composite

Density measurements were made for at least three important reasons: (1) for the determination of mass and volume of samples, (2) the quality of the samples and (3) selecting the optimal experimental conditions. Sample density varies with powder size, compaction pressure, and experimental condition of CVD. The densities of synthesized 3Di-hBN CuNi composites were measured using Archimedes immersion technique. The samples were weighed in air and in distilled water, then the density was calculated

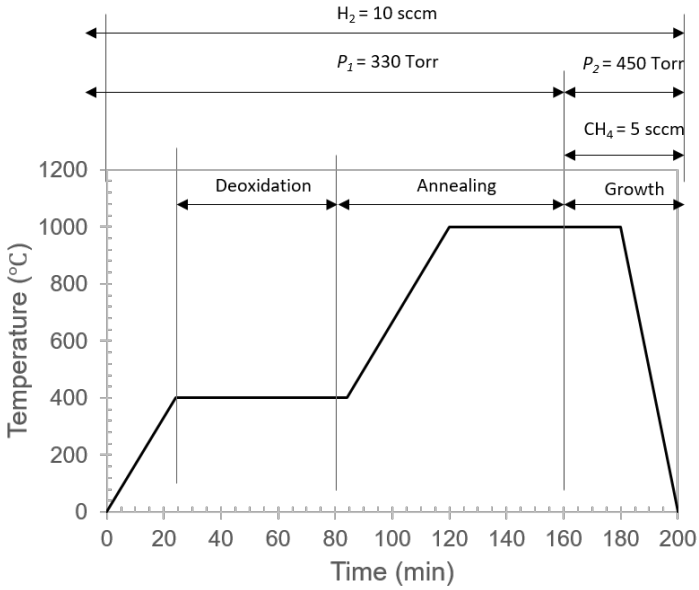

Figure 3.7: Experimental conditions for fabricating 3DiGr CuNi composites [28]. (Reused under a Creative Commons Attribution (CC BY) license. See Appendix 'E')

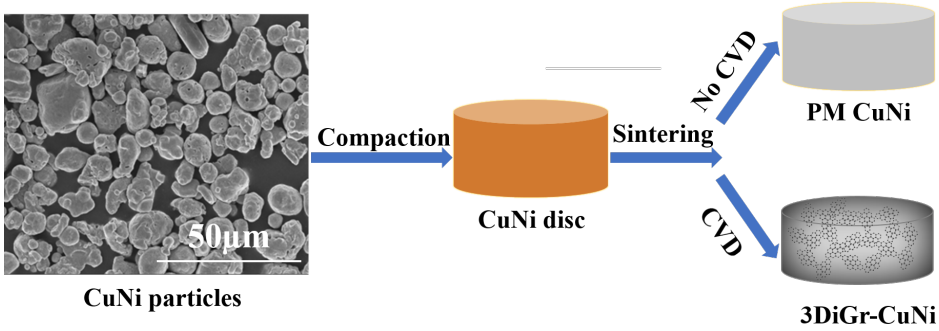

Figure 3.8: Schematic of fabrication of PM CuNi alloy and 3DiGr CuNi composite [161]. (Reproduced under a Creative Commons Attribution (CC BY) license. See Appendix 'E')

according to equation 3.3.

$$Density\ of\ composite\ = \frac{w_a}{w_a - w_w} \tag{3.3}$$

where w_a and w_w are the masses of the sample in air and water, respectively.

3.4.2 Microstructural Characterization

3.4.2.1 Optical Microscopy (OM)

In this research, OM was used to find the optimum CVD conditions for the synthesis of 3Di-hBN CuNi and 3DiGr CuNi composites. Microstructure of the composites prepared under various CVD conditions and compacting pressures was examined using OM in order to observe the relative pore density. OM investigations of samples were conducted after the sample was cut in half and the cutting surface was polished with emery papers of size down to 4000 grit. The sample preparation method for OM investigation is given in Appendix ”C”. The polished surface was etched at room temperature using a mixed solution of 0.5 M $FeCl_3$ and 2 M HCl to reveal the microstructure [43]. The procedure to make this etchant is also given in Appendix “C” in detail.

3.4.2.2 Scanning Electron Microscopy (SEM)

In scanning electron microscopy, the surface of sample is scanned in a raster pattern by the beam of high-enegy electrons. It has become a widely used tool for studying the surface morphology, microstructure and composition of various materials under vacuum. The structures of 3Di-hBN and 3DiGr were examined by scanning electron microscope. To extract 3Di-hBN or 3DiGr from the composites, 3Di-hBN CuNi (or 3DiGr CuNi) was placed in the etching solution of HCl and $FeCl_3$ for a sufficiently long time so that all the metallic content is etched away, leaving 3Di-hBN (or 3DiGr). After complete removal of the CuNi matrix, 3Di-hBN (or 3DiGr) was washed a few times with DI water and then freeze-dried to obtain a 3D structure [165]. The sample preparation for SEM and the freeze-drying method are described in detail in Appendix ”C”.

3.4.2.3 Transmission Electron Microscopy (TEM)

The TEM is a powerful technique to probe the nanostructed materials. The image

on TEM is mainly formed by the transmitted signals passing through a thin sample. The resolution of TEM extends to the atomic level due to the very small wavelength of the electrons. This property of TEM makes it possible to analyse a wide variety of materials in many fields, such as bioengineering and chemical engineering. For TEM measurements, the 3Di-hBN CuNi composites were mechanically polished to a thickness of 100 µm and cut into small pieces of 3 mm diameter (see Appendix "C"). Then the CuNi was etched out in the etching solution of HCl and $FeCl_3$, leaving only the 3Di-hBN foam, which after thorough cleaning was transferred to the TEM grid for examination.

3.4.2.4 X-ray Diffraction (XRD)

XRD measurements were performed on clean and flat wafers to investigate the crystal structure of PM CuNi alloy, 3DiGr CuNi, and 3DihBN CuNi composites. The working principle of X-ray diffraction can be understood as follows. When X-ray radiation with monochromatic wavelength falls on a sample, it interacts with the valance electrons, which cause the scattering of the incident electromagnetic wave. Since atoms in crystalline materials are arranged periodically in a lattice and the distance between planes is approximately same as the wavelength of the incident radiation, the scattered wave can interfere either constructively or destructively. Diffraction occurs when X-rays are emitted at characteristic angles based on the distance between atoms arranged in crystallographic planes. In general, crystals have a multiple set of planes having a specific interplanar distance. This unique interplanar distance gives rise to the characteristic angle of diffracted X-rays. The wavelength, atomic spacing and, angle are corelated according to Bragg's equation [166]. In the present report, qualitative and quantitative phase analyses of the composites was carried out by XRD technique using Cu Kα radiation with a wavelength of 1.54 Å and scan range of 20^o to 100^o.

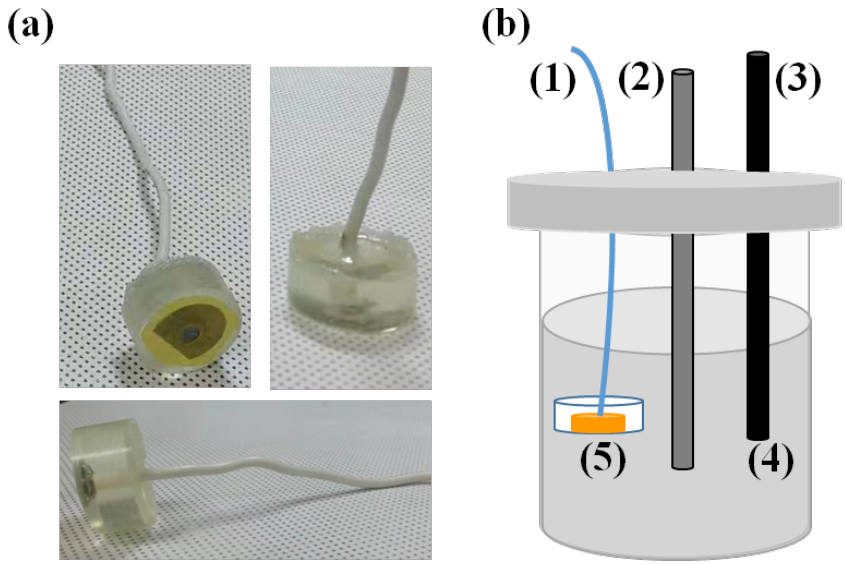

Figure 3.9: Schematic of potentiodynamic polarization test, (a) specimens to be tested (b) experimental set-up which is composed of (1) a working electrode, (2) a reference electrode, (3) a graphite counter electrode, (4) 3.5wt% NaCl solution, and (5) a specimen to be tested [161]. (Reproduced under a Creative Commons Attribution (CC BY) license. See Appendix 'E')

3.4.3 Electrochemical Corrosion Experiments

The electrochemical corrosion behaviorof 3Di-hBN CuNi, 3DiGrCuNi composites and PM CuNi alloy were analyzed by potentiodynamic polarization experiments in 3.5 wt% NaCl solution at 25°C using a potentiostat (Bio Logic VMP3) with a three-electrode electrochemical cell. The samples were prepared by attaching a copper wire on the rear side of the sample using a conductive epoxy resin, followed by mounting with an epoxy resin (Figure 3.9 (a)). The surface (to be investigated) was polished with emery paper having grit size up to 4000. The surface was then cleaned with DI water and sonicated to remove microparticles that had become lodged on the surface as a result of polishing. After sonication, the samples were dried with N_2 gas. A conventional three-electrode cell was set up with the sample, a saturated calomel electrode, and graphite as the working, reference, and counter electrodes, respectively, as shown in Figure 3.9 (b) . Only the

surface of 0.28 cm^2 of the sample was exposed, while the rest of the surface was covered with waterproof tape. Before starting the potentiodynamic polarization experiment, the electrolyte (NaCl solution) was degassed with nitrogen for at least 1 hour. The open circuit potential (OCP) was continuously monitored until steady state was reached. The potentiodynamic polarization measurements (cathodic and anodic) were performed with a voltage sweep rate of 1 mV s^{-1} in a scan range of -0.5 to $+0.5$ V. To determine the corrosion current density (I_{corr}), a Tafel analysis of the logarithm of current density (I) versus potential (V) was performed for both oxidation and reduction reactions. The prepared samples and schematic diagram of the experimental setup are shown in Figure 3.9.

In addition, electrochemical impedance spectroscopy (EIS) of 3Di-hBN CuNi composite and PM CuNi alloy was performed to further evaluate their corrosion behavior. The frequency was varied from 10 mHz to 0.1 MHz by applying a sinusoidal AC potential of 10 mV. Bode and Nyquist plots were constructed to understand the corrosion behavior. In Nyquist plot, imaginary impedance is plotted against the real impedance, while Bode plots contain frequency plotted against the magnitude of impedance (Z) and negative phase angle (θ) [167]. Lastly, the effect of corrosion on the microstructure was analyzed using SEM.

3.4.4 High-Temperature Oxidation

The stability of hBN at high temperatures prompted us to investigate the resistance of 3Di-hBN CuNi composite to high-temperature oxidation. For the high-temperature oxidation experiments, the disk samples with a diameter of $\sim$15 mm were cleaned with acetone and then dried in an oven. The samples were then weighed using an analytical balance with an accuracy of 0.01 mg. The weighed samples were placed on alumina crucibles and heated to 900°C in an electric muffle furnace. The temperature of 900°C was maintained for the duration of 12 h, 24 h, 36 h and 48 h. Upon cooling, the weight

of the samples was measured again to calculate the mass gain due to oxidation. The oxidation behavior at high temperatures was then analyzed by plotting the graph between the mass gain per unit area and the oxidation time. Moreover, the same experiment was performed for PM CuNi alloy for comparison. The effect of temperature on oxidation behavior was also analyzed using an OM.

3.4.5 Uniaxial Tensile Tests

The mechanical properties of 3Di-hBN CuNi, 3DiGr CuNi composites, and PM CuNi alloy were investigated by uniaxial tensile tests. The dogbone-shaped specimens with a gauge length of 4 mm and a cross section of about 2 mm $\times$ 1 mm were prepared from the discs (diameter 18.9 mm) by wire cutting (Figure 3.10 (a)), and the uniaxial tensile test was performed in a tensile testing machine (H10KS) with a cross-head spead of 0.09 mm min^{-1}. The stress-strain curves obtained from the uniaxial tensile tests were further analyzed to determine the yield strength, ultimate tensile strength (UTS), elongation at break, and fracture toughness. The tensile testing machine with the loaded tensile specimen is shown in Figure 3.10 (b). The yield strength was measured using the 0.2% offset method, while the fracture toughness was calculated by finding the area under the stress-strain curve, which gives the total energy absorbed before fracture [168]. Appendix ”D” describes in detail the method used to determine the mechanical properties.

3.4.6 Thermal Conductivity Measurement

Accurate measurements of density and thermal properties such as thermal diffusivity and specific heat capacity are required to accurately determine thermal conductivity [169]. Thermal conductivity (k) is given by the following equation 3.4 [169].

$$k = \alpha \times \rho \times c_p \tag{3.4}$$

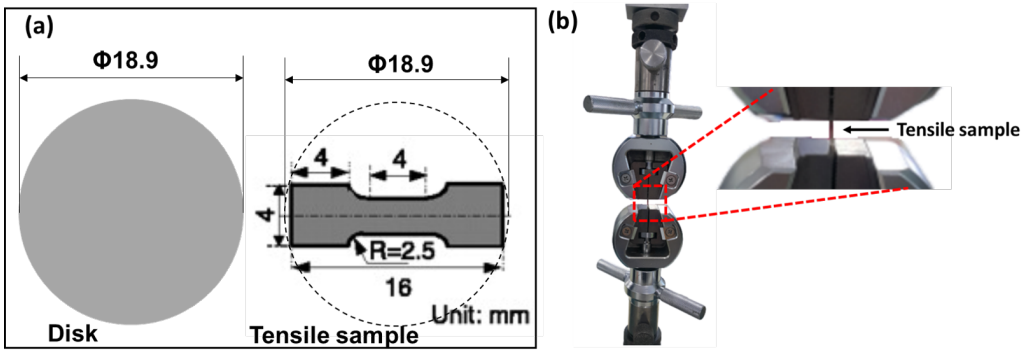

Figure 3.10: (a) Technical drawing of composite disc and the tensile sample prepared by wire cutting operation [164], (Reused with permission from Springer Nature under license number 5196180570802. See Appendix 'E'), (b) tensile sample loaded in tensile tester.

where α, ρ, and c_p are the thermal diffusivity, density, and specific heat capacity, respectively of the sample whose thermal conductivity is to be measured. In our experiment, the thermal diffusivity of the disk sample with a diameter of 12.7 mm and a thickness of 1 mm was measured with the instrument (NETZSCH LFA 447) according to the well-known method [170], in which the front side of the sample was heated with a laser source and the eventual temperature rise on the rear surface was recorded with an infrared detector according to Parker's law [170]. The resulting curve of temperature rise versus time was analyzed to determine the thermal diffusivity. Next, the density of the sample was measured using the Archimedes immersion technique as explained in Section 3.4.1. In addition, the specific heat capacity was determined by preparing rectangular samples of size 4 mm$\times$ 4 mm $\times$ 0.5 mm using differential scanning calorimetry (TA instrument DSC Q2000) technique. The measurement of c_p is described in detail in Appendix "D".

4 RESULTS AND DISCUSSIONS

This chapter will discuss the outcomes of the experiments which were carried out as described in previous chapter. The results were explained to highlight the influence of three dimensionally interconnected network of hBN or graphene on the properties of synthesized 3Di-hBN CuNi and 3DiGr CuNi composites.

4.1 Synthesis of 3Di-hBN CuNi composites

4.1.1 Mechanism of hBN Formation at Grain Boundaries

The processes involved in the synthesis of 3Di-hBN CuNi composite are schematically shown in Figure 4.1. Cu and Ni particles are compacted into a disc after carefully mixing as explained in Section 3.2.1. During sintering, the excess surface free energy of the particles acts as the driving force for the diffusion which leads to the reduction in volume and eventual formation of solid solution of Cu and Ni [171, 172]. As a result, the volume of the compact disc shrinks and thus densification occurs. We believe that the 3Di-hBN formed in 3Di-hBN CuNi composites in following stages [28]. (i) The diffusion of metal particles under the action of driving force due to reduction of surface energy (consolidation), (ii) the formation of solid solution of Cu-Ni due to diffusion of Cu to Ni or vice versa, (iii) durring MOCVD, the diffusion of boron and nitrogen in the solid solution of CuNi, and (iv) precipatation of boron and nitrogen atoms out from CuNi solid solution, nucleation and growth of 2D hBN layers along the interfaces of CuNi grains resulting in the formation of 3Di-hBN CuNi composite [173].

As the solid solution of Cu and Ni is formed, small pores or voids cab be formed, probably due to the insufficient sintering time or excessive free space among the particles. hBN can nucleate and grow in these pores because of the possibility of these pores acting as catalytic sites for the nucleation and growth during subsequent MOCVD process thus forming bulk hBN at these sites [162]. The small lighter gray areas (some of which are

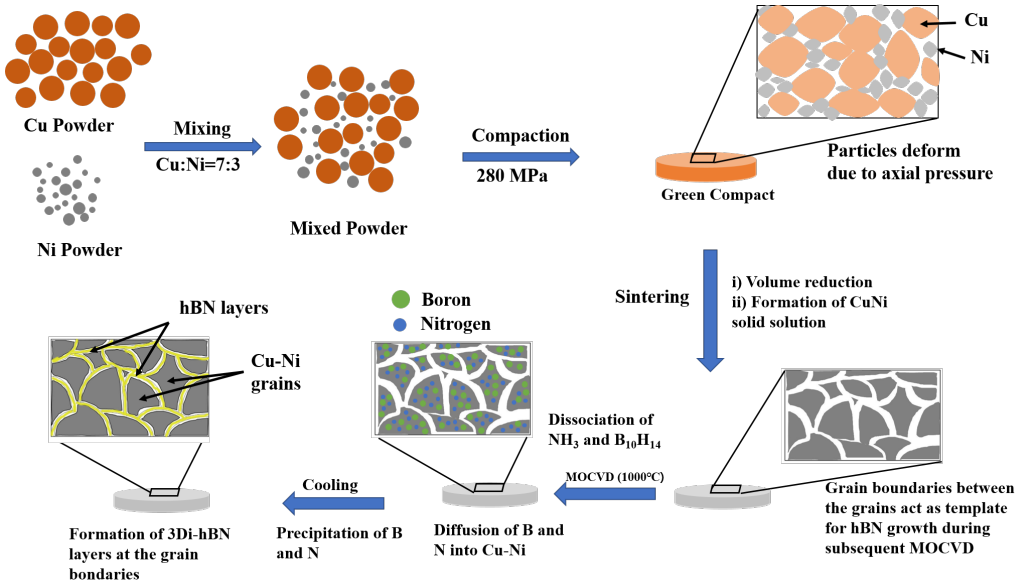

Figure 4.1: Schematic showing the process of formation of 3Di-hBN CuNi composite [162]. (Reused under a Creative Commons Attribution (CC BY) license. See Appendix 'E')

indicated by small white loops) in Figure 4.2 indicate the bulk hBN that accumulated on pores during the MOCVD process. Excessive formation of bulk hBN may result in poor properties of 3Di-hBN CuNi composites including mechanical, thermal and wear. Therefore, it is important to find the optimal conditions in order to minimize these pores (generated during sintering) and bulk hBN (formed during MOCVD).

4.1.2 Optimal Conditions for Forming 3Di-hBN

Figure 4.3 shows the density of 3Di-hBN CuNi composites as a function of compaction pressure (during compaction) and sintering time. The increase of the compaction pressure leads to an increase of the density up to a critical point (280 MPa), where the density of the composite starts decreasing. The increase in density with increasing compaction pressure is understandable because the particles have to travel a shorter distance during sintering when the compaction pressure is higher. Hence better

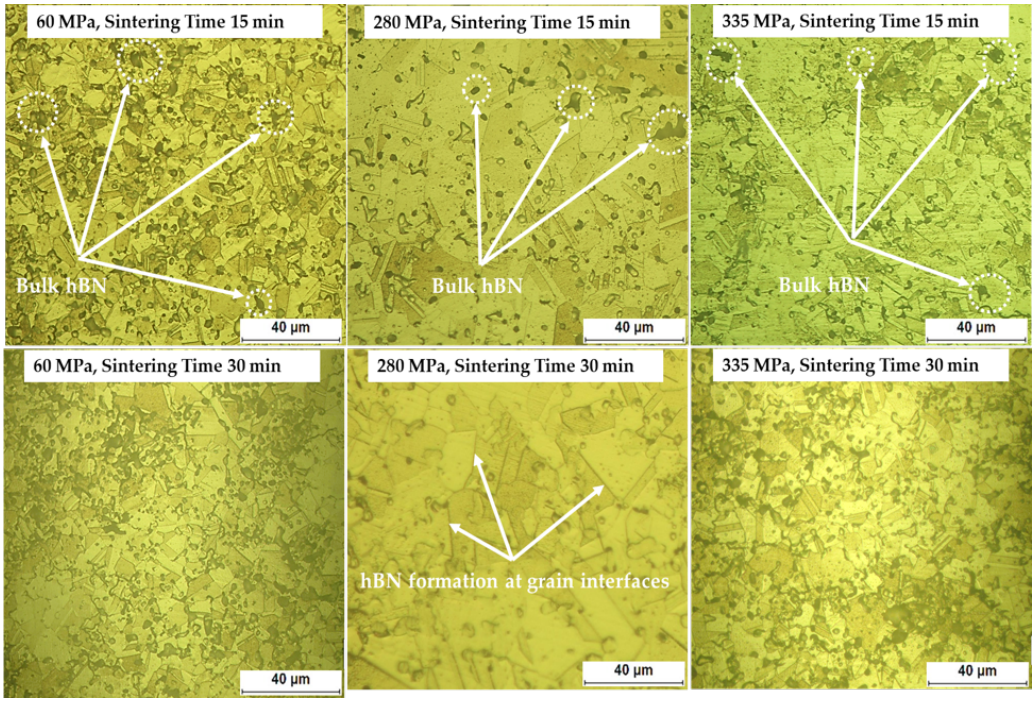

Figure 4.2: OM images of 3Di-hBN CuNi composites under various conditions [162]. (Reused under a Creative Commons Attribution (CC BY) license. See Appendix 'E')

densification is likely to occur. This trend is obvious in Figure 4.2, where the white dotted circles represent pores formed during sintering and filled with bulk hBN during MOCVD. Although these pores were filled with bulk hBN during MOCVD, the density of the composite did not increase as the densities of hBN ($\sim$2.1 gcm^{-3}) and CuNi alloy ($\sim$8.9 gcm^{-3}) differ significantly. A relatively small number of pores was observed with increasing compaction pressure as shown in Figure 4.2. However, the decrease in density with further increase in compaction pressure is due to the excessive friction between the particles. The particles at the top and bottom of the disk were compressed with greater force than the particles in the middle, so the particles in the middle have to travel a longer diffusion distance due to their lower density, resulting in the formation of larger pores or irregular shrinkages, as shown in Figure 4.4 (b). Moreover, the density of 3Di-hBN CuNi composite also depends on the sintering time, as shown in Figure 4.3. A longer sintering

time resulted in fewer pores (i.e., a lower volume fraction of bulk hBN), as can be seen in Figure 4.2, and consequently more densification.

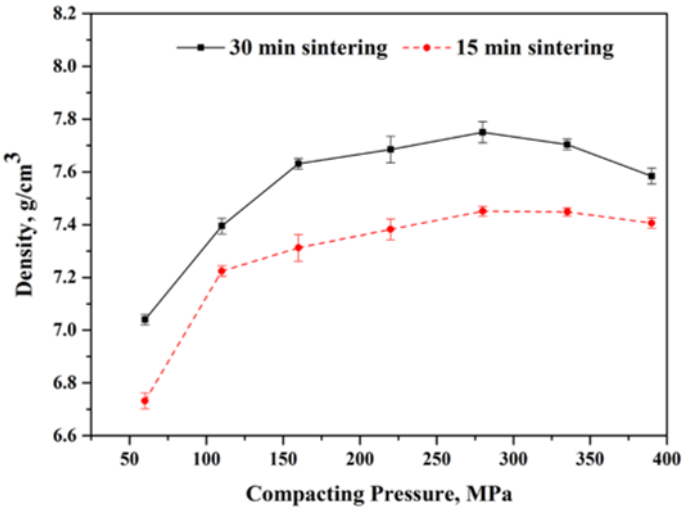

Figure 4.3: Density of the 3Di-hBN CuNi composite as a function of compacting pressure and sintering time [162]. (Reused under a Creative Commons Attribution (CC BY) license. See Appendix 'E')

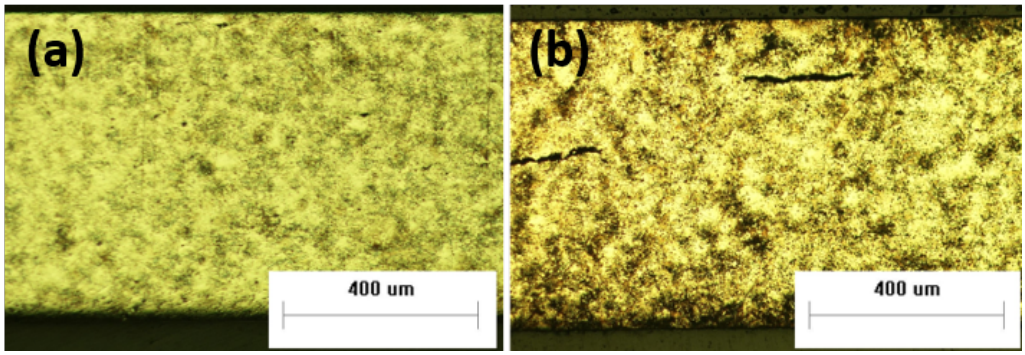

Figure 4.4: OM images of 3Di-hBN CuNi composites processed at compaction pressures of (a) 280 MPa and (b) 335 MPa [162]. (Reused under a Creative Commons Attribution (CC BY) license. See Appendix 'E')

4.1.3 Microstructural Investigation

The analyses of SEM and EDS results revealed that boron and nitrogen atoms were found in excess at the grain boundaries as discussed in our published work [162]. Moreover, the pores created during sintering were later filled with bulk hBN during the MOCVD process as we have reported in Ref. [162] that these pores also serve as catalytic sites for the nucleation and growth of hBN. Figure 4.5 (a) shows the SEM image of 3Di-hBN CuNi composite and Figure 4.5 (b) indicates the presence of boron and nitrogen atoms at the grain boundaries of CuNi matrix (inset of Figure 4.5 (a)).

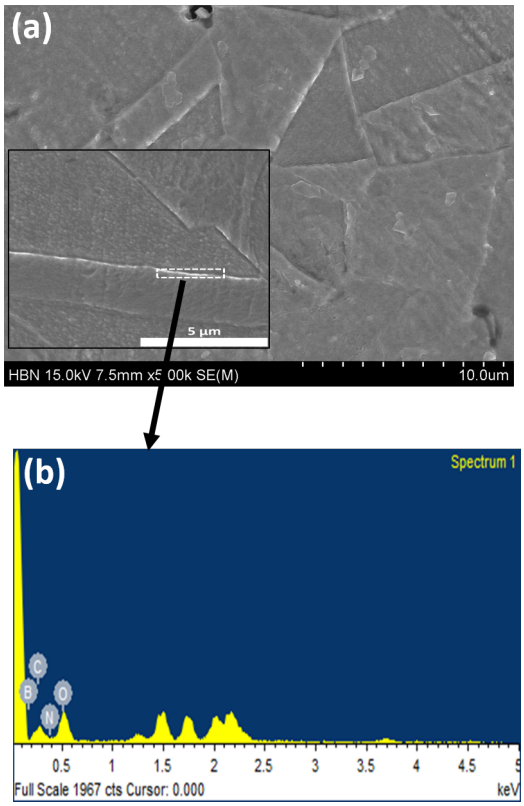

Figure 4.5: (a) SEM image showing the grains of 3Di-hBN CuNi composite produced under compaction pressure of 280 MPa and sintering time of 30 min (b) EDX result at grain boundary of grains of 3Di-hBN CuNi (inset of Figure 4.5 (a)).

Figure 4.6 shows the SEM image of the 3Di-hBN foam obtained after etching the 3Di-hBN-CuNi composite. It can be seen that the hBN layers form an interconnected network, which has a foam-like structure with channels and pockets. The metallic particles in the 3Di hBN-Cu-Ni composite are mostly in direct contact with each other. When the composite is placed in an etchant, these metallic particles etch out and form channels, as shown in Figure 4.6, completely removing the CuNi matrix from the 3Di hBN-Cu-Ni composite and leaving 3Di-hBN behind. The pockets (Figure 4.6) are formed when the CuNi grains are etched away while the surrounding hBN layers are retained. The average size of the pockets is 10-20 µm, which is consistent with the average grain size of 3Di-hBN CuNi composite (Figure 4.2), implying that hBN layers form around the CuNi grains.

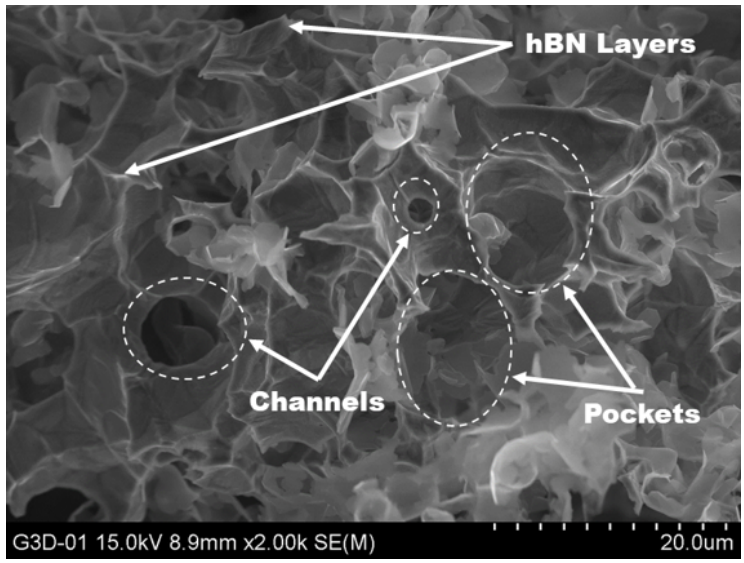

Figure 4.6: SEM image showing the 3D interconnected network of hBN in 3Di-hBN CuNi composite produced under compaction pressure of 280 MPa and sintering time of 30 min, respectively [162]. (Reused under a Creative Commons Attribution (CC BY) license. See Appendix 'E')

The crystallinity of 3Di-hBN CuNi composite was confirmed by XRD analysis, as can be clearly seen from the sharpness of the different diffraction peaks (Figure 4.7

(a)). The XRD pattern shows that a face-centered cubic solid solution of Cu-Ni was formed and no other diffraction peaks were observed than the characteristic planes shown in Figure 4.7 (a) (JCPDS 04-0836). Moreover, Figure 4.7 (b) shows the elemental distribution map of 3Di-hBN CuNi composite. Cu and Ni are uniformly distributed along the surface (100 µm × 100 µm), implying the formation of a CuNi solid solution.

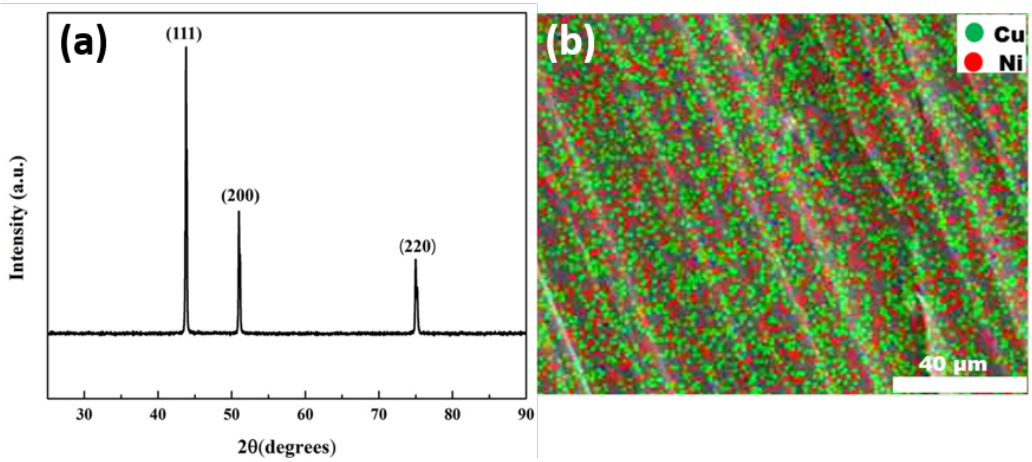

Figure 4.7: (a) XRD pattern of 3Di-hBN CuNi composite and (b) Elemental distribution map of 3Di-hBN CuNi composite [162]. (Reused under a Creative Commons Attribution (CC BY) license. See Appendix 'E')

TEM inspection of 3Di-hBN was also performed, as shown in Figure 4.8. The low magnification bright field TEM in Figure 4.8 (a) shows a complex morphology with curvatures and overlapping structures in which the 3D layers of hBN form a porous structure (see Figure 4.8). The structure collapsed under the action of capillary force during drying when 3Di-hBN was transferred on TEM grid. The high-resolution TEM image (Figure 4.8 (b)) shows 2-6 hBN layers with an interlayer spacing of about 0.35 ± 0.02 nm (inset in Figure 4.8 (b)). The interlayer spacing of ∼0.35 nm implies the thickness of one layer of hBN which is consistent with theoretically predicted value [139, 174, 175]. Figure 4.8 (c) shows the lattice pattern of 2D hBN transferred on TEM grid. The inset in Figure 4.8 (c) shows the lattice profile of hBN, indicating the lattice

parameter of 0.24 nm which is consistent with the theoretical value [176]. Moreover, EDX analysis shown in Figure 4.8 (d) reveals the presence of B and N atoms, indicating the chemical composition of hBN.

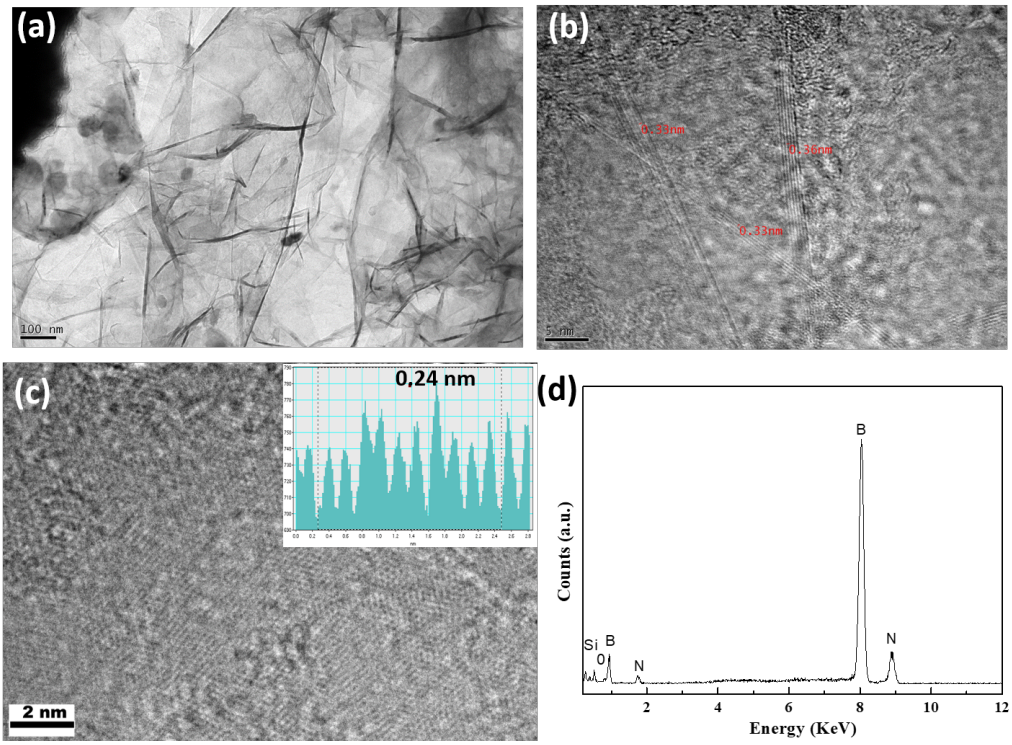

Figure 4.8: TEM investigation: (a) low-magnification bright-field TEM image of 3Di-hBN, (b) HR-TEM image showing 2–6 layers of hBN (inset shows a interlayer distance of 0.35 nm, (c) lattice pattern of 2D hBN(inset showing the lattice profile) and (d) EDS analysis of hBN [162]. (Reproduced under a Creative Commons Attribution (CC BY) license. See Appendix 'E')

In summary, 3Di-hBN CuNi composites were prepared by a simple two-step process. The maximum density of the composite was measured when the Cu and Ni particles were compacted with a compaction pressure of 280 MPa, and the sintering time was kept 30 min. Various characterization techniques such as OM, SEM and TEM showed that these conditions were optimal for forming three dimensionally interconnected network of hBN layers in 3Di-hBN CuNi composite.

4.2 Properties of 3Di-hBN CuNi composites

4.2.1 Mechanical Properties

The densities of 3Di-hBN CuNi composites as a function of compaction pressure are given in Table 4.1. The relative densities of 3Di-hBN CuNi composites can be calculated by comparing their densities with the density of PM CuNi alloy (7.9 g cm^3). As discussed earlier in Section 4.1.3 that the pores generated during sintering were filled later with bulk hBN during MOCVD and that no other microstructural defects were present in 3Di-hBN CuNi composites. This information leads to approximating the amount of hBN present in 3Di-hBN CuNi composites as given in following equation (4.1).

$$hBN\ content\ (wt.\%) = Density\ of\ hBN \times (1 - Relative\ density) \tag{4.1}$$

The density of hBN is ∼2.1 g cm^{-3} and therefore, amount of hBN for sample D was calculated to be 3.9 wt%.

Table 4.1: Actual and relative densities of 3Di-hBN CuNi composite and PM CuNi alloy.

Material	Sample Name	Compaction Pressure (MPa)	Actual Density (g cm^{-3})	Relative Density (%)
3Di-hBN CuNi composite	A	55	6.72	85.06
	B	210	7.21	91.26
	C	250	7.32	92.66
	D	280	7.75	98.10

The stress-strain curves for 3Di-hBN CuNi composites and PM CuNi alloy are shown in Figure 4.9. The inset in Figure 4.9 shows the macro image of the tensile sample. The increase in the density of 3Di-hBN leads to a significant increase in the yield strength, UTS, and ductility. When the density of 3Di-hBN CuNi composite was at its highest (sample D), the composite exhibited a yield strength, UTS, and fracture toughness of 252 ± 8 MPa, 340 ± 9 MPa, and 96 ± 6 MPa, respectively. In contrast, the lowest density sample (Sample A) exhibited a yield strength, UTS, and fracture toughness of 136 ± 12 MPa, 172 ± 9 MPa, and 11 ± 3 MPa, respectively. It was assumed that the excessive

amount of bulk hBN in the low-density samples would affect the mechanical performance of the composites. In contrast, 3Di-hBN CuNi composite with maximum density (∼7.75 g cm^{-3}) was assumed to have a well-established interconnected hBN network with good interfacial bonding to the metal matrix grains.

In addition, the mechanical properties of 3Di-hBN CuNi composite (sample D) were compared with those of PM CuNi alloy (7.9 g cm^{-3}), as shown in Table 4.2. In Figure 4.9, sample E shows the stress-strain curve of PM CuNi alloy. Encouragingly, 3Di-hBN CuNi composite showed yield strength, UTS, fracture toughness and elongation of 3Di-hBN CuNi composite, ∼16.3%, ∼11.67%, ∼27.9% and 20.1% higher than those of PM CuNi alloy, respectively, mainly due to the unique three-dimensional architecture of hBN.

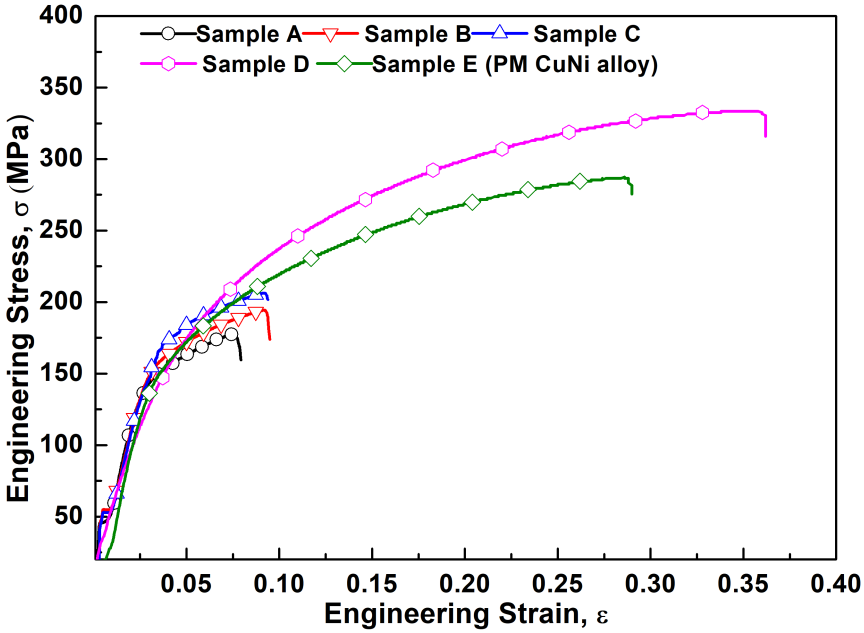

Figure 4.9: Stress-strain curves of 3Di-hBN CuNi composites and PM CuNi alloy [164]. (Reused with permission from Springer Nature under license number 5196180570802. See Appendix 'E')

Table 4.2: Mechanical properties of 3Di-hBN CuNi composite and PM CuNi alloy having densities of 7.75 g cm^{-3} and 7.9 g cm^{-3}, respectively.

Materia	Yield Strength (MPa)	Elastic Modulus (MPa)	UTS (MPa)	Elongation (%)	Toughness (MPa)
PM CuNi	211 ± 7	6083 ± 28	300 ± 7	28.9 ± 0.9	70 ± 5
3Di-hBN CuNi	252 ± 7	7872 ± 32	340 ± 9	36.2 ± 1.4	97 ± 6

High and low magnification SEM images of the fractured surfaces of the tensile specimens are shown in Figure 4.10. In these images, the typical ductile fracture for both 3Di-hBN CuNi composite (Figures 4.10 (a-b)) and PM CuNi alloy (Figure 4.10 (c)) can be discerened. The fractured surfaces clearly show the pronounced dimples. The nucleation of dimples occurs when the bond between the reinforcement and the matrix breaks during deformation [177]. In ductile fracture, nucleation, growth, and coalescence of dimples occur to form microcracks. The arrows in Figure 4.10 (a) indicate the hBN accumulated on the surface after fracture. Next, Figures 4.10 (b) and (d) show the presence of hBN detected by EDX analysis on the surface of the dimples. The continuous network of hBN blocks the propagation of cracks, thereby enhancing material's strength.

In addition to blocking dislocation movement and crack propagation, the hBN network also retards fracture by absorbing any externally applied load, giving the composite a toughening effect. This leads to improved ductility [7, 21, 29, 177]. In addition, the higher elastic modulus of hBN likely improves the toughness of the composite, leading to an increase in ductility while making fracture more difficult [29]. More ductile materials exhibit greater dimples and hence the dimple size is proportional to the ductility [177]. In Figure 4.9, the stress-strain curves show improved ductility of the material. This means that the CuNi matrix and the hBN bond are strong enough to prevent premature cracking at the interface.

Researchers have observed an increase in the mechanical performance of the metal matrix when boron nitride is incorporated [178–180]. This enhanced 3Di-hBN CuNi composite strength (Figure 4.11 (a)) can be explained with three possible mechanisms:

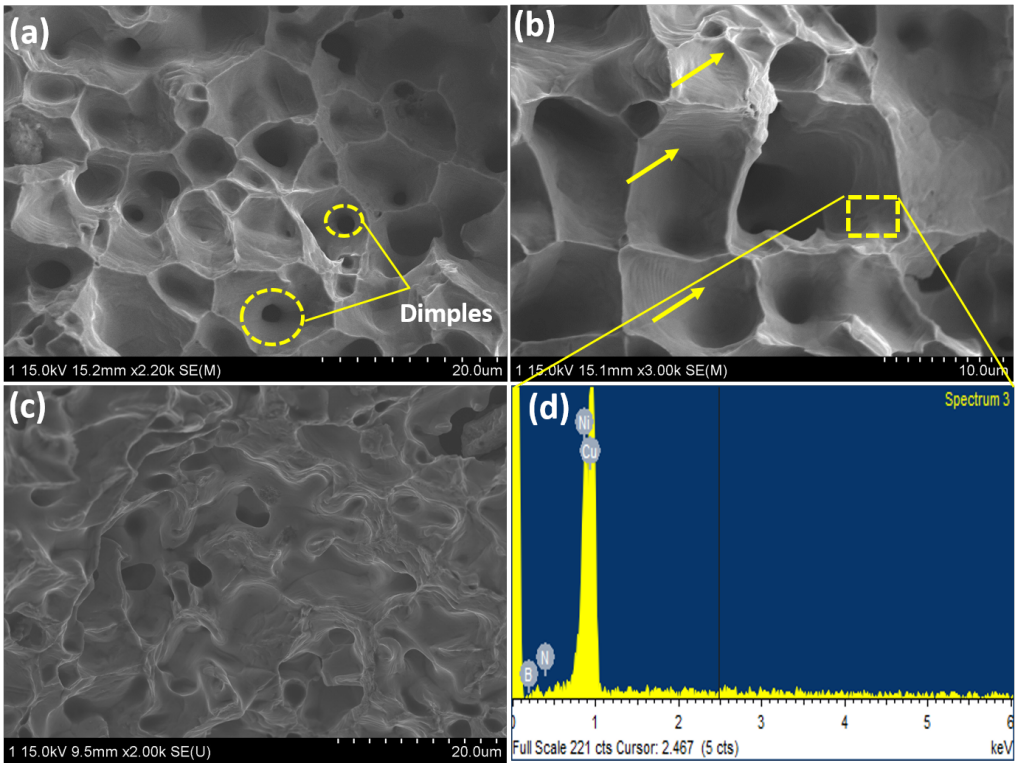

Figure 4.10: (a) SEM micrograph of 3Di-hBN showing the interconnected hBN (b-c) TEM images showing hBN layers of 3Di hBN [164]. (Reused with permission from Springer Nature under license number 5196180570802. See Appendix 'E')

load transfer, dislocation strengthening, and grain refinement [181].

A high load transfer efficiency is guaranteed by strong interfacial bonding of the reinforcing agent to the metal matrix. When attached with metal grains, hBN enhances the load-transfer efficiency since it possess a large specific area and high aspect ratio [29]. It was reported by Rui et al. that hBN strongly attaches to the metal matrix owing to its good wettability at atomic level [139]. The in-situ grown hBN accomplished by a simple two-step process is fairly thin as shown in 4.11 (b) and (c) as the solubility of B and N in CuNi is very low [138, 182]. It therefore develops a well-contacted interface with the CuNi matrix. The architecture of 3Di-hBN is responsible for its better reinforcing

efficiency in 3Di-hBN CuNi composite. 3Di-hBN can sustain the load as a whole unit instead of isolated layers (load transfer) [29].

In Figure 4.12 (a) the XRD patterns are shown and indicate broadened peaks of deformed 3Di-hBN CuNi composite compared to PM CuNi alloy. Using the Williamson-Hall technique [183], the dislocation density (ρ) vis-à-vis dislocations per unit area can be quantified through XRD analyses of the deformed samples. The dislocation density

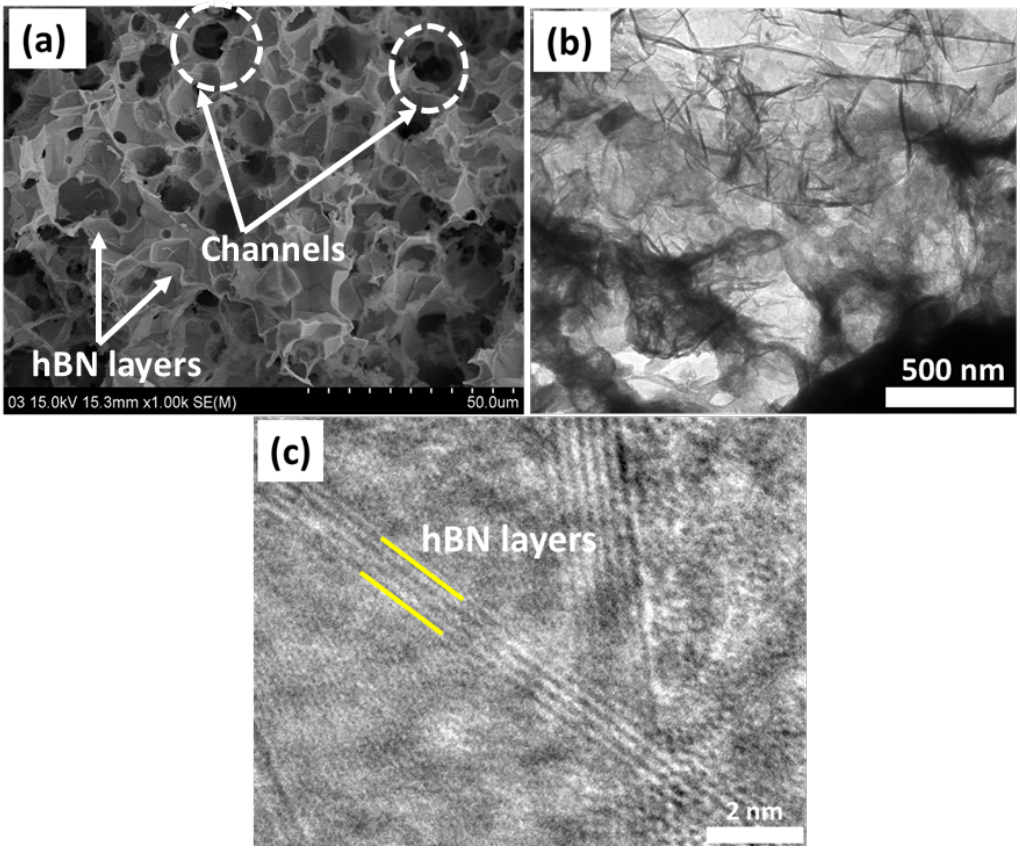

Figure 4.11: SEM micrographs form the fracture surfaces of (a-b) 3Di-hBN CuNi composite, (c) PM CuNi alloy, and (e) EDX spectrum of rectangular section in (b) [164]. (Reused with permission from Springer Nature under license number 5196180570802. See Appendix 'E')

calculated is given in the following equation:

$$\rho = \frac{2\sqrt{3}\varepsilon}{db} \tag{4.2}$$

where ε, d and, b are lattice strain, crystallite size and, burgers vector (0.254 nm for CuNi), respectively. ε and d can be calculated from XRD patterns and are related by following equation (4.3) based on Williamson-Hall method [184].

$$B cos\theta = \frac{K\lambda}{d} + 4\varepsilon sin\theta \tag{4.3}$$

where B is XRD peak broadening of full-width at half maximum (FWHM) in radians, K is shape factor and is constant (0.9), λ is wavelength of Cu Kα radiation (0.154 nm), and θ is the Bragg's angle. ε and d were found by linear-fitting of the plot between $Bcos\theta$ and $4sin\theta$ as shown in Figures 4.12 (b). These values were then populated in equation (4.2) to give the dislocation densities of 3Di-hBN CuNi composite and PM CuNi alloy.

The dislocation density of the deformed 3Di-hBN CuNi composite was 50.2% higher than that of PM CuNi alloy (Figure 4.12 (d)). This explains the dislocation strengthening mechanism in 3Di-hBN CuNi composite. At the CuNi grain boundary, hBN caused an accumulation of dislocations resulting in a relatively larger dissipation of applied energy applied which delayed the fracture [148]. The dislocation densities calculated for the undeformed specimens of 3Di-hBN CuNi composite and PM CuNi alloy are shown in Figure 4.12 (d). It can be seen that the undeformed 3Di-hBN CuNi composite has a higher dislocation density compared to the undeformed PM CuNi alloy. This can be attributed to the lattice mismatch between hBN and CuNi substrate. Due to this lattice mismatch, thermal stresses come into play and lead to the formation of more dislocations in 3Di-hBN CuNi composite.

Lastly, a relatively more grain refinement in the structure of 3Di-hBN CuNi composite is achieved by the formation of hBN layers at the CuNi matrix interfaces,

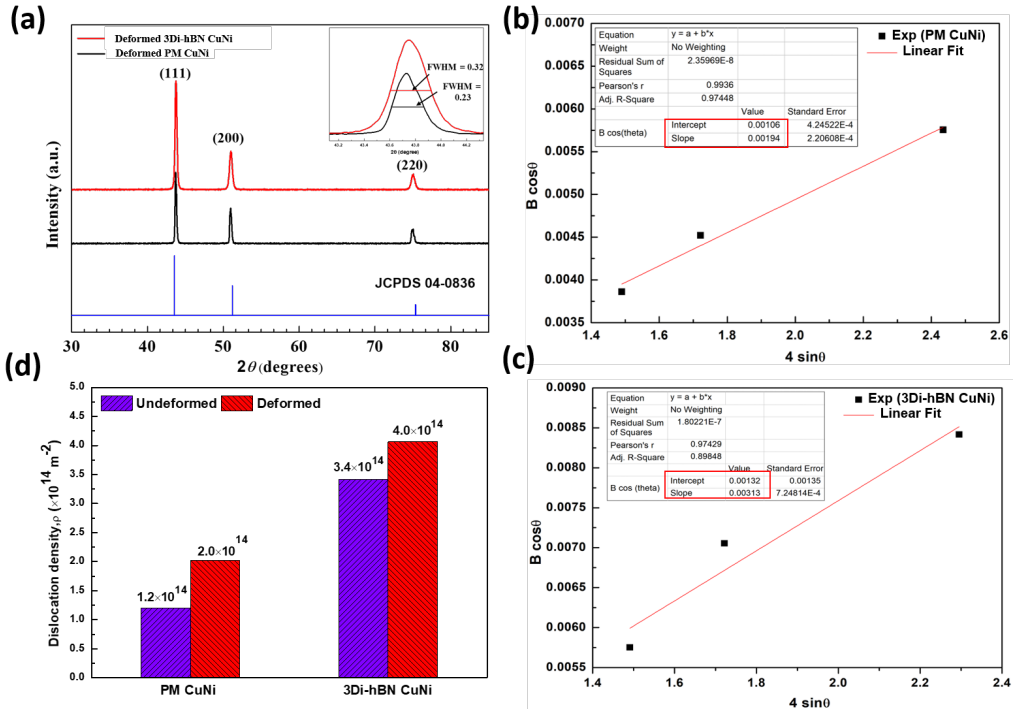

Figure 4.12: (a) XRD patterns of deformed 3Di-hBN CuNi and PM CuNi samples, Lattice strain and crystallite size calculation of (b) deformed PM CuNi and (c) deformed 3Di-hBN CuNi, and (d) Dislocation densities of deformed PM CuNi and 3Di-hBN CuNi composite [164]. (Reused with permission from Springer Nature under license number 5196180570802. See Appendix 'E')

which inhibits the grain growth (diffusion) during the MOCVD process [139]. A greater refinement is indicated in the structure of 3Di-hBN CuNi composite by OM images and XRD patterns compared with PM CuNi alloy (Figure 4.13). The smaller the grains, the larger the stress required for material's deformation. As a result, 3Di-hBN CuNi composite exhibits improved strength according to the Hall patch relationship [149].

4.2.2 Thermal Conductivity Analysis

Kostecki et al. [185] reported that the in-plane thermal conductivity of 2D hBN is as high as 400 W $m^{-1}K^{-1}$, which is higher than that of bulk crystalline hBN. Although the thermal conductivity of hBN is much lower than that of graphene (4000 W $m^{-1}K^{-1}$)

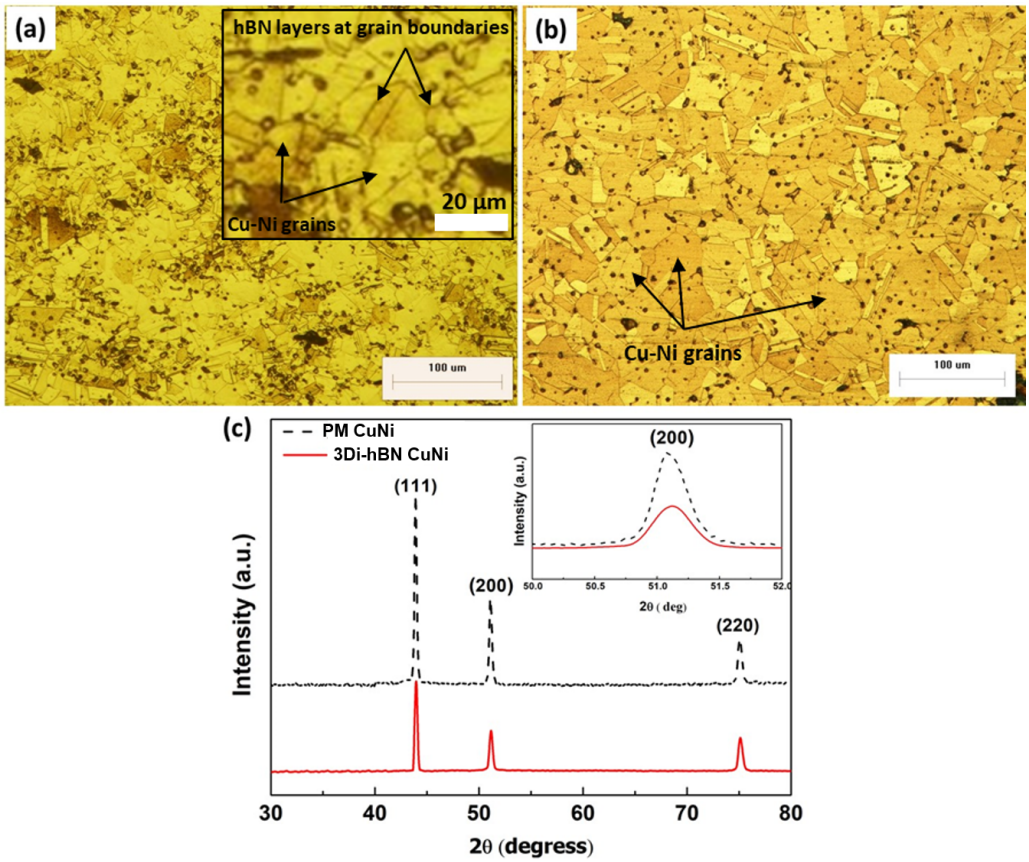

Figure 4.13: OM micrographs showing the microstructures of (a) 3Di-hBN CuNi composite and (b) PM CuNi alloy, and (c) XRD patterns of 3Di-hBN CuNi composite and PM CuNi alloy [164]. (Reused with permission from Springer Nature under license number 5196180570802. See Appendix 'E')

[186], the formation of hBN around the grains should somewhat improve the thermal conductivity of the composite. Moreover, the reinforcement by hBN is beneficial in certain applications where high thermal conductivity and low electrical conductivity are required, because hBN is an electrically insulating material [5, 187, 188]. The thermal conductivities of 3Di-hBN CuNi composite (18 ± 0.5 W $m^{-1}K^{-1}$) and PM CuNi alloy (16 ± 0.5 W $m^{-1}K^{-1}$) are shown in Figure 4.14. It was found that the thermal conductivity of 3Di-hBN CuNi composite (with a density of 7.75 g cm^{-3}) was ~10%

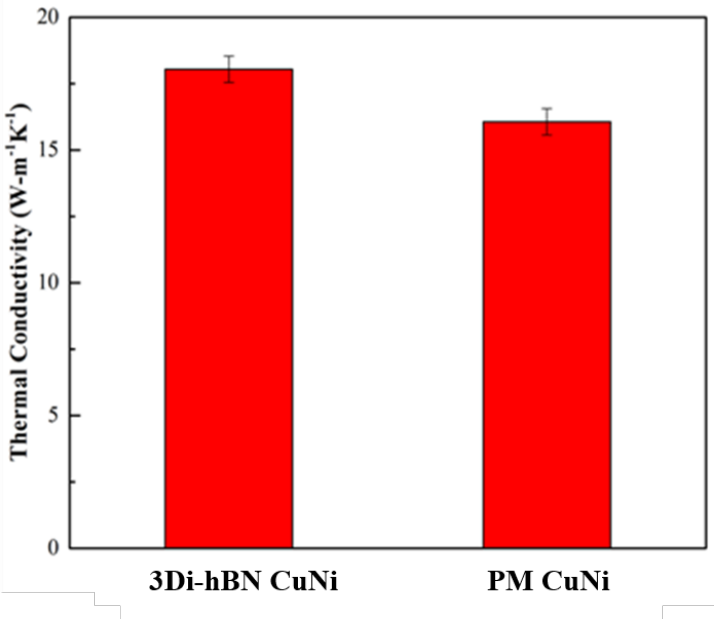

Figure 4.14: Thermal conductivities of 3Di-hBN CuNi composite and PM CuNi alloy at room temperature.

higher than that of PM CuNi alloy. This improvement could be due to the good alignment of the 3Di-hBN as well as its good bonding to the matrix, which provides a thermal conduction path along the in-plane direction [169, 185].

4.2.3 Electrochemical Corrosion Behavior

The potentiodynamic polarization curves of 3Di-hBN CuNi composite and PM CuNi alloy are shown in Figure 4.15 (a). The intersection of the cathodic and anodic polarization curves gives the corrosion current density (I_{corr}) and the corrosion potential (V_{corr}). 3Di-hBN CuNi composite exhibited better corrosion resistance than PM CuNi alloy. The corrosion potential of 3Di-hBN CuNi composite (−182.59 mV) was shifted in a more positive (upward) direction than that of PM CuNi alloy (−373.72 mV), as shown by the polarization curves of 3Di-hBN CuNi composite and PM CuNi alloy in Figure 4.15 (a). It was also found that the I_{corr} of 3Di-hBN CuNi composite (14.0 μA cm^{-2}) was

about 6 times lower than that of PM CuNi alloy (85.1 μA cm^{-2}). The lower value of I_{corr} also indicates that the corrosion resistance of 3Di-hBN is significantly improved. The improvement in electrochemical corrosion resistance can be attributed to the formation of an interconnected network of hBN layers anchored around the grains of the CuNi matrix, as shown by the EDS analysis (Figures 4.5 (a-b)) of 3Di-hBN CuNi composite. The interconnected network of hBN layers in 3Di-hBN CuNi composite, as shown in Figure 4.15 (b) resists the chrage transfer due to the impermeability of hBN to ions and molecules [160]. Therefore, the corrosion reaction speed is reduced because fewer ions flow across the metal-electrolyte interface as the exposed metal surface is reduced by hBN, as schematically shown in Figure 4.16. Consequently, the addition of a 3D interconnected network of hBN could effectively reduce the corrosion rate of the metal matrix in 3Di-hBN CuNi composites [160, 189–191].

Following equation (4.4) can be used to calculate the corrosion rate (CR) as per ASTM standard G102.

$$CR = K\left[\frac{I_{corr}}{\rho}\right] \times (EW) \tag{4.4}$$

where K is a constant and is equal to 3.27 $\times 10^{-3}$ mm g $\mu A^{-1} cm^{-1} year^{-1}$, EW is the equivalent weight of CuNi solid solution and is equal to 31.05, ρ is the density of the material (7.75 g cm^{-3} for 3Di-hBN CuNi composite and 7.9 g cm^{-3} for PM CuNi alloy). The values of CR for PM CuNi alloy and 3Di-hBN CuNi composite were calculated to be 1.09 mm $year^{-1}$ and 0.183 mm $year^{-1}$, respectively, using the equation 4.4. This clearly means that CR was significantly reduced by 3Di-hBN at the grain boundaries of 3Di-hBN CuNi composite; the value was reduced by ∼16.67%, indicating more than six times better corrosion resistance. Table 4.3 lists the electrochemical corrosion parameters of PM CuNi alloy and 3Di-hBN CuNi composite.

The SEM images of the surfaces of 3Di-hBN CuNi composites and PM CuNi alloy after performing electrochemical corrosion experiments are shown in Figures 4.17 (a)

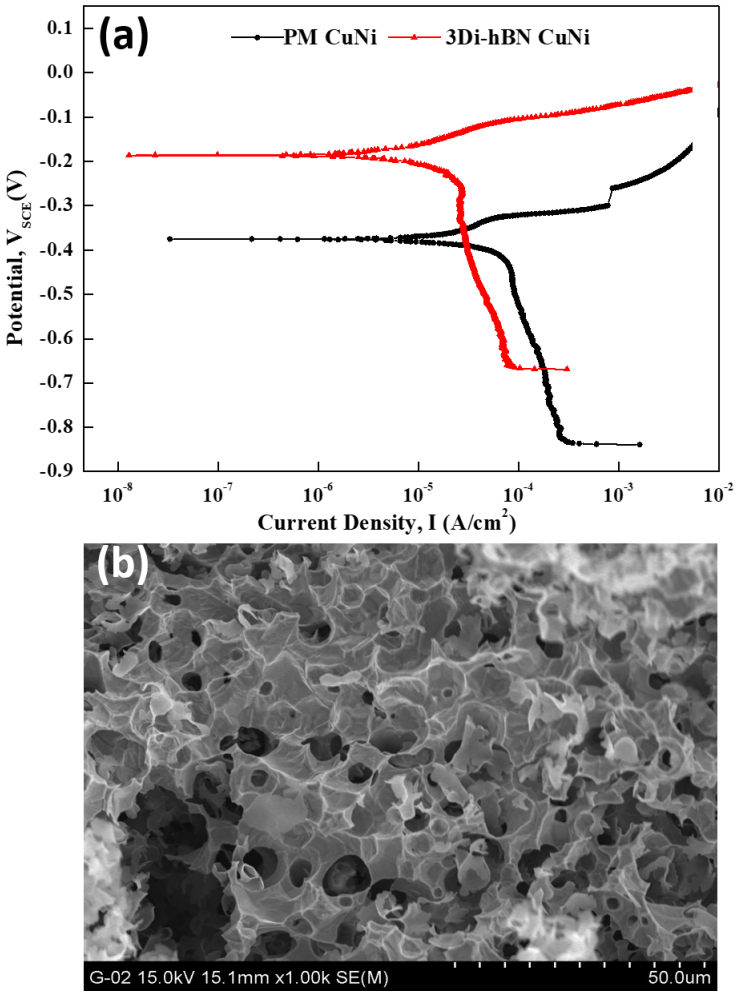

Figure 4.15: (a) Potentiodynamic polarization curves of 3Di-hBN CuNi composites and PM CuNi alloy, (b) and (c) SEM images and EDS analysis of 3Di-hBN CuNi composite, and (d) SEM image of 3Di-hBN.

Table 4.3: Electrochemical corrosion parameters.

Material	V_{corr} (mV)	I_{corr} (μA cm^{-2})	CR (mm year^{-1})
PM CuNi	−373.72	85.1	1.09
3Di-hBN CuNi	−182.59	14.0	0.183

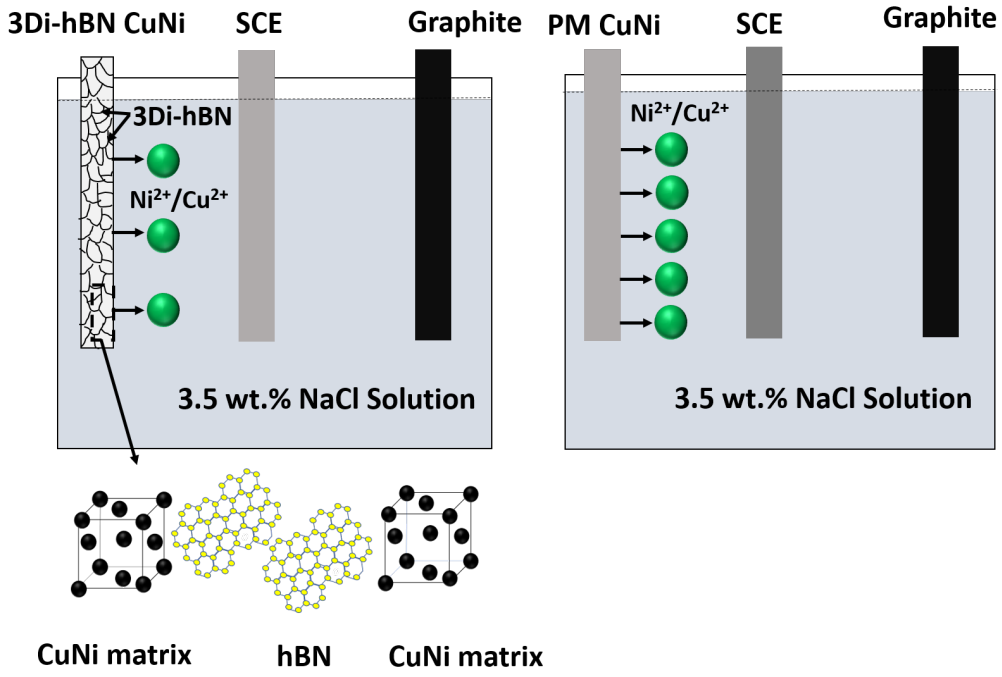

Figure 4.16: Schematic explanation of 3Di-hBN blocking the ions transport at metal-electrolyte interface.

and (b). The surface of PM CuNi alloy is much more corroded and rougher with large corrosion pits and depressions (Figure 4.17 (b)) compared to 3Di-hBN CuNi composite (Figure 4.17 (a)). Therefore, the examination of the SEM images further confirms the better corrosion resistance of 3Di-hBN CuNi composites compared to PM CuNi alloy.

The corrosion behavior of 3Di-hBN CuNi composite and PM CuNi alloy was also investigated by EIS. Bode plots are shown in Figures 4.18 (a) and (b) which indicate the plots of impedance (Z) versus frequency and phase engle versus frequency, respectively. Figures 4.18 (a) shows that impedance of 3Di-hBN CuNi composite was substantially higher (25%) than that of PM CuNi alloy which can be associated to a rise in charge transfer resistance owing to 3Di-hBN layers surrounding the Cu-Ni grains in 3Di-hBN CuNi composite. In particular, highe value of Z at low frequency implies the higher

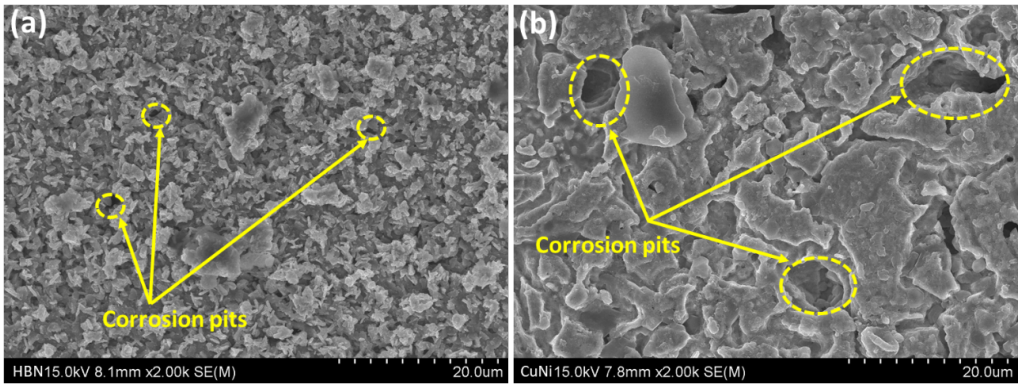

Figure 4.17: SEM images of the specimen surface for (a) 3Di-hBN CuNi composite and (b) PM CuNi alloy taken after electrochemical corrosion experiments.

corrosion resistance [192]. Figure 4.18 (b) shows a broad time constant that occurred in the high and medium frequency ranges for both 3Di-hBN CuNi composite and PM CuNi alloy [160, 192]. Nyquist plots along with equivalent electrical circuit (EEC) model for 3Di-hBN CuNi composite and PM CuNi alloy are shown in Figure 4.18 (c).

The larger size of the Nyquist plot of 3Di-hBN CuNi composite than that of PM CuNi alloy suggests the better anti-corrosion behavior of 3Di-hBN CuNi composite [193]. For both EIS spectra, an intercept at high frequency corresponding to electrolyte resistance, a portion of the semicircle at middle frequency, and an inclined line in the low frequency range corresponding to the Warburg impedance were observed (Figure 4.18 (c)). At lower frequencies, straight lines indicate that the corrosion mechanism is controlled not only by the charge transfer process but also by the diffusion of charged species through the corrosion products [194]. As shown in the EEC model (inset of Figure 4.18 (c)) for fitting the EIS spectra, R_s, R_{ct} and W_s represent solution resistance, charge transfer resistance and Warburg impedance, respectively. For PM CuNi alloy, the values of R_s, R_{ct} and W_s were found to be 29.26 Ωcm^2, 2×10^4 Ω cm^2 and 1.2×10^6 Ω cm^2, respectively which were smaller than those for 3Di-hBN CuNi composite (36.21 Ω cm^2 for R_s, 2.7×10^5 Ω cm^2 for R_{ct}, and 1.5×10^6 Ω cm^2 for W_s) as illustrated in Figure 4.18 (d). This

suggests the higher corrosion resistance of 3Di-hBN CuNi composite than that of PM CuNi alloy which can be attributed to the network of 3Di-hBN layers. 3Di-hBN network is likely to reduce the rate of electrochemical kinetics due to its high charge transfer resistance and block the diffusion of corrosion species into/out of the composite due to its impermeability.

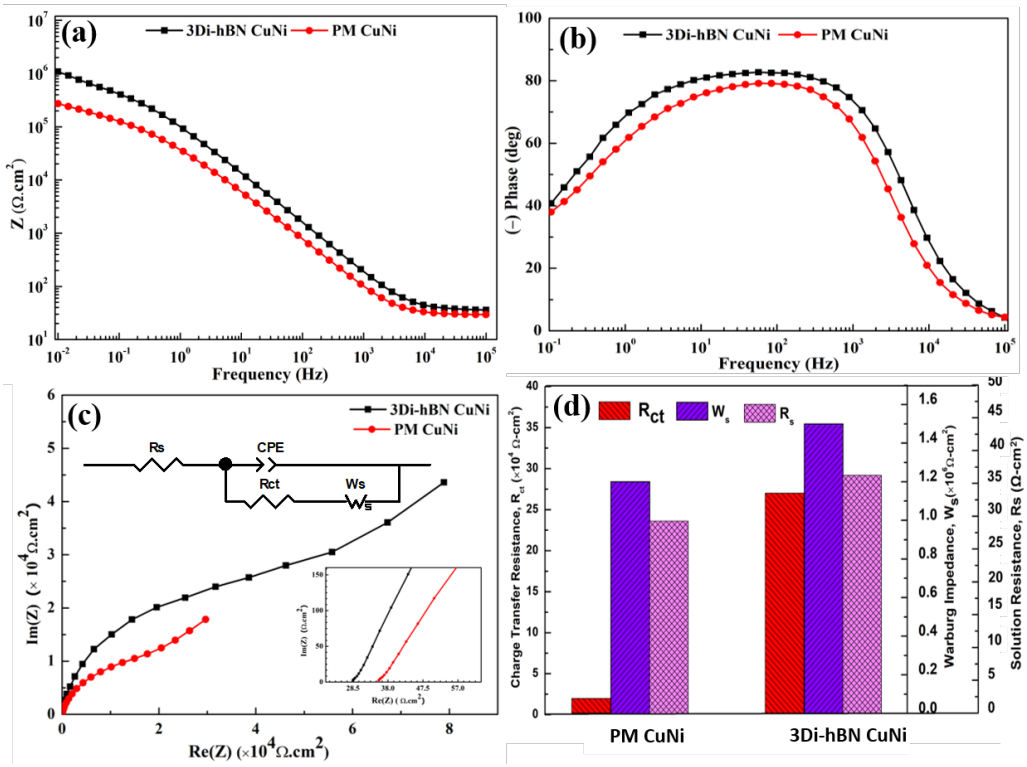

Figure 4.18: Bode plots of (a) impedance magnitude of 3Di-hBN CuNi and PM CuNi alloy (b) phase angle of 3Di-hBN CuNi and PM CuNi alloy, (c) Nyquist impedance plots for 3Di-hBN CuNi and PM CuNi alloy (Inset showing the ECC model), and (d) Electrochemical corrosion parameters obtained from EEC model.

4.2.4 High-Temperature Oxidation Behavior

The high-temperature oxidation behavior of 3Di-hBN CuNi composite and PM CuNi alloy was investigated by heating in air at 900°C for 48 h maximum. The formation

of oxides at high temperatures resulted in weight increase of both materials [195]. Nevertheless, the mass increase of 3Di-hBN CuNi composite was lower than that of PM CuNi alloy at each time point, as shown in Figure 4.19 (a). Thus, 3Di-hBN CuNi composite gained ~36.7% less mass (0.77 mg mm^{-2}) than PM CuNi alloy with a mass gain of 1.22 mg mm^{-2}. Moreover, Figure 4.19 (a) shows that PM CuNi alloy also gained mass faster than 3Di-hBN CuNi composites.

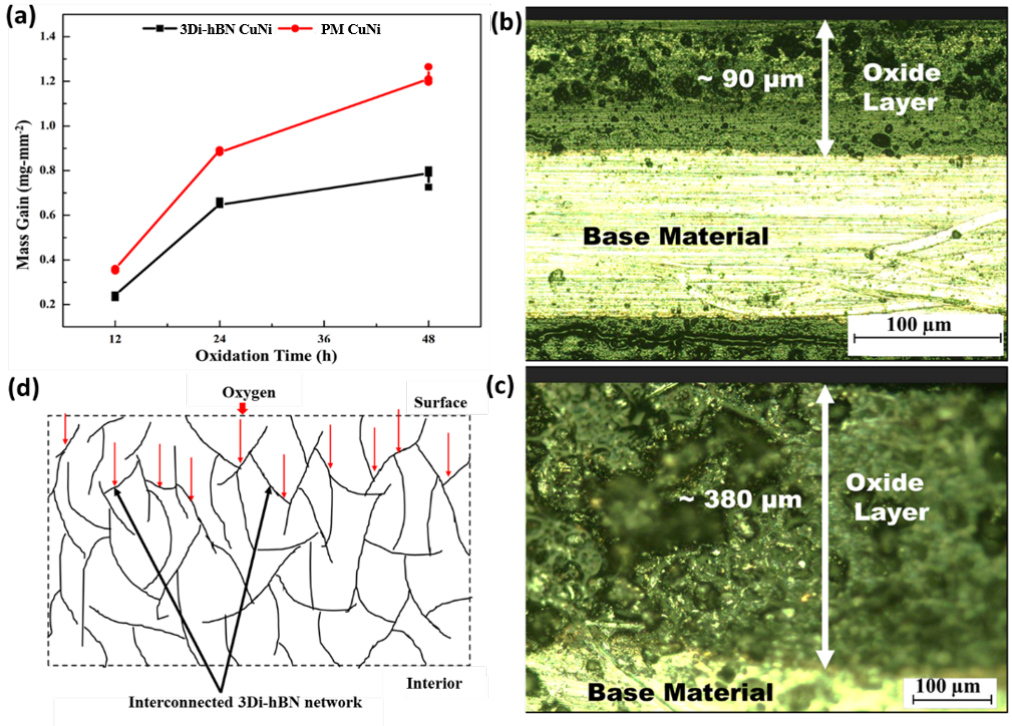

Figure 4.19: (a) High-temperature oxidation test results for 3Di-hBN CuNi composites and PM CuNi alloy, OM images of cross-sections of (b) 3Di-hBN CuNi composite and (c) PM CuNi alloy, and (d) Schematic illustrating the mechanism of hBN layers acting as barriers to oxygen diffusion to the interior of 3Di-hBN CuNi composite.

The improved anti-oxidation behavior of 3Di-hBN CuNi composite can also be observed from the OM images of 3Di-hBN CuNi and PM CuNi alloy obtained after performing high-temperature oxidation experiments, as shown in Figures 4.19 (b) and

(c). After oxidation of the samples at 900°C for 48 h, the cross-section was observed microscopically by cutting the oxidized disk into two halves. Figure 4.19 (b) shows that an oxide layer of ∼90 µm was formed on 3Di-hBN CuNi composite, while an oxide layer of ∼380 µm was formed on PM CuNi alloy, as shown in Figure 4.19 (b). The oxide layer formed on 3Di-hBN CuNi is at least four times thinner than that formed on PM CuNi alloy, which may be due to the fact that 3Di-hBN blocks the penetration of oxygen into the metal matrix at the interfaces of CuNi grains at high temperatures.

We believe that following two properties of hBN are responsible for 3Di-hBN CuNi composite to exhibit such behavior. (i) Unlike graphene, hBN is thermodynamically stable at high temperatures [195–199]. The high-temperature stability of 3Di-hBN was

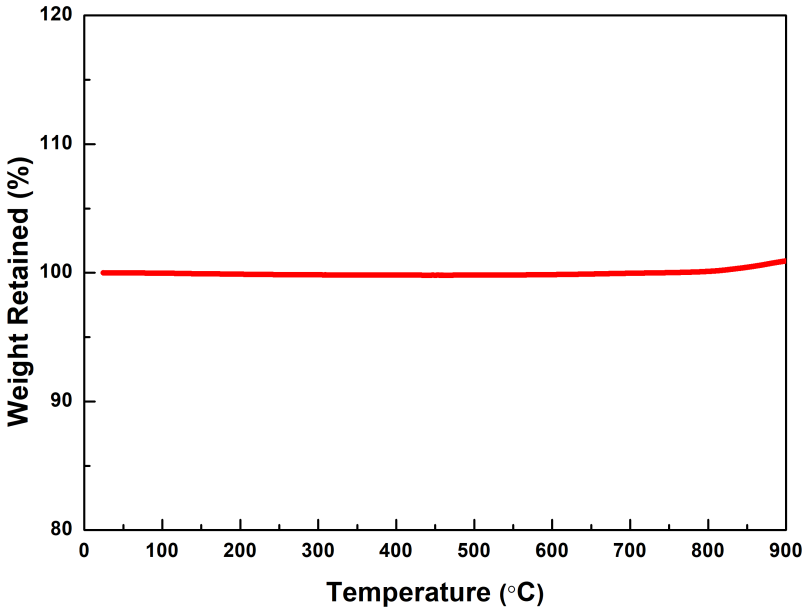

Figure 4.20: TGA analysis of 3Di-hBN CuNi composite.

indirectly confirmed by performing thermogravimetric analysis (TGA) of 3Di-hBN CuNi composite, as shown in Figure 4.20, up to a temperature of 900°C in N_2 environment.

The results indicate negligible bulk degradation of 3Di-hBN CuNi composite up to ~900°C, suggesting thermodynamically stable hBN in 3Di-hBN CuNi composite. (ii) The impermeability of hBN enables it to block the penetration of small atoms, ions and molecules [160, 189, 191]. Therefore, 3Di-hBN resists oxygen penetration into 3Di-hBN CuNi composite at elevated temperature while being themodynamically stable, as schematically shown in Figure 4.19 (d). The improved high-temperature anti-oxidation behavior due to hBN has been extensively reported in the literature [195, 200]. Considering the high-temperature applications of CuNi-based alloys in industry, hBN reinforcement could be of great benefit.

4.3 Synthesis of 3DiGr CuNi Composites

4.3.1 Mechanism of Formation of 3DiGr

The synthesis of 3DiGr CuNi composite is shown schematically in Figure 4.21. Cu and Ni particles are compacted into a disc after carefully mixing as explained in Section 3.2.1. During sintering, the excess surface energy of the particles acts as the driving force for the diffusion which leads to the reduction in volume and eventual formation of solid solution of Cu and Ni [171, 172]. As a result, the volume of the compact disc shrinks and thus densification occurs. At a certain time when CVD started, methane decomposed into C and hydrogen at 1000°C according to the following equation (4.5).

$$CH_{4(g)} \rightarrow [C] + 2H_{2(g)} \tag{4.5}$$

These carbon atoms diffused into the interior of the disc. The concentration gradient leads to the diffusion of the C atoms into the free spaces in the disc. In this way, a solid solution of Cu, Ni and C is formed at 1000°C, in which the carbon atoms occupy the interstices of the CuNi alloy. Eventually, the diffused carbon atoms precipitate out of the CuNi alloy upon cooling, nucleate and grow along the grain boundaries, forming a

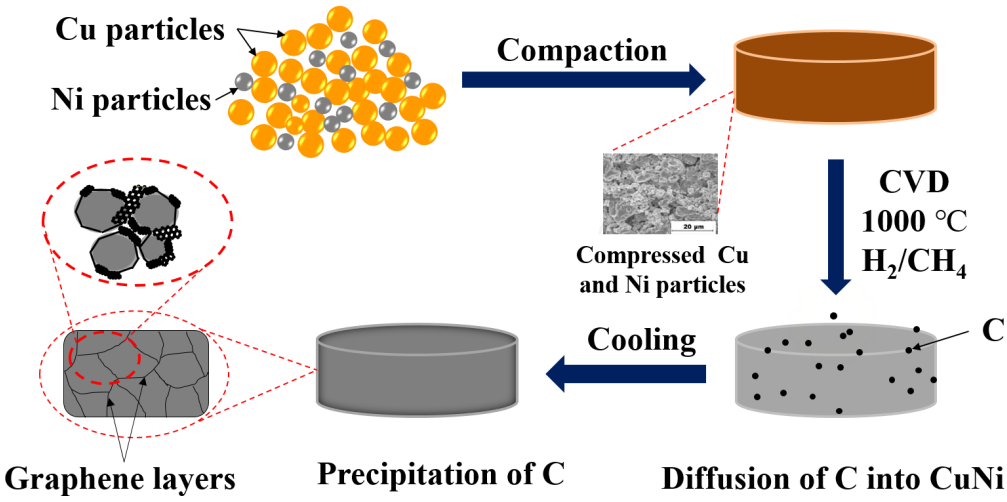

Figure 4.21: Synthesis of 3DiGr CuNi composites.

3DiGr CuNi composite [43]. To summarize, 3DiGr is formed in 3DiGr CuNi composite in following steps:

- The reduction of distance between Cu and Ni particles during sintering under driving force due to reduction of surface energy.
- The diffusion of Cu into Ni and vice versa.
- The formation of CuNi solid solution.
- The diffusion of atomic carbon in the solid solution of CuNi during CVD.
- The precipitation of C atoms out from CuNi grains during cooling.
- The nucleation and growth of graphene along the grain boundaries of CuNi.

4.3.2 Microstructural Investigation

The densities of 3DiGr CuNi composite as a function of compaction pressure are shown in Figure 4.22 (a). As the compaction pressure increases, the density also increases

until a certain value of the compaction pressure is reached above which the density stops increasing. This trend of density-pressure relationship has been discussed in detail in Section 4.1.2. Figures 4.22 (c) and (d) are the OM images of 3DiGr CuNi composites prepared at compaction pressures of 55 MPa and 280 MPa, respectively. In these images, the graphite-filled voids (some of which are shown with dashed white circles) and CuNi grains can be seen. The number of graphite sites is higher in the composite prepared under a compaction pressure of 55 MPa (Figures 4.22 (c)) compared to the composite prepared under a compaction pressure of 280 MPa (Figures 4.22 (d)). This is consistent with the XRD patterns shown in Figures 4.22 (b), which show that more graphite was formed at lower compaction pressure (55 MPa), as indicated by the visible graphite peak (002) at 26.7°. However, no graphite peak (002) was observed at higher compaction pressure, suggesting that mostly graphene layers were formed at the grain boundaries of the CuNi matrix [21].

Figure 4.23 (a) shows the SEM image of the 3DiGr foam obtained by etching, washing, and freeze-drying, as explained in Section 3.4.2.2. The graphene layers are interconnected and form a network with channels and pockets. Moreover, the partially etched surface of 3DiGr CuNi composite contains an interconnected network of graphene layers with a large surface area, as shown in Figure 4.23 (b). EDS of the partially etched 3DiGr CuNi surface revealed that the surface is composed of carbon atoms, Cu, and Ni as shown in Figures 4.23 (c) and (d). We believe that such CuNi-graphene composites can be used either directly or after slight modification in devices used for energy generation or storage.

Recently, it has been reported that metals as caytalysts in oxidation-reduction reactions (ORR) do not contribute to the catalytic function, however, play a role in the formation of active sites [21]. Carbon materials such as carbon nanotubes, graphene and graphite foam can function as electrochemically active materials for ORR [201, 202]. In our work, the electrolytic activity of the free-standing interconnected graphene network

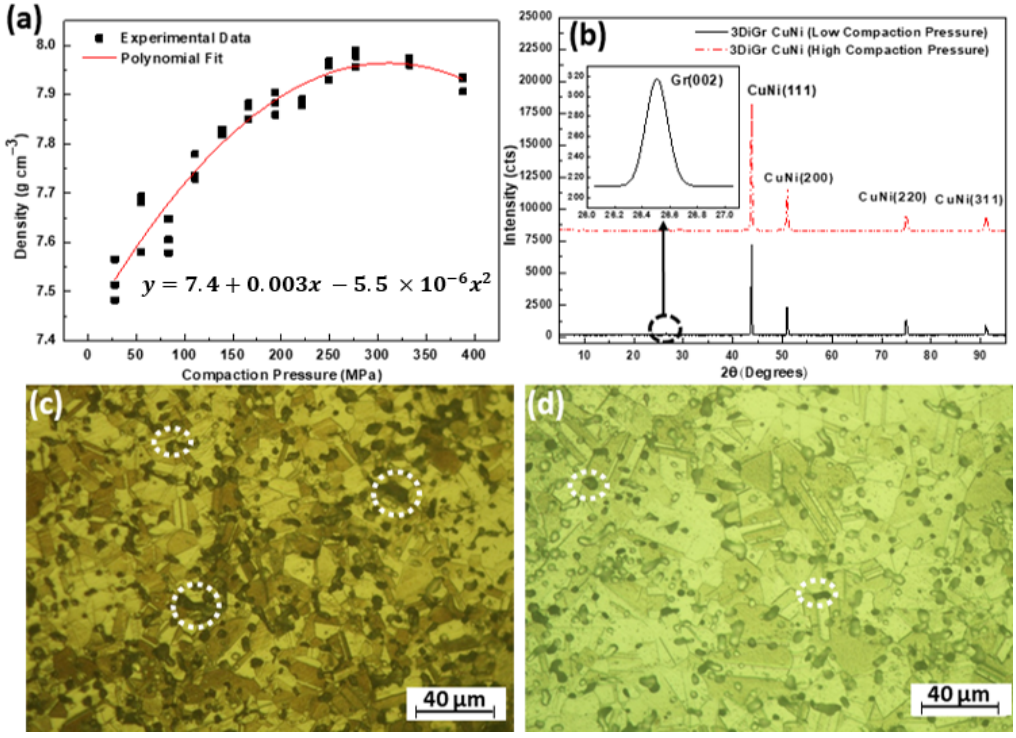

Figure 4.22: (a) Compaction pressure-density relationship, (b) XRD patterns for 3DiGr CuNi composite, and OM images of 3DiGr CuNi composite at compaction pressure of (c) 55 MPa and (d) 280 MPa.

on the surface of 3DiGr CuNi composite was investigated by performing voltammograms of the rotating ring-disk electrode.

Figure 4.24 shows the cyclic voltammogram of the partially etched 3DiGr CuNi composite for different scan rates. It can be seen that the large surface area graphene network on the surface of 3DiGr CuNi composite shows the catalytic activity. The net peak current density approaches 320 mA and the capacitance stabilized at ∼32% at a scan rate of 100 mV s^{-1}. However, recent studies suggest that the catalytic activity for ORR is enhanced when carbon materials are doped with nitrogen [201]. Since the electronegativity of nitrogen is higher than that of carbon, it attracts the electrons of neighboring carbon atoms, resulting in partially positively charged carbon atoms that

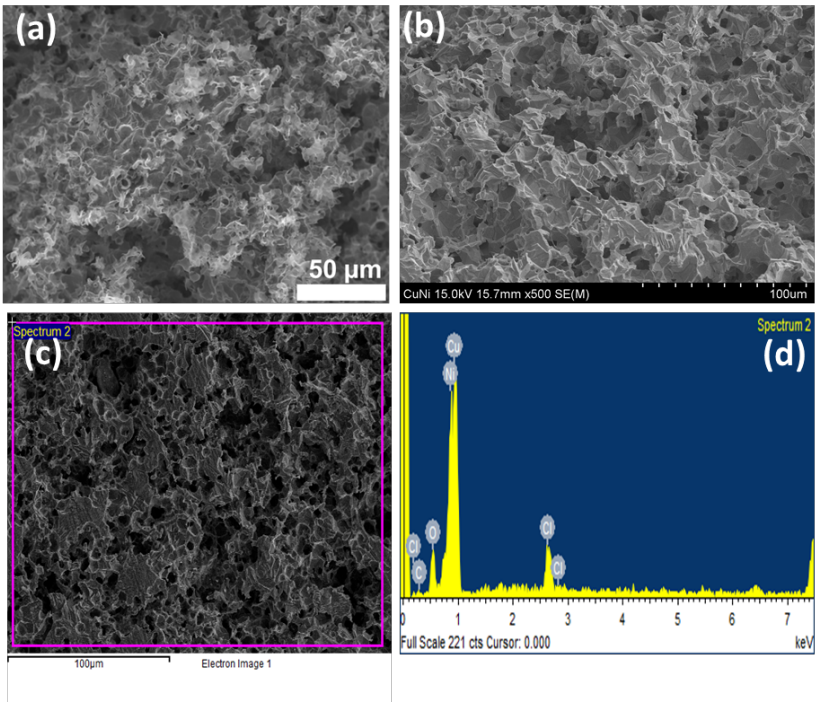

Figure 4.23: (a) Microstructure of 3DiGr, (b) microstructure of partially etched 3DiGr CuNi composite, and (c-d) EDS analysis of partially etched 3DiGr CuNi composite.

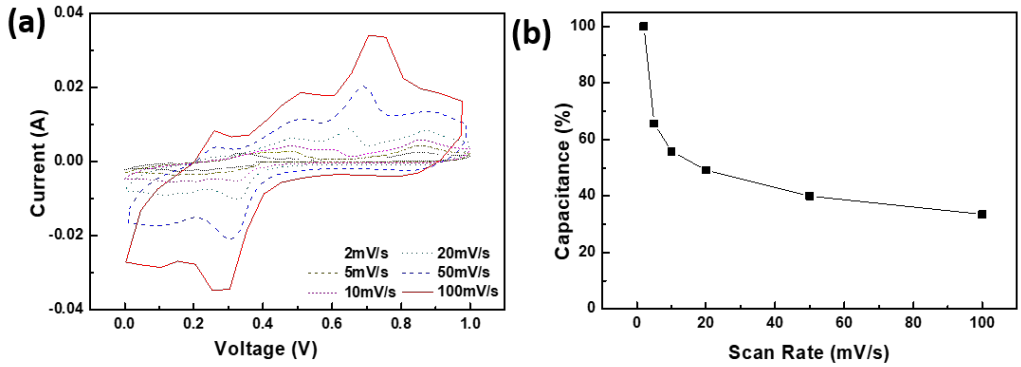

Figure 4.24: (a) Voltammogram and (b) capacitance vs scan rate of fuel cell for 3DiGr CuNi composite being used as electrode.

act as active sites for the activation of the O_2 molecule in the ORR [201]. Therefore, this study can be extended to fabricate a three-dimensional interconnected network of N-doped graphene to further improve the electrochemical performance.

In our nanomaterials laboratory, a simple two-step process was used to form the three dimensionally interconnected network of graphene in the Cu matrix. After complete etching of the Cu matrix, the quality of the graphene was investigated by Raman spectroscopy [43] as shown in Figure 4.25. Typical D, G and 2D peaks are seen at 1350 cm^{-1}, 1580 cm^{-1} and 2700 cm^{-1}, respectively. Generally, the D band is known as the defect band and is associated with disorder between graphene layers, while the G band reflects the crystallization and symmetry of graphene [203]. Moreover, the 2D band is a double phonon resonance peak and reflects the stacking degree of graphene, which is a typical symbol of the existence of graphene [203]. The intensity ratio (I_D/I_G) reflects the

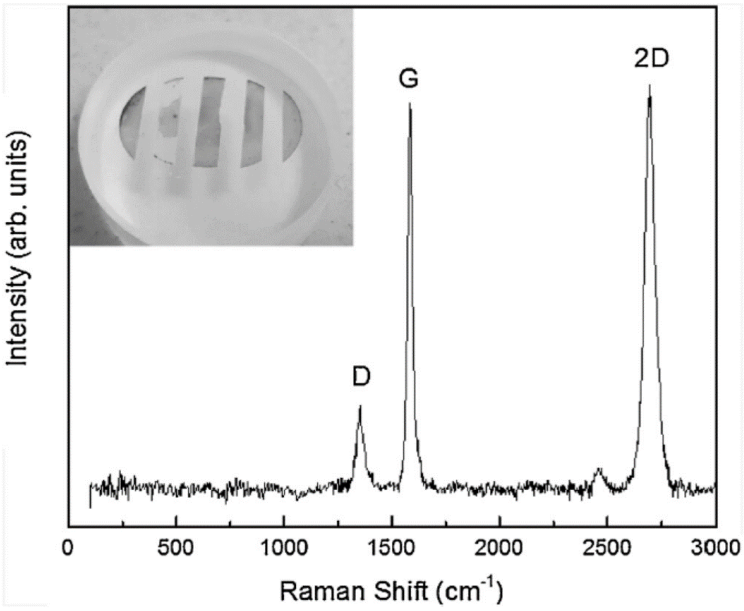

Figure 4.25: Raman spectrum of 3DiGr [43]. Analyzed based on Ref [204]. (Reused with permission from Elsevier under license number 5207361331890. See Appendix 'E')

defects of graphene structure. In the present three dimensionally interconnected network, the ratios I_D/I_G and I_{2D}/I_G were found to be 0.28 and 1, respectively, indicating the high-quality graphene with few layers.

4.4 Properties of 3DiGr CuNi Composites

4.4.1 Thermal Conductivity

The thermal conductivities of 3DiGr CuNi composite (25.6 ± 1.4 W $m^{-1}K^{-1}$) and PM CuNi alloy (16 ± 0.5 W $m^{-1}K^{-1}$) are shown in Figure 4.26. It was found that the thermal conductivity of the 3Di-Gr CuNi composite was ∼ 58% higher than that of PM CuNi alloy. The uniform and homogeneous distribution of graphene in the metal matrix is required to achieve an improvement in thermal conductivity [205]. The enhanced thermal conductivity of 3DiGr CuNi composite suggests that a three-dimensionally interconnected network of graphene must form surrounding the grains of CuNi to facilitate the electron movement [28].

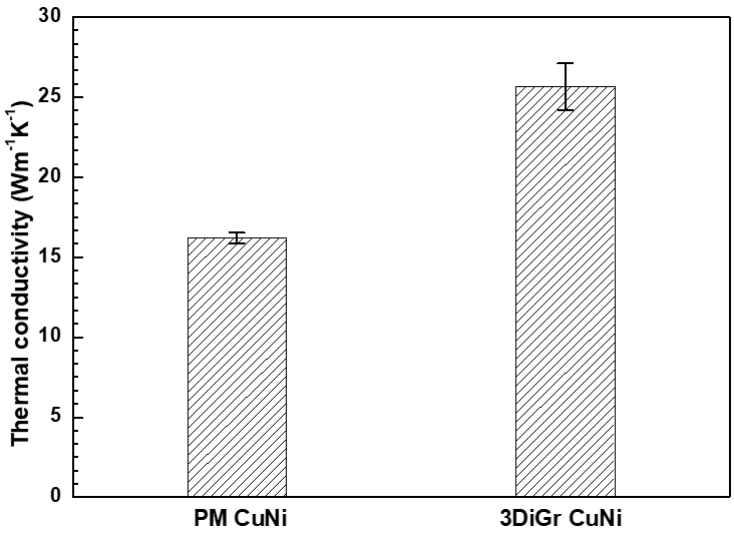

Figure 4.26: Thermal conductivities of PM CuNi and 3DiGr CuNi composite.

4.4.2 Electrochemical Corrosion Behavior

The potentiodynamic polarization curves of PM CuNi and 3DiGr CuNi composite are shown in Figure 4.27. The intersection of the cathodic and anodic polarization curves gives the corrosion current density (I_{corr}) and the corrosion potential (V_{corr}). 3DiGr CuNi composite exhibited better corrosion resistance than PM CuNi alloy. The corrosion potential of 3DiGr CuNi composite (−0.220 V) was shifted in a more positive (upward) direction than that of PM CuNi alloy (−0.373 V), as shown by the polarization curves of 3Di-hBN CuNi composite and PM CuNi alloy in Figure 4.27. It was also found that the I_{corr} of 3DiGr CuNi composite (4.16 μA cm^{-2}) was lower than that of PM CuNi alloy (85.1 μA cm^{-2}). The lower value of I_{corr} also indicates that the corrosion resistance of 3DiGr CuNi is significantly improved [206, 207]. In corrosion thermodynamics, the

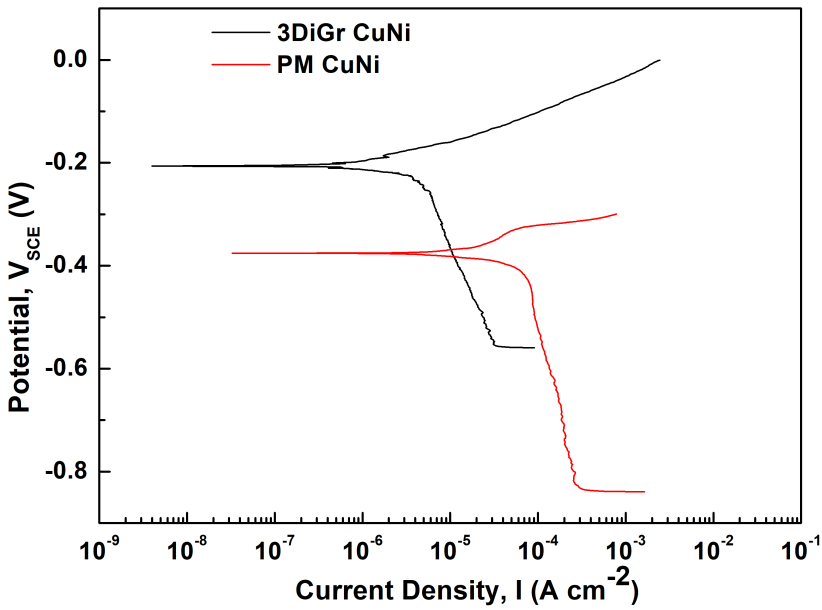

Figure 4.27: Potentiodynamic polarization curves of PM CuNi and 3DiGr CuNi composite.

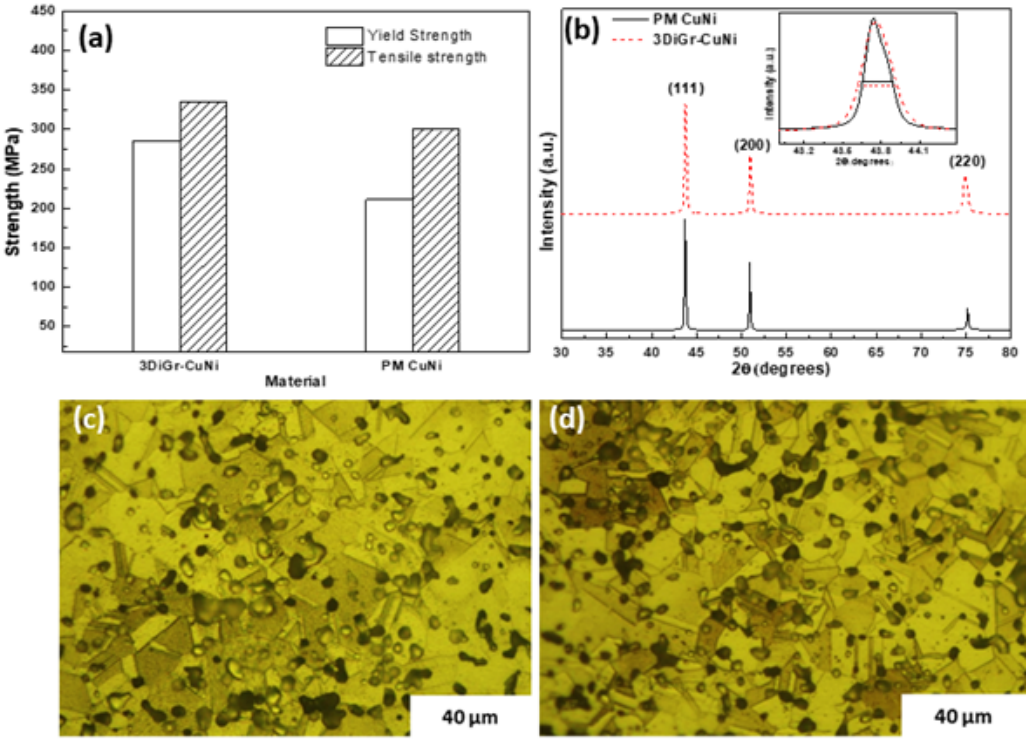

Figure 4.28: (a) YS and UTS (b) XRD patterns of 3DiGr CuNi and PM CuNi alloy, OM images of (c) PM CuNi alloy and (d) 3DiGr CuNi composite.

higher the V_{corr} is, the better the anti-corrosion property is [206, 207]. Similarly, a lower I_{corr} is a measure of better anti-corrosion property (higher corrosion resistance). In corrosion kinetics, the corrosion rate (CR) is directly proportional to I_{corr}; this means that a higher value of I_{corr} would result in a larger CR.

Table 4.4: Electrochemical corrosion parameters for 3DiGr CuNi and PM CuNi.

Specimen type	I_{corr} (μA cm^{-2})	V_{corr}, (V)
PM CuNi	85.1	− 0.373
3DiGr CuNi	4.16	− 0.220

4.4.3 Tensile Strength

Figure 4.28 (a) shows that 3DiGr CuNi composite has ∼25.9% and ∼10.1% higher YS and UTS, respectively, compared to PM CuNi alloy. The higher strength could be due to the graphene at the grain boundaries of 3DiGr CuNi composite, which acts as a barrier to the dislocation motion [141]. The higher strength of 3DiGr CuNi composite can be further related to the higher grain refinement in its microstructure compared to PM CuNi alloy. Figure 4.28 (b) shows the XRD pattern of 3DiGr CuNi composite and PM CuNi alloy. The peak of 3DiGr CuNi composite was found slightly broader than that of PM CuNi alloy, suggesting that the structure of 3DiGr CuNi composite was more refined. The magnified peaks (111) are shown in the inset of Figure 4.28 (b) as an example. Grain refinement can also be seen when viewing the OM images (Figures 4.28 (c) and (d)). The average grain size for 3DiGr CuNi composite was 20-30 μm compared to PM CuNi alloy with a grain size of 40-50 μm. The grain refinement in the microstructure could be related to the fact that the graphene inhibits the grain growth of the CuNi matrix at the time of synthesis (diffusion), resulting in smaller grains. This in turn leads to an increased strength of 3DiGr CuNi composite according to the classical Hall-Petch relationship [149].

5 CONCLUSIONS AND FUTURE SCOPE

5.1 Conclusions

3Di-hBN CuNi and 3DiGr CuNi composites were succefully fabricated using a simple two-step process that involves the compaction of the powder followed by MOCVD or CVD. Microstructural invetigations revealed that three dimensionally interconnected networks of hBN and graphene were formed surrounding the grains of CuNi matrix. The experimental outcomes can be summarized as folllows:

5.1.1 3Di-hBN CuNi Composite

1. The mechanical properties increased with increasing density. 3Di-hBN CuNi composite showed 16.3%, 11.67% and 27.9% higher yield strength, UTS, and fracture toughness, respectively, compared to PM CuNi alloy. This improvement in mechanical properties could be related to the three dimensionally interconnected network of hBN (3Di-hBN) formed around the grains of CuNi matrix. 3Di-hBN served as a load transfer unit when the composite is subjected to deformation due to (i) a continuous network of hBN layers and (ii) good interfacial bonding of hBN to the matrix. Strong interfacial bonding likely prevents dislocation movement and crack propagation when an external load is applied. In addition, the formation of 3Di-hBN at grain boundaries during MOCVD prevents excessive grain growth and thus improves mechanical performance through grain refinement.

2. The thermal conductivity of 3Di-hBN CuNi composite was $\sim$10% higher than that of PM CuNi alloy, which may be due to the fact that 3Di-hBN provides a conductive path for electron movement at the grain boundaries.

3. Electrochemical corrosion experiments showed that 3Di-hBN CuNi composites exhibited better anti-corrosion behavior than PM CuNi alloy. The corrosion rate of 3Di-hBN CuNi composite was calculated to be 0.183 mm year^{-1} which is

about one-sixth of the corrosion rate of PM CuNi alloy. These results show that the corrosion resistance of 3Di-hBN CuNi composite is increased by more than six times compared to PM CuNi alloy. It was shown that 3Di-hBN in 3Di-hBN CuNi composite effectively blocked the penetration of molecules or ions into the composite, thereby improving the corrosion resistance. Moreover, the electrochemical impedance spectroscopy results confirm the improved anti-corrosion property of 3Di-hBN CuNi composites.

4. The mass gain versus oxidation time curves showed that 3Di-hBN CuNi composite gained about 36% less weight during the high-temperature oxidation for 48 hours at 900°C; 3Di-hBN CuNi composite is more stable at high temperature and less affected by the environment compared with PM CuNi alloy. This could be due to the formation of the network of 3Di-hBN layers at the interfaces of CuNi grains. Since hBN is stable at high temperatures and impermeable to oxygen, the oxide formation (oxygen penetration/diffusion) in 3Di-hBN CuNi composite was significantly reduced.

5.1.2 3DiGr CuNi Composite

1. The voltammograms of the rotating ring-disc electrode showed the catalytic activity on the modified surface of the 3DiGr CuNi composite, indicating that the slightly modified surface can be used in energy storage devices such as batteries and fuel cells.

2. 3DiGr provided a conductive path for electron mobility, resulting in $\sim$58% higher thermal conductivity compared to PM CuNi alloy without 3DiGr. This was attributed to the good interfacial bonding of graphene to the CuNi matrix and its high thermal conductivity.

3. Finally, the yield strength and ultimate tensile strength of 3DiGr CuNi composite

were 25.9% and 10.1% higher than PM CuNi alloy, respectively, which can be related to the grain refinement and dislocation strengthening in the structure caused by graphene. During CVD, the formation of graphene at the grain boundaries hinders the grain growth of the CuNi solid solution, resulting in grain refinement of the structure.

5.2 Future Scope

Based on the present research work, the following work can be carried out as a future scope to enrich/reveal this field further.

It has now been established by experimentation in this research work as well as in several other researches that the presence of hBN or graphene at matrix grain boundaries impart good attributes to the composites such as higher thermal conductivity, strength and corrosion resistance. However, atomistic simulation can prove to be useful tool to further refining and generalizing the results. For instance, molecular dynamics study for the graphene/hBN reinforced Cu/CuNi composites needs to be conducted to characterize their thermal, mechanical, and chemical properties. This can be done by modeling the grains (from 2 to 4) and investigating the effect of graphene between the grain boundaries under the effect of applied loading (chemical, thermal or mechanical). This could be helpful in optimising the processing parametrs and reducing the associated cost and energy.

Secondly, mechanical properties could be affected when a material is subjected to hydrogen at high pressure and temperature and the phenomenon is known as hydrogen embrittlement [208]. In this context, graphene (or hBN) at the interface of Cu grains might act as an effective barrier to hydrogen penetration inside the composite thereby maintaining the strength of the material subjected to severe hydrogen exposure. Therefore, mechanical properties of 3DiGr CuNi and 3Di-hBN CuNi composites can be investigated before and after exposure to the hydrogen environment. Furthermore, Cu

and Ni based alloys are widely used in nuclear power plants, however, these materials become embrittled over the time due to nuclear irradiation. Neutron irradiation leads to formation of transmutation products, irradiation defects, dislocation loops, and stacking fault tetrahedra and voids [209]. All these features result in reduction of electrical and thermal conductivities. Various studies show that 2D materials are impermeable to the particles having sizes as small as neutron [209]. In this context, physical and mechanical properties of 3Di-hBN or 3DiGr reinforced Cu/CuNi composites must be investigated under the effect of nuclear irradiation.

PUBLICATIONS

1. Zahid Hussain, Haneul Jang, HyunJoo Choi and Byung-Sang Choi.

   ”Microstructure, Mechanical Behavior, and Thermal Conductivity of Three-Dimensionally Interconnected hBN Reinforced Cu-Ni Composite”. Journal of Materials Engineering and Performance (published online on 24 November, 2021).

2. Zahid Hussain, Hye-Won Yang, and Byung-Sang Choi. ”Synthesis of Three-Dimensionally Interconnected Hexagonal Boron Nitride Networked Cu-Ni Composite”. Korean Journal of Metals and Materials 2021; 59(7): 505-513.

3. Zahid Hussain, Jung-Soo Lee and Byung-Sang Choi. ”Graphene Reinforced CuNi Composite Fabricated by a Simple Two-step Process”. J. of Advanced Engineering and Technology (Under review).

4. Li Xue, Zahid Hussain and Byung-Sang Choi. ”Three-dimensionally Interconnected Graphene Networked Cu-Ni Composite Fabricated by a Simple Two Steps Process”. (2019 autumn conference), The Korean institute of Metals and Materials, poster presentation.

5. Zahid Hussain, Hye-Won Yang and Byung-Sang Choi. ”Synthesis of Three-Dimensionally Interconnected Hexagonal Boron Nitride Networked Cu-Ni Composite”. (2020 spring conference), The Korean institute of Metals and Materials, poster presentation.

6. Zahid Hussain and Byung-Sang Choi. ”Corrosion behavior of hexagonal boron nitride reinforced Cu-Ni composite”.(2021 spring conference), The Korean institute of Metals and Materials, poster presentation.

BIBLIOGRAPHY

1. Zhang, J, Perez, R. & Lavernia, E. Documentation of damping capacity of metallic, ceramic and metal-matrix composite materials. *Journal of materials science* **28,** 2395–2404 (1993).

2. Ercetin, A. & Pimenov, D. Y. Microstructure, Mechanical, and Corrosion Behavior of Al2O3 Reinforced Mg2Zn Matrix Magnesium Composites. *Materials* **14,** 4819 (2021).

3. Etaat, M., Pouraliakbar, H., Khalaj, G. & Ghambari, M. Adhesion strength measurement of nickel layer on the iron-based P/M parts influenced by different surface pre-treatment operations. *Measurement* **66,** 204–211 (2015).

4. Jia, P. Fabrication and Properties of Cu-SiC-GNP composites (2018).

5. Rawal, S. P. Metal-matrix composites for space applications. *Jom* **53,** 14–17 (2001).

6. Moheimani, S. K., Dadkhah, M. & Saboori, A. Development of Novel AlSi10Mg Based Nanocomposites: Microstructure, Thermal and Mechanical Properties. *Metals* **9,** 1000 (2019).

7. Cai, S. *et al.* Fabrication of three-dimensional graphene/Cu-Ag composites by in situ chemical vapor deposition and their properties. *Journal of Materials Engineering and Performance* **29,** 2248–2255 (2020).

8. Hu, Z *et al.* Graphene-reinforced metal matrix nanocomposites–a review. *Materials Science and Technology* **32,** 930–953 (2016).

9. Kasar, A. K., Xiong, G. & Menezes, P. L. Graphene-reinforced metal and polymer matrix composites. *Jom* **70,** 829–836 (2018).

10. Wadhwa, A. S. & Chauhan, A. An overview of the controllable process parameters in mechanical characterization of developed hybrid metal matrix composites and their optimization for advanced engineering applications. *Materials Today: Proceedings* **28,** 1295–1301 (2020).

11. Dong, X., Hu, J., Wang, H., Liu, S. & Guo, Z. A study on carbon concentration distribution and microstructure of P/M materials prepared by carbusintering. *Journal of Materials Processing Technology* **209,** 3776–3782 (2009).

12. El-Tantawy, A., Daoush, W. M. & El-Nikhaily, A. E. Microstructure and properties of BN/Ni-Cu composites fabricated by powder technology. *Journal of Experimental Nanoscience* **13,** 174–187 (2018).

13. Zhao, P., Chen, Z. & Dong, C. Failure analysis of warm stamping of magnesium alloy sheet based on an anisotropic damage model. *Journal of materials engineering and performance* **23,** 4032–4041 (2014).

14. Trojanová, Z., Dash, K., Máthis, K., Lukáč, P. & Kasakewitsch, A. Elastic and plastic behavior of an ultrafine-grained Mg reinforced with BN nanoparticles. *Journal of Materials Engineering and Performance* **27,** 3112–3121 (2018).

15. Ercetin, A., Özgün, Ö. & Aslantas, K. Investigation of mechanical properties of Mg5Sn-xZn alloys produced through new method in powder metallurgy. *Journal of Testing and Evaluation* **49** (2021).

16. Wen, X. & Joshi, R. 2D materials-based metal matrix composites. *Journal of Physics D: Applied Physics* **53,** 423001 (2020).

17. Pouraliakbar, H *et al.* Toughness prediction in functionally graded Al6061/SiCp composites produced by roll-bonding. *Ceramics International* **40,** 8809–8825 (2014).

18. Pouraliakbar, H., Nazari, A., Fataei, P., Livary, A. K. & Jandaghi, M. Predicting Charpy impact energy of Al6061/SiCp laminated nanocomposites in crack divider and crack arrester forms. *Ceramics International* **39,** 6099–6106 (2013).

19. Brockenbrough, J., Suresh, S. & Wienecke, H. Deformation of metal-matrix composites with continuous fibers: geometrical effects of fiber distribution and shape. *Acta metallurgica et materialia* **39,** 735–752 (1991).

20. Farahmand, S., Monazzah, A. H. & Soorgee, M. H. The fabrication of Al2O3–Al FGM by SPS under different sintering temperatures: microstructural evaluation and bending behavior. *Ceramics International* **45,** 22775–22782 (2019).

21. Chu, K. & Jia, C. Enhanced strength in bulk graphene–copper composites. *physica status solidi (a)* **211,** 184–190 (2014).

22. Naseer, A. *et al.* A review of processing techniques for graphene-reinforced metal matrix composites. *Materials and Manufacturing Processes* **34,** 957–985 (2019).

23. Monazzah, A. H., Pouraliakbar, H., Bagheri, R. & Reihani, S. M. S. Al-Mg-Si/SiC laminated composites: fabrication, architectural characteristics, toughness, damage tolerance, fracture mechanisms. *Composites Part B: Engineering* **125,** 49–70 (2017).

24. Singh, S. P., Joshi, R. & Singla, V. *Effect of Hexa Boron Nitride and REO Addition on Wear and Corrosion Behavior of Hard-Facing on Mild Steel* PhD thesis (2018).

25. Elkady, O. A., Abu-Oqail, A., Ewais, E. M. & El-Sheikh, M. Physico-mechanical and tribological properties of Cu/h-BN nanocomposites synthesized by PM route. *Journal of Alloys and Compounds* **625,** 309–317 (2015).

26. Liu, Z. *et al.* Ultrathin high-temperature oxidation-resistant coatings of hexagonal boron nitride. *Nature communications* **4,** 1–8 (2013).

27. Duan, X. *et al.* Review on the properties of hexagonal boron nitride matrix composite ceramics. *Journal of the European Ceramic Society* **36,** 3725–3737 (2016).

28. Li, X., Ring, T. A. & Choi, B.-S. Thermal Conductivity of Three-Dimensionally Interconnected Graphene-Networked Cu Composite Fabricated by a Simple Two-Step Process. *Korean Journal of Metals and Materials* **57,** 529–534 (2019).

29. Chen, Y. *et al.* Fabrication of in-situ grown graphene reinforced Cu matrix composites. *Scientific reports* **6,** 1–9 (2016).

30. Kim, S.-E. & Shon, I.-J. Rapid sintering of nanocrystalline (W, Ti) C-graphene composites. *Journal of the Korean Institute of Metals and Materials* **56,** 854–860 (2018).

31. Wu, M. *et al.* High oxidation resistance of CVD graphene-reinforced copper matrix composites. *Nanomaterials* **9,** 498 (2019).

32. Tripathi, K., Gyawali, G. & Lee, S. W. Graphene coating via chemical vapor deposition for improving friction and wear of gray cast iron at interfaces. *ACS applied materials & interfaces* **9,** 32336–32351 (2017).

33. Gopinath, S, Prince, M & Raghav, G. Enhancing the mechanical, wear and corrosion behaviour of stir casted aluminium 6061 hybrid composites through the incorporation of boron nitride and aluminium oxide particles. *Materials Research Express* **7,** 016582 (2020).

34. Reddy, A. C. *Study of factors influencing sliding wear behavior of hexagonal boron nitride reinforced AA6061 metal matrix composites* in *5th International Conference on Modern Materials and Manufacturing, Bangalore* (2013), 409–413.

35. Zitoun, E. & Reddy, A. C. *Microstructure-Property Relationship of AA3003/Boron Nitride Particle-Reinforced Metal Matrix Composites Cast by Bottom-Up Pouring* in *6th National Conference on Materials and Manufacturing Processes, Hyderabad* (2008), 115–119.

36. Khatavkar, M. R. A., Mandave, A. K., Baviskar, D. D. & Shinde, S. L. Influence of Hexagonal Boron Nitride on Tribological Properties of AA2024-hBN Metal Matrix Composite. *Int. Res. J. Eng. Technol.* **5** (2018).

37. Cho, W.-J. & Shon, I.-J. Effect of BN addition on the mechanical properties of TiN-BN composites. *Korean Journal of Metals and Materials* **56,** 658–663 (2018).

38. Li, J. *et al.* Microstructure and tensile properties of bulk nanostructured aluminum/graphene composites prepared via cryomilling. *Materials Science and Engineering: A* **626,** 400–405 (2015).

39. Cao, M. *et al.* Aligning graphene in bulk copper: Nacre-inspired nanolaminated architecture coupled with in-situ processing for enhanced mechanical properties and high electrical conductivity. *Carbon* **117,** 65–74 (2017).

40. Jiang, R., Zhou, X., Fang, Q. & Liu, Z. Copper–graphene bulk composites with homogeneous graphene dispersion and enhanced mechanical properties. *Materials Science and Engineering: A* **654,** 124–130 (2016).

41. Wang, M. *et al.* Direct synthesis of high-quality graphene on Cu powders from adsorption of small aromatic hydrocarbons: a route to high strength and electrical conductivity for graphene/Cu composite. *Journal of Alloys and Compounds* **798,** 403–413 (2019).

42. Yang, Z. *et al.* Preparation mechanism of hierarchical layered structure of graphene/copper composite with ultrahigh tensile strength. *Carbon* **127,** 329–339 (2018).

43. Kawk, S.-R., Ring, T. A. & Choi, B.-S. A simple two-step fabrication route for Cu composite reinforced by three-dimensional graphene network. *Journal of Industrial and Engineering Chemistry* **70,** 484–488 (2019).

44. Taylor, C. D. & Tossey, B. M. High temperature oxidation of corrosion resistant alloys from machine learning. *npj Materials Degradation* **5,** 1–10 (2021).

45. Wei, Y. *et al.* Influencing factors and mechanism of high-temperature oxidation of high-entropy alloys: A review. *International Journal of Minerals, Metallurgy and Materials* **28,** 915–930 (2021).

46. Choi, Y.-J. *et al.* High temperature isothermal oxidation behavior of NbSi2 coating at 1000–1450 *Corrosion Science* **129,** 102–114 (2017).

47. LE GUYADER, H., GROLLEAU, A.-M., LEMIEUX, E., LUCAS, K. & WOLEJSZA, T. in *Corrosion behaviour and protection of copper and aluminium alloys in seawater* 95–115 (Elsevier, 2007).

48. Gautam, C. *et al.* Synthesis and 3D interconnected nanostructured h-BN-based biocomposites by low-temperature plasma sintering: bone regeneration applications. *ACS omega* **3,** 6013–6021 (2018).

49. Guiney, L. M. *et al.* Three-dimensional printing of cytocompatible, thermally conductive hexagonal boron nitride nanocomposites. *Nano letters* **18,** 3488–3493 (2018).

50. Yin, J., Li, X., Zhou, J. & Guo, W. Ultralight three-dimensional boron nitride foam with ultralow permittivity and superelasticity. *Nano letters* **13,** 3232–3236 (2013).

51. Jin, J. *et al.* Catalyst-free synthesis of crumpled boron and nitrogen co-doped graphite layers with tunable bond structure for oxygen reduction reaction. *ACS nano* **8,** 3313–3321 (2014).

52. Wu, P., Wang, H., Tang, Y., Zhou, Y. & Lu, T. Three-dimensional interconnected network of graphene-wrapped porous silicon spheres: in situ magnesiothermic-reduction synthesis and enhanced lithium-storage capabilities. *ACS applied materials & interfaces* **6,** 3546–3552 (2014).

53. Tiwari, J. N., Tiwari, R. N. & Kim, K. S. Zero-dimensional, one-dimensional, two-dimensional and three-dimensional nanostructured materials for advanced electrochemical energy devices. *Progress in Materials Science* **57,** 724–803 (2012).

54. Singh, R. & Singh, R. K. A Review on Nano Materials of Carbon. *J. Appl. Phys* **9,** 42–57 (2017).

55. Xu, M., Liang, T., Shi, M. & Chen, H. Graphene-like two-dimensional materials. *Chemical reviews* **113,** 3766–3798 (2013).

56. Zhang, K., Feng, Y., Wang, F., Yang, Z. & Wang, J. Two dimensional hexagonal boron nitride (2D-hBN): synthesis, properties and applications. *Journal of Materials Chemistry C* **5,** 11992–12022 (2017).

57. Jiang, H. & Lin, J. Hexagonal boron nitride for deep ultraviolet photonic devices. *Semiconductor Science and Technology* **29,** 084003 (2014).

58. Hui, F. *et al.* On the use of two dimensional hexagonal boron nitride as dielectric. *Microelectronic Engineering* **163,** 119–133 (2016).

59. Constantinescu, G. C. & Hine, N. D. Multipurpose black-phosphorus/hBN heterostructures. *Nano letters* **16,** 2586–2594 (2016).

60. Bao, J. *et al.* Two-dimensional hexagonal boron nitride as lateral heat spreader in electrically insulating packaging. *Journal of Physics D: Applied Physics* **49,** 265501 (2016).

61. Oh, K.-H. *et al.* Enhanced durability of polymer electrolyte membrane fuel cells by functionalized 2D boron nitride nanoflakes. *ACS applied materials & interfaces* **6,** 7751–7758 (2014).

62. Chimene, D., Alge, D. L. & Gaharwar, A. K. Two-dimensional nanomaterials for biomedical applications: emerging trends and future prospects. *Advanced Materials* **27,** 7261–7284 (2015).

63. Roy, S. *et al.* Structure, Properties and Applications of Two-Dimensional Hexagonal Boron Nitride. *Advanced Materials,* 2101589 (2021).

64. Chopra, N. G. *et al.* Boron nitride nanotubes. *Science* **269,** 966–967 (1995).

65. Li, L. H. & Chen, Y. Atomically thin boron nitride: unique properties and applications. *Advanced Functional Materials* **26,** 2594–2608 (2016).

66. Li, L. H., Cervenka, J., Watanabe, K., Taniguchi, T. & Chen, Y. Strong oxidation resistance of atomically thin boron nitride nanosheets. *ACS nano* **8,** 1457–1462 (2014).

67. Kumar, R., Rajasekaran, G & Parashar, A. Optimised cut-off function for Tersoff-like potentials for a BN nanosheet: a molecular dynamics study. *Nanotechnology* **27,** 085706 (2016).

68. Wang, Z. *et al.* Fabrication of boron nitride nanosheets by exfoliation. *The Chemical Record* **16,** 1204–1215 (2016).

69. Bao, J. *et al.* Synthesis and applications of two-dimensional hexagonal boron nitride in electronics manufacturing. *Electronic Materials Letters* **12,** 1–16 (2016).

70. Nam, T.-H., Lee, J.-H., Choi, S.-R., Yoo, J.-B. & Kim, J.-G. Graphene coating as a protective barrier against hydrogen embrittlement. *International journal of hydrogen energy* **39,** 11810–11817 (2014).

71. Lee, C., Wei, X., Kysar, J. W. & Hone, J. Measurement of the elastic properties and intrinsic strength of monolayer graphene. *science* **321,** 385–388 (2008).

72. Calizo, I. *et al.* Raman nanometrology of graphene: Temperature and substrate effects. *Solid State Communications* **149,** 1132–1135 (2009).

73. Ahn, J.-H. *et al.* Things you could do with graphene. *Nat Nanotechnol* **9,** 737–747 (2014).

74. Balandin, A. A. *et al.* Superior thermal conductivity of single-layer graphene. *Nano letters* **8,** 902–907 (2008).

75. Neto, A. C., Guinea, F. & Peres, N. M. Drawing conclusions from graphene. *Physics world* **19,** 33 (2006).

76. Littlejohn, S. D. *Electrical properties of graphite nanoparticles in silicone: Flexible oscillators and electromechanical sensing* (Springer Science & Business Media, 2013).

77. Tiwari, S. K. *et al.* Magical allotropes of carbon: prospects and applications. *Critical Reviews in Solid State and Materials Sciences* **41,** 257–317 (2016).

78. Huang, X. *et al.* Graphene-based materials: synthesis, characterization, properties, and applications. *small* **7,** 1876–1902 (2011).

79. Agarwal, A., Lahiri, D. & Bakshi, S. R. *Carbon nanotubes: reinforced metal matrix composites* (CRC press, 2018).

80. Abbott, I. E. Graphene: exploring carbon flatland. *Phys. Today* **60,** 35 (2007).

81. Bolotin, K. I. *et al.* Ultrahigh electron mobility in suspended graphene. *Solid state communications* **146,** 351–355 (2008).

82. Geim, A. Nature Mater. 6, 183 (2007); AH Castro Neto, F. Guinea, NMR Peres, KS Novoselov, and AK Geim. *Rev. Mod. Phys* **81,** 109 (2009).

83. Kauling, A. P. *et al.* The worldwide graphene flake production. *Advanced Materials* **30,** 1803784 (2018).

84. Ferrari, A. C. *et al.* Science and technology roadmap for graphene, related two-dimensional crystals, and hybrid systems. *Nanoscale* **7,** 4598–4810 (2015).

85. Mortensen, A & Llorca, J. Metal Matrix Composites Annual Review of Materials Research (2010).

86. Sidhu, S. S., Kumar, S. & Batish, A. Metal matrix composites for thermal management: a review. *Critical Reviews in Solid State and Materials Sciences* **41,** 132–157 (2016).

87. Miracle, D. Metal matrix composites–from science to technological significance. *Composites science and technology* **65,** 2526–2540 (2005).

88. Macke, A., Schultz, B. & Rohatgi, P. Metal matrix composites. *Adv. Mater. Processes* **170,** 19–23 (2012).

89. Zandiatashbar, A, Picu, R. & Koratkar, N. Mechanical behavior of epoxy-graphene platelets nanocomposites. *Journal of engineering materials and technology* **134** (2012).

90. Nieto, A., Bisht, A., Lahiri, D., Zhang, C. & Agarwal, A. Graphene reinforced metal and ceramic matrix composites: a review. *International Materials Reviews* **62,** 241–302 (2017).

91. Song, Y *et al.* Microscopic mechanical properties of titanium composites containing multi-layer graphene nanofillers. *Materials & Design* **109,** 256–263 (2016).

92. Li, M., Che, H., Liu, X., Liang, S. & Xie, H. Highly enhanced mechanical properties in Cu matrix composites reinforced with graphene decorated metallic nanoparticles. *Journal of materials science* **49,** 3725–3731 (2014).

93. Chu, K., Wang, F., Wang, X.-h. & Huang, D.-j. Anisotropic mechanical properties of graphene/copper composites with aligned graphene. *Materials Science and Engineering: A* **713,** 269–277 (2018).

94. Asgharzadeh, H. & Sedigh, M. Synthesis and mechanical properties of Al matrix composites reinforced with few-layer graphene and graphene oxide. *Journal of Alloys and Compounds* **728,** 47–62 (2017).

95. Nieto, A., Lahiri, D. & Agarwal, A. Synthesis and properties of bulk graphene nanoplatelets consolidated by spark plasma sintering. *Carbon* **50,** 4068–4077 (2012).

96. Pérez-Bustamante, R, Bolaños-Morales, D, Bonilla-Martínez, J, Estrada-Guel, I & Martínez-Sánchez, R. Microstructural and hardness behavior of graphene-nanoplatelets/aluminum composites synthesized by mechanical alloying. *Journal of alloys and compounds* **615,** S578–S582 (2014).

97. Kumar, H. P. & Xavior, M. A. Graphene reinforced metal matrix composite (GRMMC): a review. *Procedia Engineering* **97,** 1033–1040 (2014).

98. Kim, W., Lee, T. & Han, S. Multi-layer graphene/copper composites: Preparation using high-ratio differential speed rolling, microstructure and mechanical properties. *Carbon* **69,** 55–65 (2014).

99. Dutkiewicz, J. *et al.* Microstructure and properties of bulk copper matrix composites strengthened with various kinds of graphene nanoplatelets. *Materials Science and Engineering: A* **628,** 124–134 (2015).

100. Borkar, T. *et al.* Excellent strength–ductility combination in nickel-graphite nanoplatelet (GNP/Ni) nanocomposites. *Journal of Alloys and Compounds* **646,** 135–144 (2015).

101. Yalçın, E., Çanakçı, A, Erdemir, F., Çuvalcı, H & Karabacak, A. Enhancement of wear and corrosion resistance of ZA27/nanographene composites produced by powder metallurgy. *Arabian Journal for Science and Engineering* **44,** 1437–1445 (2019).

102. Salvo, C, Mangalaraja, R., Udayabashkar, R, Lopez, M & Aguilar, C. Enhanced mechanical and electrical properties of novel graphene reinforced copper matrix composites. *Journal of Alloys and Compounds* **777,** 309–316 (2019).

103. Yue, H. *et al.* Effect of ball-milling and graphene contents on the mechanical properties and fracture mechanisms of graphene nanosheets reinforced copper matrix composites. *Journal of Alloys and Compounds* **691,** 755–762 (2017).

104. Shin, S., Choi, H., Shin, J. & Bae, D. Strengthening behavior of few-layered graphene/aluminum composites. *Carbon* **82,** 143–151 (2015).

105. Bhadauria, A., Singh, L. K. & Laha, T. Combined strengthening effect of nanocrystalline matrix and graphene nanoplatelet reinforcement on the mechanical properties of spark plasma sintered aluminum based nanocomposites. *Materials Science and Engineering: A* **749,** 14–26 (2019).

106. Chen, Q., Zhang, L. & Chen, G. Facile preparation of graphene-copper nanoparticle composite by in situ chemical reduction for electrochemical sensing of carbohydrates. *Analytical chemistry* **84,** 171–178 (2012).

107. Wang, L. *et al.* Graphene-copper composite with micro-layered grains and ultrahigh strength. *Scientific Reports* **7,** 1–10 (2017).

108. Li, X. *et al.* Large-area synthesis of high-quality and uniform graphene films on copper foils. *science* **324,** 1312–1314 (2009).

109. Xiang, S. *et al.* Graphene nanoplatelets induced heterogeneous bimodal structural magnesium matrix composites with enhanced mechanical properties. *Scientific reports* **6,** 1–13 (2016).

110. Clyne, T. & Withers, P. *An introduction to metal matrix composites* (Cambridge university press, 1995).

111. Hidalgo-Manrique, P. *et al.* Microstructure and mechanical behaviour of aluminium matrix composites reinforced with graphene oxide and carbon nanotubes. *Journal of Materials Science* **52,** 13466–13477 (2017).

112. Young, R. J. *et al.* The mechanics of reinforcement of polymers by graphene nanoplatelets. *Composites Science and Technology* **154,** 110–116 (2018).

113. Suk, J. W., Piner, R. D., An, J. & Ruoff, R. S. Mechanical properties of monolayer graphene oxide. *ACS nano* **4,** 6557–6564 (2010).

114. Ruiz-Vargas, C. S. *et al.* Softened elastic response and unzipping in chemical vapor deposition graphene membranes. *Nano letters* **11,** 2259–2263 (2011).

115. Nicholl, R. J. *et al.* The effect of intrinsic crumpling on the mechanics of free-standing graphene. *Nature communications* **6,** 1–7 (2015).

116. Ahmad, S., Hashim, J & Ghazali, M. Effect of porosity on tensile properties of cast particle reinforced MMC. *Journal of composite materials* **41,** 575–589 (2007).

117. Oliver, W. C. & Pharr, G. M. An improved technique for determining hardness and elastic modulus using load and displacement sensing indentation experiments. *Journal of materials research* **7,** 1564–1583 (1992).

118. Hwang, J. *et al.* Enhanced mechanical properties of graphene/copper nanocomposites using a molecular-level mixing process. *Advanced materials* **25,** 6724–6729 (2013).

119. Xia, X., Su, Y., Zhong, Z. & Weng, G. J. A unified theory of plasticity, progressive damage and failure in graphene-metal nanocomposites. *International journal of plasticity* **99,** 58–80 (2017).

120. Mercier, D., Vanhumbeeck, J.-F., Caruso, M., Eynde, X. V. & Febvre, M. Microstructural and mechanical characterisation of electroplated nickel matrix composite coatings. *Surface Engineering* **35,** 177–188 (2019).

121. Liu, C., Su, F. & Liang, J. Producing cobalt–graphene composite coating by pulse electrodeposition with excellent wear and corrosion resistance. *Applied Surface Science* **351,** 889–896 (2015).

122. Pavithra, C. L., Sarada, B. V., Rajulapati, K. V., Rao, T. N. & Sundararajan, G. A new electrochemical approach for the synthesis of copper-graphene nanocomposite foils with high hardness. *Scientific reports* **4,** 1–7 (2014).

123. Ren, W. *et al.* A Facile and Cost-Effective Approach to Fabricate In-Situ Synthesized Graphene Nanosheet Reinforced 316L Stainless Steel. *JOM,* 1–8 (2020).

124. Cao, H. *et al.* Thermal properties of in situ grown graphene reinforced copper matrix laminated composites. *Journal of Alloys and Compounds* **771,** 228–237 (2019).

125. Fu, K. *et al.* An approach for fabricating Ni@ graphene reinforced nickel matrix composites with enhanced mechanical properties. *Materials Science and Engineering: A* **715,** 108–116 (2018).

126. Liu, G. *et al.* In-situ synthesis of graphene decorated with nickel nanoparticles for fabricating reinforced 6061Al matrix composites. *Materials Science and Engineering: A* **699,** 185–193 (2017).

127. Guo, S. *et al.* In situ synthesis of high content graphene nanoplatelets reinforced Cu matrix composites with enhanced thermal conductivity and tensile strength. *Powder Technology* **362,** 126–134 (2020).

128. Zhang, X. *et al.* A powder-metallurgy-based strategy toward three-dimensional graphene-like network for reinforcing copper matrix composites. *Nature communications* **11,** 1–13 (2020).

129. Gao, L., Guest, J. R. & Guisinger, N. P. Epitaxial graphene on Cu (111). *Nano letters* **10,** 3512–3516 (2010).

130. Li, X., Cai, W., Colombo, L. & Ruoff, R. S. Evolution of graphene growth on Ni and Cu by carbon isotope labeling. *Nano letters* **9,** 4268–4272 (2009).

131. Losurdo, M., Giangregorio, M. M., Capezzuto, P. & Bruno, G. Graphene CVD growth on copper and nickel: role of hydrogen in kinetics and structure. *Physical Chemistry Chemical Physics* **13,** 20836–20843 (2011).

132. Al-Hilfi, S. H., Kinloch, I. A. & Derby, B. Chemical Vapor Deposition of Graphene on Cu-Ni Alloys: The Impact of Carbon Solubility. *Coatings* **11,** 892 (2021).

133. Yang, C. *et al.* Copper-vapor-assisted rapid synthesis of large AB-stacked bilayer graphene domains on Cu-Ni alloy. *Small* **12,** 2009–2013 (2016).

134. Liu, X. *et al.* Segregation growth of graphene on Cu–Ni alloy for precise layer control. *The Journal of Physical Chemistry C* **115,** 11976–11982 (2011).

135. Chen, P.-Y. & Alu, A. Atomically thin surface cloak using graphene monolayers. *ACS nano* **5,** 5855–5863 (2011).

136. Wu, Y. *et al.* Growth mechanism and controlled synthesis of AB-stacked bilayer graphene on Cu–Ni alloy foils. *Acs Nano* **6,** 7731–7738 (2012).

137. Choi, H. *et al.* Precise control of chemical vapor deposition graphene layer thickness using Ni x Cu 1- x alloys. *Journal of Materials Chemistry C* **3,** 1463–1467 (2015).

138. Hu, X., Bjo?rkman, T., Lipsanen, H., Sun, L. & Krasheninnikov, A. V. Solubility of boron, carbon, and nitrogen in transition metals: getting insight into trends from first-principles calculations. *The Journal of Physical Chemistry Letters* **6,** 3263–3268 (2015).

139. Shu, R. *et al.* Synergetic effect of nano-carbon and HBN on microstructure and mechanical properties of Cu/Ti3SiC2/C nanocomposites. *Materials Science and Engineering: A* **755,** 128–137 (2019).

140. Li, M.-X., Xie, J., Li, Y.-D. & Xu, H.-H. Reduced graphene oxide dispersed in copper matrix composites: Facile preparation and enhanced mechanical properties. *physica status solidi (a)* **212,** 2154–2161 (2015).

141. Jo, Y., Lib, X., Choc, D. & Choib, B.-S. Tensile properties of three-dimensionally interconnected graphene-networked Cu composite and changes in its microstructure in relation to heat treatment temperature (2019).

142. Tang, Y., Yang, X., Wang, R. & Li, M. Enhancement of the mechanical properties of graphene–copper composites with graphene–nickel hybrids. *Materials Science and Engineering: A* **599,** 247–254 (2014).

143. Cui, Y., Wang, L., Li, B., Cao, G. & Fei, W. Effect of ball milling on the defeat of few-layer graphene and properties of copper matrix composites. *Acta Metallurgica Sinica (English Letters)* **27,** 937–943 (2014).

144. Chen, W. *et al.* Advances in graphene reinforced metal matrix nanocomposites: Mechanisms, processing, modelling, properties and applications. *Nanotechnology and Precision Engineering* **3,** 189–210 (2020).

145. Yan, S. *et al.* Investigating aluminum alloy reinforced by graphene nanoflakes. *Materials Science and Engineering: A* **612,** 440–444 (2014).

146. Wang, H., Zhang, K. & Zhang, M. Fabrication and properties of Ni-modified graphene nanosheets reinforced Sn-Ag-Cu composite solder. *Journal of Alloys and Compounds* **781,** 761–772 (2019).

147. Kim, Y. *et al.* Strengthening effect of single-atomic-layer graphene in metal–graphene nanolayered composites. *Nature communications* **4,** 1–7 (2013).

148. Chu, K. *et al.* Interface structure and strengthening behavior of graphene/CuCr composites. *Carbon* **133,** 127–139 (2018).

149. Kato, M. Hall–Petch relationship and dislocation model for deformation of ultrafine-grained and nanocrystalline metals. *Materials Transactions* **55,** 19–24 (2014).

150. Zhang, X. *et al.* Achieving high strength and high ductility in metal matrix composites reinforced with a discontinuous three-dimensional graphene-like network. *Nanoscale* **9,** 11929–11938 (2017).

151. Huang, G. *et al.* Preparation and characterization of the graphene-Cu composite film by electrodeposition process. *Microelectronic engineering* **157,** 7–12 (2016).

152. Chen, F. *et al.* Effects of graphene content on the microstructure and properties of copper matrix composites. *Carbon* **96,** 836–842 (2016).

153. Gao, X. *et al.* Mechanical properties and thermal conductivity of graphene reinforced copper matrix composites. *Powder Technology* **301,** 601–607 (2016).

154. Hsieh, C.-C. & Liu, W.-R. Synthesis and characterization of nitrogen-doped graphene nanosheets/copper composite film for thermal dissipation. *Carbon* **118,** 1–7 (2017).

155. Wejrzanowski, T. *et al.* Thermal conductivity of metal-graphene composites. *Materials & design* **99,** 163–173 (2016).

156. Luo, H. *et al.* Copper matrix composites enhanced by silver/reduced graphene oxide hybrids. *Materials Letters* **196,** 354–357 (2017).

157. Si, X. *et al.* Effect of carbide interlayers on the microstructure and properties of graphene-nanoplatelet-reinforced copper matrix composites. *Materials Science and Engineering: A* **708,** 311–318 (2017).

158. Ponraj, N. V. *et al.* Effect of milling on dispersion of graphene nanosheet reinforcement in different morphology copper powder matrix. *Surfaces and Interfaces* **9,** 260–265 (2017).

159. Chu, K. *et al.* Thermal properties of graphene/metal composites with aligned graphene. *Materials & Design* **140,** 85–94 (2018).

160. Mahvash, F *et al.* Corrosion resistance of monolayer hexagonal boron nitride on copper. *Scientific reports* **7,** 1–5 (2017).

161. Li Xue Ahmed Ateeq, C. B.-S. Electrochemical Corrosion Resistance and Electrical Conductivity of Three-Dimensionally Interconnected Graphene-Reinforced Cu Composites. *Korean J. Met. Mater.* **59,** 821–828 (2021).

162. Hussain, Z., Yang, H. & Choi, B.-S. Synthesis of Three-Dimensionally Interconnected Hexagonal Boron Nitride Networked Cu-Ni Composite. *Korean Journal of Metals and Materials* **59,** 505–513 (2021).

163. Chatterjee, S. *et al.* Syntheses of boron nitride nanotubes from borazine and decaborane molecular precursors by catalytic chemical vapor deposition with a floating nickel catalyst. *Chemistry of Materials* **24,** 2872–2879 (2012).

164. Hussain, Z., Jang, H., Choi, H. & Choi, B.-S. Microstructure, Mechanical Behavior, and Thermal Conductivity of Three-Dimensionally Interconnected Hexagonal Boron Nitride-Reinforced Cu-Ni Composite. *Journal of Materials Engineering and Performance,* 1–9 (2021).

165. Ding, Y. *et al.* in *Novel Nanomaterials-Synthesis and Applications* (IntechOpen, 2017).

166. Fish, P. Electron diffraction and the Bragg equation. *Physics Education* **6,** 7 (1971).

167. Alhumade, H., Abdala, A., Yu, A., Elkamel, A. & Simon, L. Corrosion inhibition of copper in sodium chloride solution using polyetherimide/graphene composites. *The Canadian Journal of Chemical Engineering* **94,** 896–904 (2016).

168. Roylance, D. Stress-strain curves. *Massachusetts Institute of Technology study, Cambridge* (2001).

169. Khalaj, M. *et al.* Recent Progress in the Study of Thermal Properties and Tribological Behaviors of Hexagonal Boron Nitride-Reinforced Composites. *Journal of composites science* **4,** 116 (2020).

170. Parker, W., Jenkins, R., Butler, C. & Abbott, G. Flash method of determining thermal diffusivity, heat capacity, and thermal conductivity. *Journal of applied physics* **32,** 1679–1684 (1961).

171. German, R. M. Coarsening in sintering: grain shape distribution, grain size distribution, and grain growth kinetics in solid-pore systems. *Critical reviews in solid state and materials sciences* **35,** 263–305 (2010).

172. McDonald, S. *et al.* Microstructural evolution during sintering of copper particles studied by laboratory diffraction contrast tomography (LabDCT). *Scientific Reports* **7,** 1–11 (2017).

173. Joshi, S. *et al.* Boron nitride on Cu (111): an electronically corrugated monolayer. *Nano letters* **12,** 5821–5828 (2012).

174. Lin, Y., Williams, T. V. & Connell, J. W. Soluble, exfoliated hexagonal boron nitride nanosheets. *The Journal of Physical Chemistry Letters* **1,** 277–283 (2010).

175. Shi, Y. *et al.* Synthesis of few-layer hexagonal boron nitride thin film by chemical vapor deposition. *Nano letters* **10,** 4134–4139 (2010).

176. Paszkowicz, W, Pelka, J., Knapp, M, Szyszko, T & Podsiadlo, S. Lattice parameters and anisotropic thermal expansion of hexagonal boron nitride in the 10–297.5 K temperature range. *Applied Physics A* **75,** 431–435 (2002).

177. Hedayatian, M., Vahedi, K., Nezamabadi, A. & Momeni, A. Microstructural and mechanical behavior of Al6061-graphene oxide nanocomposites. *Metals and Materials International* **26,** 760–772 (2020).

178. Yoo, S. C. *et al.* Enhanced mechanical properties of boron nitride nanosheet/copper nanocomposites via a molecular-level mixing process. *Composites Part B: Engineering* **195,** 108088 (2020).

179. Madhukar, P. *et al.* Microstructure studies of AA7150-hBN nanocomposites fabricated by ultrasonic assisted stir casting. *Materials Research Express* **6,** 116545 (2019).

180. Yao, W. & Fan, L. Effect of defects on mechanical properties of novel hybrid graphene-h-BN/copper layered nanostructures. *Applied Physics A* **125,** 1–13 (2019).

181. Xiong, D.-B. *et al.* Graphene-and-copper artificial nacre fabricated by a preform impregnation process: bioinspired strategy for strengthening-toughening of metal matrix composite. *Acs Nano* **9,** 6934–6943 (2015).

182. Chen, T.-A. *et al.* Wafer-scale single-crystal hexagonal boron nitride monolayers on Cu (111). *Nature* **579,** 219–223 (2020).

183. Smallman, R. & Westmacott, K. Stacking faults in face-centred cubic metals and alloys. *Philosophical magazine* **2,** 669–683 (1957).

184. Mustapha, S *et al.* Comparative study of crystallite size using Williamson-Hall and Debye-Scherrer plots for ZnO nanoparticles. *Advances in Natural Sciences: Nanoscience and Nanotechnology* **10,** 045013 (2019).

185. Kostecki, M., Cygan, T., Petrus, M. & Jaroszewicz, J. Thermal properties of multilayer graphene and hBN reinforced copper matrix composites. *Journal of Thermal Analysis and Calorimetry* **138,** 3873–3883 (2019).

186. Mortazavi, B. *et al.* Machine-learning interatomic potentials enable first-principles multiscale modeling of lattice thermal conductivity in graphene/borophene heterostructures. *Materials Horizons* **7,** 2359–2367 (2020).

187. Zheng, J.-C. *et al.* High thermal conductivity of hexagonal boron nitride laminates. *2D Materials* **3,** 011004 (2016).

188. Shen, H. *et al.* Fabrication of oriented hBN scaffolds for thermal interface materials. *RSC advances* **6,** 16489–16494 (2016).

189. Chilkoor, G. *et al.* Hexagonal boron nitride: the thinnest insulating barrier to microbial corrosion. *ACS nano* **12,** 2242–2252 (2018).

190. Husain, E. *et al.* Marine corrosion protective coatings of hexagonal boron nitride thin films on stainless steel. *ACS applied materials & interfaces* **5,** 4129–4135 (2013).

191. Al-Saadi, S., Banerjee, P. C., Anisur, M. & Raman, R. Hexagonal boron nitride impregnated silane composite coating for corrosion resistance of magnesium alloys for temporary bioimplant applications. *Metals* **7,** 518 (2017).

192. Raman, R. S. *et al.* Protecting copper from electrochemical degradation by graphene coating. *Carbon* **50,** 4040–4045 (2012).

193. Lee, H.-S., Singh, J. K., Ismail, M. A. & Bhattacharya, C. Corrosion resistance properties of aluminum coating applied by arc thermal metal spray in SAE J2334 solution with exposure periods. *Metals* **6,** 55 (2016).

194. Feliu, S. Electrochemical impedance spectroscopy for the measurement of the corrosion rate of magnesium alloys: brief review and challenges. *Metals* **10,** 775 (2020).

195. Wang, S., Liu, X., Yin, X., Zhang, B. & Du, N. High-temperature oxidation behavior of Ti2AlNb alloy with PEO/hBN composite coating at 1000 *Surface and Coatings Technology* **404,** 126473 (2020).

196. Chen, Y., Zou, J., Campbell, S. J. & Le Caer, G. Boron nitride nanotubes: Pronounced resistance to oxidation. *Applied physics letters* **84,** 2430–2432 (2004).

197. Chakrabarty, K., Arnold, I. & Catledge, S. A. Hexagonal boron nitride grown using high atomic boron emission during microwave plasma chemical vapor deposition. *Journal of Vacuum Science & Technology A: Vacuum, Surfaces, and Films* **37,** 061507 (2019).

198. Raj, R. R. & Kanagasabapathy, H. Influence of abrasive water jet machining parameter on performance characteristics of AA7075-ZrSiO4-hBN hybrid metal matrix composites. *Materials Research Express* **5,** 106509 (2018).

199. Nan, H. Y. *et al.* The thermal stability of graphene in air investigated by Raman spectroscopy. *Journal of Raman Spectroscopy* **44,** 1018–1021 (2013).

200. Xu, Y., Ma, T., Wang, X., Jiang, Y. & Yan, M. High temperature oxidation resistance of hot-pressed h-BN/ZrO2 composites. *Ceramics International* **40,** 11171–11176 (2014).

201. Mustakeem, M. Electrode materials for microbial fuel cells: nanomaterial approach (2015).

202. Su, D. S. *et al.* Metal-free heterogeneous catalysis for sustainable chemistry. *ChemSusChem: Chemistry & Sustainability Energy & Materials* **3,** 169–180 (2010).

203. Ping, Y., Gong, Y., Fu, Q. & Pan, C. Preparation of three-dimensional graphene foam for high performance supercapacitors. *Progress in Natural Science: Materials International* **27,** 177–181 (2017).

204. Nacken, T. J., Damm, C., Xing, H., Rüger, A. & Peukert, W. Determination of quantitative structure-property and structure-process relationships for graphene production in water. *Nano Research* **8,** 1865–1881 (2015).

205. Wu, M. *et al.* Graphene platelet reinforced copper composites for improved tribological and thermal properties. *RSC Advances* **9,** 39883–39892 (2019).

206. Kamboj, A., Raghupathy, Y, Rekha, M. & Srivastava, C. Morphology, texture and corrosion behavior of nanocrystalline copper–graphene composite coatings. *JOM* **69,** 1149–1154 (2017).

207. Heiba, A. R., Taher, F. A., Abou Shahba, R. M. & Ghany, N. A. A. Corrosion mitigation of carbon steel in acidic and salty solutions using electrophoretically deposited graphene coatings. *Journal of Coatings Technology and Research* **18,** 501–510 (2021).

208. Yamabe, J., Awane, T. & Murakami, Y. Hydrogen trapped at intermetallic particles in aluminum alloy 6061-T6 exposed to high-pressure hydrogen gas and the reason for high resistance against hydrogen embrittlement. *international journal of hydrogen energy* **42,** 24560–24568 (2017).

209. Li, M & Zinkle, S. 4.20-physical and mechanical properties of copper and copper alloys. *Comprehensive nuclear materials,* 667–690 (2012).

APPENDIX A: Main Reagents and Materials

The reagents and materials used in this work are listed in Table A.1

Table A.1: Main Reagents and Materials.

Reagents and materials	Quality
Copper powder	99% purity, 14-25 μm (spherical)
Nickel powder	99.5% purity, 1∼5 μm (spherical)
Hydrochloric acid	Assay above 35% , extra pure
$FeCl_3 \cdot 6H_2O$	97.0-102.0%
Ethanol	99.5% purity
Acetone	99.5% purity

APPENDIX B: Synthesis and Characterization Tools

B.1 CVD System

Two separate systems, CVD and MOCVD, were used to fabricate 3DiGr CuNi and 3Di-hBN CuNi composites.

1. The CVD apparatus used to fabricate 3DiGr CuNi composites had a gas distribution system consisting of H_2 (99.999%) and CH_4 (99.995%) flowing through each mass flow controller into a quartz tube furnace 1.5 m long and 80 mm in diameter, capable of reaching 1100°C. The gas pressure inside the chamber was controlled by a throttle valve in conjunction with a pressure controller. The system controlled the furnace temperature to ± 0.5°C at 1000°C, gas flow rate to ± 0.05 sccm at 10 sccm, and system pressure to ± 0.01 Torr at 330 and 450 Torr. The temperature profile within the chamber when the furnace was set at 1000°C was accurately determined by a single thermocouple moved down the length of the furnace, with measurements made at 2 cm intervals. A parabolic fit to the furnace temperature data gave an R^2 value of 0.99.

2. The MOCVD apparatus used to produce 3Di-hBN CuNi composites had a gas distribution system consisting of H_2 (99.999%), Ar(99.999%), NH_3 and decaborane evaporating system (shown in Figure 3.5 (a)).

B.2 Other Experimental Instruments

Table B.1 shows the other experimental instruments and their usage

B.3 Characterization Methods

Different instruments were employed in this study to characterize the materials fabricated and trace the reactions during the synthesis processes and are given in

Table B.1: Instruments and their usage.

Instrument	Model	Usage
Ultrasonic cleaner	BRANSON 2210R-DTH	Washing and cleaning
Drying oven	HANBAEK SCIENTIFIC CO.,LTD (HB-501M)	Drying
Vacuum glove box	JISICO J-924 AHO	Protection against moisture and oxidation
Polishing machine	ALLIED TWINPREP 3 7M	Surface polishing to reveal microsrture
Analytical Balances	SHINKO DENSHICO.,LTD (AF-R220E-D)	Weighing the samples

Table B.2. This section mainly introduces the graphene/hBN structure characterization technology used in this work, and characterization of other chemical and physical properties have been described in detail in section 3.4. These tools helped to optimize the synthesis conditions of the composites.

Table B.2: Structural characterization tools.

Instrument	Model
OM	NIKON
XRD	PANalytical CubiX3
SEM	HITACHI S-4800
TEM	TECNAI G20FEI

APPENDIX C: Sample Preparation for Microstructural Investigation

C.1 Sample Preparation for OM

1. Diamond cutting machine was used to cut the disc in two halves.
2. Then ultrasonic cleaner was used to clean the cut sample with alcohol to remove cutting oil and debris.
3. These samples were mounted in hot press mounting machine such that cross section could be easily polished.
4. Sandpapers of 1000-4000 grits were gradually used to polish the sample to get a smooth and scratch-free surface for subsequent examination.
5. Ultrasonic cleaner was used again to clean the polished samples with alcohol to remove the silicon and carbon particles (if any).
6. Then the samples were etched for 2-3 min in a mixed solution of $FeCl_3$ and HCl to reveal the microstructure. The method of making etchant is given below.

C.2 Etchant Preparation

1. Take 120 ml of DI water using volumetric flask and pour it in a clean beaker.
2. Weigh 10 g of $FeCl_3$ solution and put in the beaker containing 120 ml of DI water.
3. Take 30 ml of HCl (11.67 M) and put it in mixture containing the $FeCl_3$ and DI water.
4. Continuously stir the mixture using magnetic stirrer until solution becomes homogeneous.
5. The etchant is the mixed solution of 0.5 M $FeCl_3$ and 2 M HCl solutions.

C.3 Sample Preparation for SEM

1. Cut the small portion (one-fourth) of the composite disk and ultrasonicate it using ethanol to remove the oil.
2. Place it in the etchant for a sufficiently long time leaving 3Di-hBN as a result of complete etching of the metal matrix. The metallic particles in 3Di-hBN CuNi composite are mostly in direct contact with each other. When the composite is placed in etchant, these metallic particles etch out forming channels thereby completely removing the CuNi matrix leaving behind 3Di-hBN or 3DiGr.
3. Wash 3Di-hBN and 3DiGr several times with DI water to remove the remains of etchant.
4. Dry the samples using freez-drying method as explained in the section C.4.
5. Dried samples can be readily examined using SEM to investigate the microstructure.

C.4 Freeze-Drying Method

This method was used so that 3Di-hBN or 3DiGr does not collapse during drying under the effect of capillary force. Afetr wasing with Di water, 3Di-hBN and 3DiGr foam were carefully placed in a container (like a small tube) alongwith DI water and were frozen down to $-60°C$. In the last step, water content is removed under vacuum while it is frozen. 3Di-hBN and 3DiGr foam have stable network of hBN or graphene layers which can be further used for SEM or TEM examination.

C.5 Sample Preparation for TEM

1. Carefully polish the composite disk down to thickness of less than 100 μm.
2. Make small pieces of diameter of 3 mm with the punching gun.

3. Put these pieces in the etchant ($FeCl_3$ and HCl solution)

4. When CuNi matrix is etched out completely, wash 3Di-hBN foam with DI water several times to remove the contents of etchant.

5. Transfer the washed 3Di-hBN foam on TEM grid for TEM examination.

APPENDIX D: Properties Measurement

D.1 Mechanical Properties

1. Young's modulus can simply be calculated by finding the slope of stress strain curve in the elastic (linear) region. The value can be found as per following equation D.1:

$$E = \frac{\sigma}{\varepsilon} \tag{D.1}$$

where σ and ε are stress and strain at any point in elastic region.

2. Yield strength can be calculated by 0.2% offset method as follows:

   - Take the linear section of the stress strain curve.
   - Draw a line parallel to it that passes through the strain axis at 0.2% strain.
   - At the intersection point of offset line and stress strain curve, note the value of stress (y-axis). This value is yield stress.

3. Ultimate tensile strength can be calculate by simply noting the stress value in stress strain curve at the point where fracture starts.

4. Toughness is the total energy absorbed by a specimen before final fracture and can be calculated by approximating the area under the stress strain curve.

D.2 Heat Capacity Measurement with DSC Q2000

1. First, perform basic calibration of DSC (baseline, cell constant, temperature) to obtain specific heat conditions (heating speed 10°C min^{-1}, type of purge gas N_2, sample pan etc.).

2. Stabilize the cooling device (Refrigerated Cooling Systems (RCS) are used to perform DSC cooling experiments) in the equipment. Perform the following steps to stabilize RCS.

    - Check the cell status; c_p must have a good baseline status to obtain reliable data. Visually observe to remove contaminants or dust, and after running the baseline in the measurement range, open the baseline file in the UA program and adjust the Y-axis range to 1 mW. It is hoped that the baseline looks flat near the heat flow value of 0.
    - Turn on RCS at a speed of 20°C min^{-1} while letting air pass through the battery instead of N_2 upto 500°C . After gently wiping the battery with the supplied glass fiber brush, follow the wind to remove fiber fragments and other burning foreign objects, and then check the battery status again.

3. Use calibration mode to stabilize RCS, if the difference between the baselines in each cycle is small, RCS running style can be considered stable.

4. Use three-run method to measure sample c_p: this is a measurement method using sapphire registered in the ASTM method. A total of 3 experiments are required to measure the c_p of a sample.

5. Prepare sapphire for reference measurement.

6. Prepare several sets of lids and pans of almost the same weight. (The difference of each pair must not exceed 50 μg).

7. Put one pan + lid on the reference sensor, and put another pan + lid on the sample sensor, and then measure the ”blank” to obtain the heat flow value of the sample pan.

8. Then, put the sapphire in the pot of the sample sensor and measure the ”reference” to obtain the heat flow value of the standard sample.

9. Once done with sapphire, remove it from the pot of the sample sensor and insert the sample to obtain the heat flow value of the sample.

10. After completing three experiments, follow the below method to calculate the specific heat of the sample.

    The specific heat of sapphire ($c_{p,measured}$) is calculated by using following equation D.2

$$c_{p,sapphire;measured}(T) = \frac{W_{sapphire}(T) - W_{baseline}(T)}{m_{sapphire}(T)\Delta T} \tag{D.2}$$

    where $W_{sapphire,measured}$ and $W_{baseline}$ are the heat flow values of sapphire and blank at a given temperature T, respectively. $m_{sapphire}$ is the mass of sapphire. The following factor $E(T)$ is calculated by dividing the c_p value of sapphire taken from NIST database ($c_{p,exact}$) and $c_{p,\ measured}$ as follows:

$$E(T) = \frac{c_{p,sapphire;exact}(T)}{c_{p,sapphire;measured}(T)} \tag{D.3}$$

    The specific heat of the sample (measured value) is given by below equation D.4

$$c_{p,sample;measured(T)} = \frac{W_{sample}(T) - W_{baseline}(T)}{m_{sample}(T)\Delta T} \tag{D.4}$$

    where $W_{sample,measured}$ is the heat flow value and m_{sample} is the mass of the sample. The exact c_p value of sample is calculated by multiplying its measured value with the factor just calculated (equation D.3) according to the following equation D.5

$$c_{p,sample;exact}(T) = E(T) \times c_{p,sample;measured}(T) \tag{D.5}$$

APPENDIX E: Links to Permissions of Use

All data taken from outside sources have been properly cited in this dissertation with permission from the source where needed. Some of the data have been reproduced from sources registered under a Creative Common Attribution (CC BY) license. This license allows copying and reproducing the data for non-commercial purposes. For more details, the following url can be acccessed (https://creativecommons.org/about/cclicenses/).

As an evidence of permission to reproduce, we intend to provide details of the data reproduced here, and the relevant URL is easily accessible.

Figure 2.1:

https://www.iosrjournals.org/copyright-policy.html

Figure 2.2:

https://www.dropbox.com/s/2ru2q6fgdjr72t9/RightsLink%20Printable%20License%20%28Figure%202.2%29.pdf?dl=0

Figure 2.3:

https://pubs.rsc.org/en/content/articlelanding/2015/nr/c4nr01600a

Figure 2.4:

https://s100.copyright.com/AppDispatchServlet?title=Graphene%20nanoplatelets%20induced%20heterogeneous%20bimodal%20structural%20magnesium%20matrix%20composites%20with%20enhanced%20mechanical%20properties&author=Shulin%20Xiang%20et%20al&contentID=10.1038%2Fsrep38824&copyright=The%20Author%28s%29&publication=2045-2322&publicationDate=2016-12-12&publisherName=SpringerNature&orderBeanReset=true&oa=CC%20BY

Figure 2.5:

https://www.dropbox.com/s/91ivyihtsglpy0r/RightsLink%20Printable%2

0License%20%28Figure%202.5%29.pdf?dl=0

Figure 2.6:

https://s100.copyright.com/AppDispatchServlet?title=A%20New%20Electrochemical%20Approach%20for%20the%20Synthesis%20of%20Copper-Graphene%20Nanocomposite%20Foils%20with%20High%20Hardness&author=Chokkakula%20L.%20P.%20Pavithra%20et%20al&contentID=10.1038%2Fsrep04049&copyright=The%20Author%28s%29&publication=2045-2322&publicationDate=2014-02-11&publisherName=SpringerNature&orderBeanReset=true&oa=CC%20BY-NC-ND

Figure 2.7:

https://www.dropbox.com/s/f4yyafzv8iqq01u/RightsLink%20Printable%20License%20%28Figure%202.7%29.pdf?dl=0

Figure 2.9:

https://www.mdpi.com/openaccess

Figure 2.8

https://www.dropbox.com/s/tnf4d6z9qxcb2f3/Figure%202.8.pdf?dl=0

Figure 2.10:

https://www.dropbox.com/s/tnf4d6z9qxcb2f3/Figure%202.8.pdf?dl=0

Figure 3.7

http://kjmm.org/journal/view.php?number=552

Figures 3.8 and 3.9:

http://kjmm.org/journal/view.php?doi=10.3365/KJMM.2021.59.11.821

Figures 3.4, 3.5, 4., 4.2, 4.3, 4.4, 4.6, 4.7, and 4.8:

http://kjmm.org/journal/view.php?number=769

Figures 3.6, 3.10 (a), 4.9, 4.10, 4.11, 4.12, and 4.13:

https://www.dropbox.com/s/7bsgglwdiverup3/Mechanical%20Properties%

20%28Rights%20and%20Permissions%29.pdf?dl=0

Figure 4.25:

https://www.dropbox.com/s/02oh5vodwiqitqa/RightsLink%20Printable%2
0License%20%28Fig%204.25%29.pdf?dl=0